Document Version
Final published version

Citation (APA)
Liu, Z. (2026). *Boron-Doped Diamond for Electrochemical Sensing: Scrutinizing the Material and Advancing Applications*. [Dissertation (TU Delft), Delft University of Technology]. https://doi.org/10.4233/uuid:92204d41-37fd-47c6-b642-0f874029c5c5

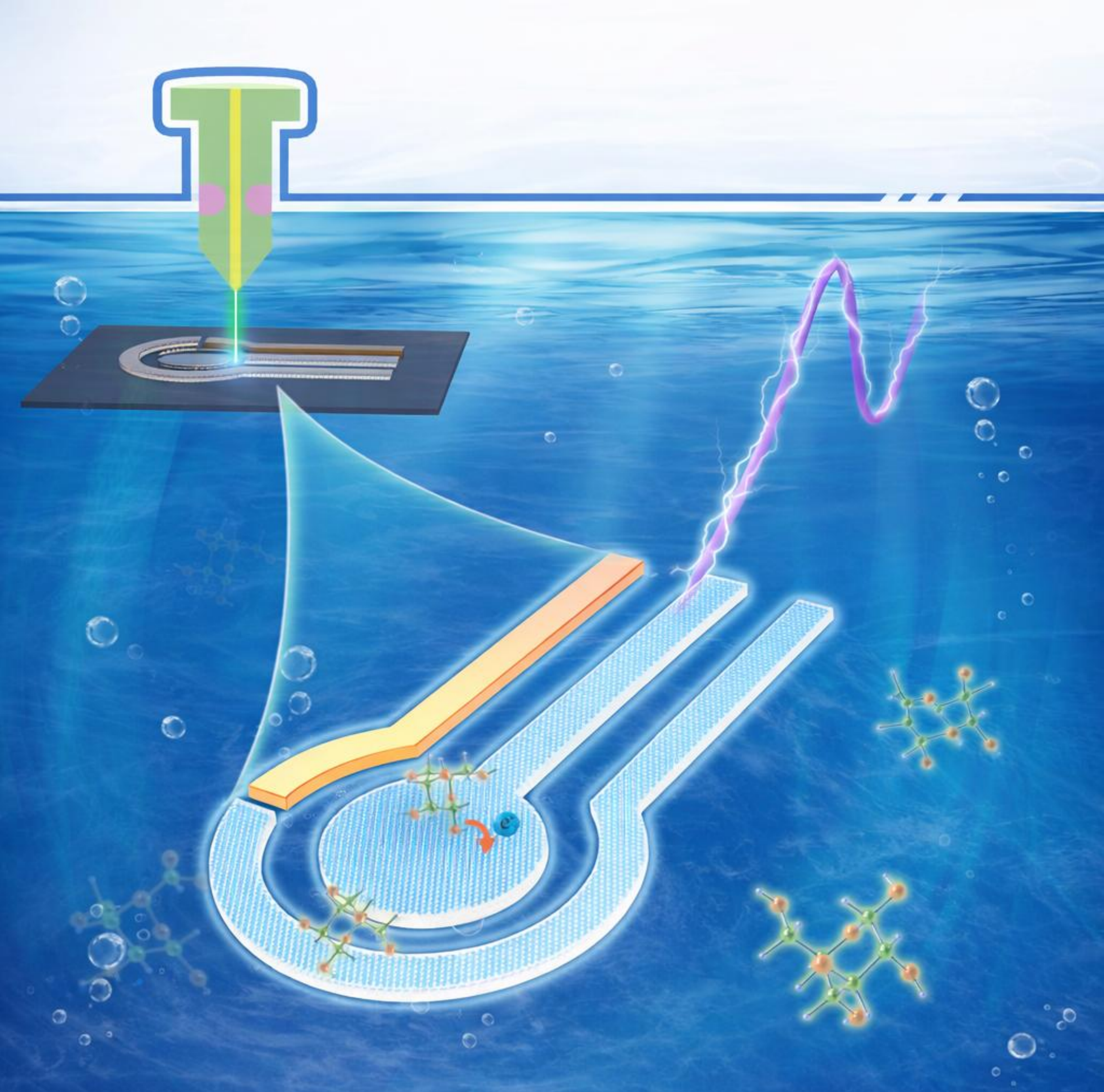

BORON-DOPED DIAMOND FOR ELECTROCHEMICAL SENSING:

SCRUTINIZING THE MATERIAL AND ADVANCING APPLICATIONS

Zhichao Liu

BORON-DOPED DIAMOND FOR ELECTROCHEMICAL SENSING: SCRUTINIZING THE MATERIAL AND ADVANCING APPLICATIONS

BORON-DOPED DIAMOND FOR ELECTROCHEMICAL SENSING: SCRUTINIZING THE MATERIAL AND ADVANCING APPLICATIONS

Dissertation

for the purpose of obtaining the degree of doctor
at Delft University of Technology
by the authority of the Rector Magnificus,
Prof. dr. ir. H. Bijl,
chair of the Board for Doctorates
to be defended publicly on
Wednesday, March 11, 2026 at 15:00

by

Zhichao LIU

This dissertation has been approved by the promotors

Composition of the doctoral committee:

Rector Magnificus,	Chairperson
Prof. dr. U. Staufer,	Delft University of Technology, Promotor
Dr. J. G. Buijnsters,	Delft University of Technology, Copromotor

Independent members:

Prof. dr. ir. J. M. C. Mol,	Delft University of Technology
Prof. dr. M. T. M. Koper,	Leiden University, the Netherlands
Prof. dr. J. Macpherson,	University of Warwick, UK
Prof. dr. K. Haenen,	Hasselt University, Belgium
Prof. dr. J. G. E. Gardeniers,	University of Twente, the Netherlands
Prof. dr. A. J. Houtepen,	Delft University of Technology, reserve member

Keywords: Boron-doped diamond, electrochemical sensing, sp^2 carbon, crystallinity, inkjet printing, voltammetry

Printed by: Proefschriftmaken

Cover art: Glucose detection on inkjet-printed BDD sensor. Generated by Z. Liu.

ISBN 978-94-6384-913-5

The journey ahead is vast and endless; I will seek unceasingly, high and low.

Qu Yuan, 340 BCE – 278 BCE, China

Contents

SUMMARY

This thesis investigates the properties of boron-doped diamond (BDD) electrodes, advances their applications, and develops innovative fabrication strategies, aiming to address key challenges in enhancing their performance and scalability. BDD has emerged as a versatile material for sensor applications due to its wide electrochemical potential window, exceptional chemical stability, and biocompatibility. The research presented in this dissertation is structured to investigate the relationships between material properties and electrochemical behavior, to assess critical factors influencing electrode performance, and to develop innovative fabrication techniques for practical applications.

Chapter 1 provides a comprehensive introduction to electrochemical sensors and the unique advantages of BDD electrodes, outlining their synthesis, material characteristics, and the factors affecting their electrochemical responses. This chapter also highlights the gaps in current research and establishes the objectives for the study, focusing on understanding microstructural variations, evaluating the role of sp^2 carbon and boron doping, and innovating manufacturing techniques.

Chapters 2 and 3 delve into the material properties of BDD and their impact on electrochemical activity. Chapter 2 investigates the heterogeneity in polycrystalline BDD electrodes by mapping of the boron distribution, crystal orientation, and localized electroactivity, utilizing advanced characterization techniques such as Raman spectroscopy and scanning electrochemical microscopy. Chapter 3 examines the role of sp^2 carbon content in non-enzymatic electrochemical sensing applications, focusing on the detection of the biologically relevant molecule glucose. These studies underscore the influence of boron doping levels and grain structure on electrode performance, providing insights for optimizing material properties.

Chapter 4 shifts attention to the fabrication of single-crystal BDD electrodes through heteroepitaxial growth. This chapter emphasizes the advantages of single-crystal structures in achieving uniform doping and superior electrochemical characteristics, addressing the limitations of polycrystalline BDD. The potential for these electrodes to improve sensor performance in detecting complex organic molecules is also explored.

In Chapter 5, the focus transitions to innovation in BDD electrode fabrication. A novel approach using inkjet printing is presented, enabling scalable and precise manufacturing of BDD sensor chips. This method optimizes ink composition, substrate preparation, and printing resolution, resulting in miniaturized sensor platforms with comparable performance to commercially available ones. The chapter highlights the potential of this technique to advance the practical deployment of BDD-based sensors in field applications.

Finally, Chapter 6 concludes the dissertation by summarizing the key findings and discussing the broader implications of the research. An outlook on future directions is provided, including recommendations for refining single-crystal BDD growth techniques and exploring new applications in biosensing and environmental monitoring. This thesis contributes significantly to the understanding and development of BDD electrodes, paving the way for their enhanced adoption in advanced electrochemical sensing technologies.

SAMENVATTING

Deze dissertatie onderzoekt de materiaaleigenschappen van boor-gedoteerde diamant (BDD)-elektroden, draagt bij aan de ontwikkeling van hun toepassingen en introduceert innovatieve fabricagestrategieën, met als doel belangrijke uitdagingen in prestaties en opschaalbaarheid aan te pakken. BDD is wordt gezien als een veelzijdig materiaal voor sensorapplicaties dankzij zijn brede elektrochemische venster, uitzonderlijke chemische stabiliteit en biocompatibiliteit. Het onderzoek in deze dissertatie is gestructureerd om de relaties tussen materiaaleigenschappen en elektrochemisch gedrag te onderzoeken, kritische factoren te evalueren die de prestaties van de elektroden beïnvloeden, en innovatieve fabricagetechnieken te ontwikkelen voor praktische toepassingen.

Hoofdstuk 1 biedt een uitgebreide introductie tot elektrochemische sensoren en de unieke voordelen van het gebruik van BDD-elektroden. Het bespreekt de synthese, materiaaleigenschappen en factoren die hun elektrochemische respons beïnvloeden. Dit hoofdstuk benadrukt ook de hiaten in huidig onderzoek en formuleert de doelstellingen van de thesis, met een focus op het begrijpen van microstructurele variaties, de rol van sp^2-koolstof en boordotering, en het innoveren van fabricagetechnieken.

Hoofdstukken 2 en 3 verdiepen zich in de materiaaleigenschappen van BDD en hun impact op de elektrochemische activiteit. Hoofdstuk 2 onderzoekt de heterogeniteit in polykristallijne BDD-elektroden door de verdeling van boor, kristaloriëntatie en lokale elektroactiviteit in kaart te brengen met geavanceerde karakterisatietechnieken zoals Ramanspectroscopie en scanning elektrochemische microscopie. Hoofdstuk 3 onderzoekt de rol van het sp^2-koolstofgehalte in niet-enzymatische elektrochemische sensorapplicaties, met een focus op de detectie van het biologisch relevante molecuul glucose. Deze studies benadrukken de invloed van boordoteringsniveaus en korrelstructuur op de prestaties van de BDD-elektroden, wat waardevolle inzichten biedt voor het optimaliseren van de materiaaleigenschappen.

Hoofdstuk 4 richt zich op de fabricage van enkelkristallijne BDD-elektroden via hetero-epitaxiale groei. Dit hoofdstuk benadrukt de voordelen van enkelkristalstructuren bij het bereiken van uniforme doping en superieure elektrochemische eigenschappen, waarmee de beperkingen van polykristallijne BDD-elektroden worden aangepakt. De potentiële verbeteringen van deze elektroden bij de detectie van complexe organische moleculen worden ook onderzocht.

In Hoofdstuk 5 wordt een innovatie in de fabricage van BDD-elektroden behandeld. Een nieuwe benadering met behulp van inkjetprinting wordt gepresenteerd, waarmee een schaalbare en precieze productie van BDD-sensorchips mogelijk wordt gemaakt. Deze methode optimaliseert de inkt samenstelling, substraat voorbehandeling en printresolutie, wat resulteert in miniatuur sensoren met prestaties die vergelijkbaar zijn met commercieel verkrijgbare sensoren. Dit hoofdstuk belicht het potentieel van deze techniek om de praktische toepassing van BDD-gebaseerde sensoren in veldtoepassingen te

bevorderen.

Tot slot vat Hoofdstuk 6 de belangrijkste bevindingen samen en bespreekt het de bredere implicaties van het onderzoek. Er wordt een toekomstperspectief geschetst, inclusief aanbevelingen voor het verfijnen van groeitechnieken voor enkelkristallijne BDD-elektroden en het verkennen van nieuwe toepassingen in biosensing en milieumonitoring. Deze dissertatie levert een belangrijke bijdrage aan het begrip en de ontwikkeling van BDD-elektroden en effent het pad voor hun verbeterde adoptie in geavanceerde elektrochemische sensortechnologieën.

LIST OF ABBREVIATIONS

AFM	Atomic Force Microscopy
AQDS	9,10-Anthraquinone-2,7-disulfonic Acid
BDD	Boron-Doped Diamond
CE	Counter Electrode
CV	Cyclic Voltammetry
CVD	Chemical Vapor Deposition
DPI	Dots Per Inch
DPV	Differential Pulse Voltammetry
EBSD	Electron Back-Scatter Diffraction
EIS	Electrochemical Impedance Spectroscopy
E_R	Reverse Potential
ET	Electron Transfer
FS-BDD	Freestanding Boron-Doped Diamond
FS-BDD-gr	Growth Side of FS-BDD
FS-BDD-nucl	Nucleation Side of FS-BDD
FS-BDD-pol	Polished Surface of FS-BDD
GCE	Glassy Carbon Electrode
HFCVD	Hot Filament Chemical Vapor Deposition
i_p	Peak Current
i_pc	Cathodic Peak Current
i_pa	Anodic Peak Current
MWCVD	Microwave Plasma Chemical Vapor Deposition
OCP	Open Circuit Potential
PDoS	Phonon Density of States
RE	Reference Electrode
RIE	Reactive Ion Etching
RSD	Relative Standard Deviation
SC-BDD	Single-Crystalline Boron-Doped Diamond
SECM	Scanning Electrochemical Microscopy
SEM	Scanning Electron Microscopy
SIMS	Secondary Ion Mass Spectrometry
v	Scan Rate
WE	Working Electrode
XPS	X-ray Photoelectron Spectroscopy
XRD	X-ray Diffraction
YSZ	Yttria-Stabilized Zirconia

1

1

INTRODUCTION

This chapter provides an overview of the fundamental properties of BDD electrodes and their application in electrochemical sensing. It highlights the limitations of existing research and identifies three key research objectives: understanding localized variations in electrochemical activity, evaluating the impact of sp^2 *carbon content and boron doping, and innovating BDD electrode fabrication through ink-jet printing. These objectives form the foundation for subsequent chapters, each addressing specific aspects of BDD electrode performance and fabrication.*

1.1. ELECTROCHEMICAL SENSORS

SENSORS have shaped our everyday lives owing to the world's growing need for quick, inexpensive, and trustworthy information. In broad terms, sensors are used as tools to detect events or changes in our environment. Of particular interest are electrochemical sensors, which are devices that detect analytes through electrical responses induced by chemical reactions. At their core, they operate by using electrodes as sensing elements [1]. When an analyte comes into contact with the electrode, it triggers a specific chemical reaction, leading to measurable electrical changes, such as variations in current, potential, or resistance. This direct induction of an electrical response by a chemical change enables the precise and rapid monitoring and analysis of various chemical substances.

Electrochemical sensors, known for their high sensitivity, rapid response times, portability, and low cost, have found widespread applications in fields such as environmental monitoring, industrial process control, agricultural analysis, safety surveillance, and healthcare. In environmental monitoring, they can detect pollutants in water, such as heavy metal ions and organic contaminants [2, 3]. These sensors assess environmental quality accurately and swiftly by measuring the current changes produced by pollutants reacting at the electrodes. In the field of industrial process control, electrochemical sensors are utilized for real-time monitoring of chemical reactions and substance concentrations on production lines, ensuring process stability and product quality. These sensors allow companies to adjust production parameters in real time, enhancing production efficiency and product quality [4]. For agriculture, the application of electrochemical sensors aids in achieving precision farming. They can detect soil pH, nutrients, and harmful substances, providing a scientific basis for precise fertilization, irrigation, and soil improvement, thus enhancing crop yield and quality [5–7]. In the field of safety monitoring, electrochemical sensors play a vital role in detecting hazardous gases (such as carbon monoxide or hydrogen sulfide) in homes and public places [8, 9]. These sensors respond quickly, issuing timely alerts to prevent potential health risks or safety incidents.

In healthcare, electrochemical sensors especially showcase their distinctive advantages. They are widely used to detect various biomarkers, chemicals, and ions, crucial for disease diagnosis, monitoring, and management. The range of detection includes, but is not limited to, cholesterol, cardiac markers (such as troponin and creatine kinase), infectious viruses, levels of electrolytes like potassium, sodium, calcium, and chlorine, as well as the pH of blood and other bodily fluids, exhaled gases, and blood glucose [10–17]. Among these, blood glucose monitoring is one of the most well-known applications of electrochemical sensors. They are used for monitoring blood glucose levels in diabetes patients, helping them manage their condition and prevent hyperglycemia or hypoglycemia. Particularly in the application of continuous glucose monitors, electrochemical sensors are revolutionizing the lives of diabetes patients. They operate as small sensors attached to the person's body and wirelessly transmit data to the patient's phone or other devices [18–20]. This real-time monitoring avoids the need for frequent finger-prick tests, significantly improving the patient's quality of life.

A schematic of a continuous electrochemical sensor placed on the skin is shown in Fig. 1.1 (a). Although these electrochemical sensors may differ in appearance, their core

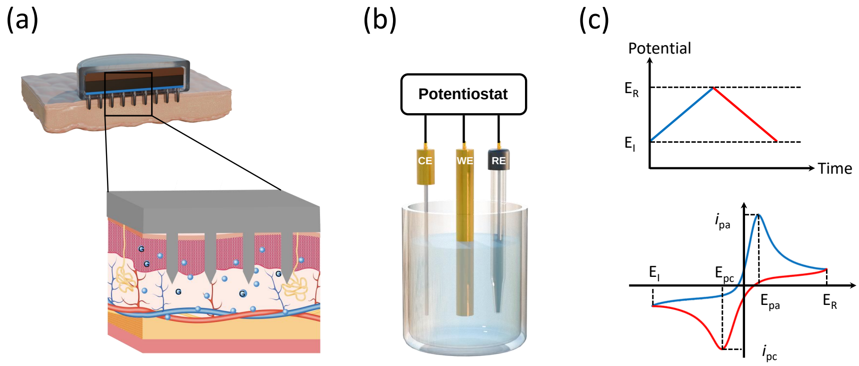

Figure 1.1: (a) A continuous electrochemical sensor mounted on the human skin; (b) The three-electrode system with working electrode (WE), counter electrode (CE), reference electrode (RE) and potentiostat; (c) Cyclic voltammetry with potential-time excitation signal (top image) and cyclic voltammogram for a reversible $\mathrm{Ox} + ne^- \leftrightarrow \mathrm{Red}$ reaction (lower image).

operating principle revolves around the use of a three-electrode system, consisting of a working electrode (WE), reference electrode (RE), and a counter electrode (CE), as shown in Fig. 1.1 (b). This system facilitates the flow of current between the WE and CE while maintaining a constant potential at the RE. The surface area of the CE should be much larger than that of the working electrode to prevent reactions on the WE from being restricted. Each electrode in the three-electrode system is connected to a potentiometer, ensuring that, with the coordination of a low-impedance ammeter and a high-impedance voltmeter at the counter electrode, no current passes directly through the RE, aiming for precise control and measurement of current and potential during the electrochemical reaction process [21].

A wide variety of materials can be used as the working electrode, ranging from metals such as gold, silver, and platinum to non-metals like graphene, conductive diamond, and glassy carbon [22, 23]. As the counter electrode, platinum wires or meshes are popular and also gold and graphite are frequently used. The RE contains a stable redox couple, with the concentration of each soluble component being saturated within the reference electrode to ensure its potential remains constant. Common REs include the saturated calomel electrode and the Ag/AgCl electrode [24]. The three electrodes are inserted into the same electrolyte solution, typically containing aqueous ionic salts (e.g., sodium chloride or potassium nitrate) to prevent ohmic drop.

In many cases within electrochemical sensors, pseudo-reference electrodes can be used in place of traditional REs, especially when the internal conditions of the electrochemical cell are known. Pseudo-reference electrodes, such as silver [25, 26], although not maintaining a constant potential, have predictable potential changes that occur with variations in the internal temperature or pH of the electrochemical cell, allowing for accurate studies of the system under a broader range of experimental conditions. Based on the signal transduction and detection mechanisms of electrochemical sensors, technologies are primarily categorized into potentiometry, voltammetry, and conductometry

[27]. Potentiometric sensors, in which the potential between two electrodes is measured using a high-impedance voltmeter, are widely used for on-site rapid testing due to their simple operation, high selectivity, and cost-effectiveness. In contrast, voltammetric sensors, which probe the current response of a chemical under an applied potential difference using a potentiostat, exhibit unique advantages in the quantitative analysis of analytes because of their superior sensitivity and faster response time. Additionally, there are sensors that detect changes in resistivity and capacitance, such as chemiresistors and capacitive sensors. These technologies identify and measure analytes by assessing changes in the impedance at the electrode interface [28].

Potential scanning technology is a cornerstone in the field of electrochemical research, with cyclic voltammetry (CV) being one of the most commonly utilized techniques. Starting from an open circuit potential (OCP) where no reaction occurs, an initial potential (E_{I}) is applied to the WE—typically at a stage where no electrochemical reaction occurs. The voltage at the working electrode is linearly altered from E_{I} at a predetermined scan rate (V/s) towards a designated reverse voltage (E_{R}), chosen based on the reaction being predominantly influenced by mass transfer. In linear scan voltammetry, the scan concludes upon reaching E_{R}, whereas CV extends the scan to E_{R} before reversing direction back to the start, thus completing a cycle in the voltammogram. This cyclic process, starting from the E_{I}, involves linear scanning in both anodic (oxidation) and cathodic (reduction) directions, leading to electron transfer and characteristically producing CV waveforms as shown in Fig. 1.1(c). As the potential is negatively driven from OCP, the rate of electron transfer (ET) in the reduction direction increases, causing an increase in current flow. Peaks form in the CV at maximum currents (i_{p}) for both anodic and cathodic scans, known as i_{pa} and i_{pc}, respectively [29].

The peak-to-peak separation between i_{pa} and i_{pc}, ΔE_{p}, is approximately 59 mV at T = 298 K for a reversible single-electron redox process [21], indicating fast electron transfer and thermodynamic equilibrium at the electrode surface. In contrast, under kinetic control, where the electron transfer rate is slower than mass transport, ΔE_{p} becomes larger, reflecting deviations from ideal reversibility. For macroelectrodes, a subsequent decline in current is typically observed after reaching the peak current (i_{p}), due to the limited mass transport rate of redox species that cannot sufficiently replenish those consumed at the electrode surface—highlighting diffusion-controlled behavior.

Under the assumptions of semi-infinite planar diffusion and negligible electron-transfer kinetic limitations, the peak current observed in a diffusion-controlled cyclic voltammogram can be described by the Randles–Ševčík equation (Equation 1.1):

$$i_{\mathrm{p}} = 0.4463\, nFAC \left(\frac{nFvD}{RT} \right)^{1/2} \tag{1.1}$$

where:

- n equals the number of electrons transferred,
- F is Faraday's constant (96485 C/mol),
- A is the total surface area of the electrode (cm^2),
- C is the volume concentration of the electroactive species ($\mathrm{mol/cm}^3$),

- v is the scan rate of the potential (V/s),
- D is the diffusion coefficient of the electroactive species (cm^2/s),
- R is the molar gas constant (8.3145 J/mol · K),
- T is the temperature (K).

The current observed is a combination of two processes occurring at the electrode surface: Faradaic and non-Faradaic processes [21]. Faradaic processes involve the reduction and oxidation of chemical species in solution through electron exchange at the electrode interface. In contrast, non-Faradaic currents do not involve charge transfer across the interface but stem from changes at the electrode/solution interface. Examples of non-Faradaic processes include the capacitance of the electrode material and the formation of the electric double layer.

1.2. BORON-DOPED DIAMOND (BDD): SYNTHESIS AND ITS UNIQUE ADVANTAGES TO ELECTROCHEMICAL SENSING

The application of boron-doped diamond (BDD) as an electrode material in electrochemical sensors has rapidly increased over the past 20 years [30]. BDD electrodes are known for their broad electrochemical activity window, enabling their operation over a vast range of potentials without water electrolysis. This feature significantly reduces the influence on background and capacitive currents, leading to a cleaner signal output [31]. Moreover, these electrodes are characterized by exceptional chemical and mechanical stability, making them highly resistant to chemical corrosion and physical wear. Such durability proves invaluable for their sustained use over time. In the application of electrochemical analysis, BDD electrodes are known for achieving low detection limits and exhibiting excellent low-fouling capabilities, which are critical for maintaining analytical consistency and reliability [32]. Additionally, the strong biocompatibility of BDD electrodes highlights their appropriateness for electrochemical sensing tasks related to human health, marking them as a beneficial choice in the field [33, 34].

Natural diamonds are optically transparent, extremely hard, have unique insulating features, a broad range of semiconductor behavior, and are highly resistant to electricity [35, 36]. The transformation of diamonds into functional electrodes is achieved through the process of doping, specifically with boron. The incorporation of boron atoms into the diamond lattice introduces additional holes, thereby serving as charge carriers. When doping levels are significantly increased ($> 10^{20}$ B atoms cm^{-3}), reaching electrically conductive or “metal-like” BDD, the energy levels created by the doping merge with the diamond’s valence band. This integration results in the valence band being partially occupied by electronic energy levels, ensuring the movement of charge carriers (holes) and preserving high conductivity.

The development of BDD electrodes was a gradual achievement. In 1954, researchers at the General Electric Company broke new ground with the High-Pressure High-Temperature (HPHT) method for creating synthetic diamonds, setting the stage for subsequent innovations [37]. The emergence of Chemical Vapor Deposition (CVD) technology, closely linked to the production of BDD, represented a significant breakthrough. Initiated in the early 1980s by researchers like John Angus, CVD diamond research quickly gained momentum [31]. The CVD method involves breaking down carbon-rich gases at high temperatures to deposit diamond films onto substrates. The precision in controlling impurity levels and film thickness offered by CVD technology has markedly improved the electrical and electrochemical characteristics of the resulting materials. These enhancements have expanded the range of applications for BDD electrodes, including their use in electrochemical sensors.

The synthesis of BDD by the CVD technique starts with the preparation of a substrate, which is cleaned and placed inside a vacuum chamber. The selection of the right substrate is crucial for maintaining stability under the conditions used to grow the diamond material. Preparing the substrate surface through methods like abrasion, seeding with diamond nanoparticles, or applying an electrical bias plays a key role in increasing the number of nucleation sites. This, in turn, helps in the effective formation of diamond.

The CVD process unfolds through several main steps: gas phase preparation, energy excitation, and the combined actions of deposition and doping. Carbon-rich precursor gases, notably methane, blended with excess hydrogen, create the reactive environment, with boron sources added to the mix as doping agents. Energy excitation, typically achieved using hot filaments or plasma, facilitates the breakdown of these gases, releasing active boron and carbon species. These species (particularly atomic/molecular radicals) subsequently adhere to the substrate, culminating in the formation of a diamond film. The integration of boron atoms within the diamond's structure imparts p-type semiconductor properties to the film. While the Hot Filament CVD (HFCVD) method enjoys widespread adoption among commercial BDD electrode producers for its scalability [38], the use of Microwave Plasma CVD (MWCVD) [39] is widespread in academia. The plasma-based approach enables the attainment of superior phase purity and expedited growth rates of diamond [38].

The grain size in BDD films is dictated by a number of factors, including the duration of growth, temperature, pressure, gas mixture, and the incorporation of inert gases like argon. BDD films are classified into ultra-nanocrystalline, nanocrystalline, microcrystalline, and single-crystal categories, each defined by its grain size and exhibiting distinct characteristics essential for specific applications. The crystal orientation, notably the (111), (110), and (100) directions, plays a crucial role in boron incorporation and doping efficacy, underscoring the significance of achieving uniform doping across (polycrystalline) diamond.

During the synthesis of BDD, sp^2-bonded carbon growth occurs at the grain boundaries, although it may also arise during individual growth phases. The occurrence of sp^2 carbon is especially pronounced in ultra-nanocrystalline and nanocrystalline BDD, where the boundary density far exceeds that in microcrystalline BDD. As the concentration of boron increases, the challenge of preventing sp^2 carbon formation intensifies. When the conditions for growing diamonds are kept stable, the size of the diamond crystals and the thickness of the overall diamond film grow with increased growth time. By setting just the right conditions for growing microcrystalline BDD (especially a high ratio of hydrogen to methyl radicals), it is possible to create nanocrystalline BDD thin films that have less sp^2 carbon [40]. Interestingly, ultra-nanocrystalline and nanocrystalline films, which are typically very thin (less than a few microns), stick to the surface they are grown on, making them easier to handle. On the other hand, the thicker microcrystalline films (hundreds of microns and beyond) can be detached from their growth substrate, and are often used as free-standing BDD electrodes.

For growing single-crystal BDD (SC-BDD) using CVD, employing single-crystal diamond substrates promotes homoepitaxial growth. These substrates are typically prepared through the HPHT method. In the synthesis of SC-BDD via CVD, understanding the growth mechanism is crucial for refining electrode growth conditions to reduce defect density and impurity levels. While the body of research work on SC-BDD may not be as advanced as its polycrystalline counterpart, progress in growth techniques has led to the production of large-area SC-BDD, owning wide advantages compared with polycrystalline BDD [41–43].

1.3. BORON-DOPED DIAMOND (BDD): MATERIAL PROPERTIES AND THEIR EFFECTS ON ELECTROCHEMICAL RESPONSE

BDD is considered a designer material [44]. Depending on the growth method and subsequent treatment of the BDD, the resulting material properties can vary significantly among different BDD electrodes. To understand the material attributes of the BDD electrodes and to derive useful comparisons between data in the literature, four main material parameters of the electrode should be considered: boron doping level, sp^2 carbon content, crystal orientation, and surface termination. This section provides an overview of reported approaches to controlling these material parameters as well as the effects that these factors have on the electrochemical response of the BDD electrode.

1.3.1. BORON DOPING LEVEL

The bandgap-width of diamond is 5.47 electron volts (eV) at 300 K [45], rendering it highly electrically insulating. Boron atoms have atomic radii very close to those of carbon atoms, allowing them to substitute carbon atoms and integrate well into the diamond lattice. Boron atoms possess only three valence electrons, whereas carbon atoms have four. This creates holes in the diamond lattice, serving as charge carriers and enabling electrons to jump from one atom to another, thus facilitating conductivity.

The conductivity of BDD increases with the concentration of boron doping. Ekimov et al. reported that low boron concentrations ($n = 10^{17}$–10^{19} $\mathrm{cm^{-3}}$) impart p-type semiconductor characteristics to diamond with an activation energy of approximately 0.35 eV [46]. Continuing to increase the boron doping level in the material exhibits hopping transport characteristics until the doping level exceeds 10^{20} $\mathrm{cm^{-3}}$, achieving metal-like conductivity near room temperature. In most research involving BDD electrochemical sensing, the boron doping level used is typically higher than 10^{20} $\mathrm{cm^{-3}}$ [47].

For determining the boron doping level in the BDD electrode, secondary ion mass spectrometry (SIMS) offers extremely high sensitivity and accuracy, making it the most common analysis method [47]. SIMS works by bombarding the BDD electrode surface with a focused high-energy ion beam, causing atoms on the BDD surface to be ejected, some of which are ionized into secondary ions. These secondary ions are then separated by a mass spectrometer and identified based on their mass-to-charge ratio (m/z), enabling precise determination of the boron concentration in the sample. Recent studies have also confirmed that Raman spectroscopy can be used to accurately estimate the boron doping of BDD [48, 49]. Boron atoms integrate into the diamond crystal lattice and alter the vibrational modes (phonons), which leads to a red shift (lower frequency) and broadening of the Raman spectral peaks. The introduction of boron causes interactions between phonons and free carriers, producing Fano resonance, which results in asymmetric peak shapes in the Raman spectrum. By analyzing these changes, particularly the shift, broadening, and asymmetry of the zero-phonon line (ZCP) and the phonon density of states (PDoS) peaks, the boron atomic concentration can be accurately estimated [48].

For SC-BDD, the boron doping level can also be estimated by measuring the charge carrier density through Mott-Schottky plots (the reciprocal of the square of capacitance, $1/C^2$, versus the potential difference between the electrode and electrolyte) in an electrolyte solution. Due to the minimal impurities in SC-BDD, the charge carrier density obtained from Mott-Schottky plots closely approximates the true boron doping levels. However, in polycrystalline BDD, which contains numerous defects and impurities that trap many charge carriers, the number of charge carriers involved in electron transfer is lower than the corresponding hole numbers derived from SIMS for assessing boron doping levels. Therefore, the measurement of charge carrier density merits attention, as even with consistent boron doping levels, other factors such as grain size, crystal orientations, and grain boundary densities can cause variations in the electrode surface's charge carrier densities, influencing its electrochemical performance differently [50, 51].

The boron doping level significantly influences the performance of BDD as an electrode in electrochemical sensing applications. Most current studies on boron doping levels utilize BDD with varying boron concentrations, achieved by controlling the ratio of boron source gas to carbon source gas during the CVD growth process [52]. However, increasing the concentration of boron source gas in the reactant gases tends to decrease the growth rate of BDD grown via CVD [51, 53, 54], which may be due to the boron incorporation mechanism and the presence of boron interfering with the preferred sites for carbon attachment [55]. Another aspect directly related to the boron doping level is the surface morphology of BDD. Numerous studies have pointed out that, with the increase in the concentration of boron source gas during the CVD growth process, significant changes occur in the BDD's surface morphology, including a reduction in grain size and an increase in grain boundary densities [51, 52, 54, 56, 57]. This is attributed to the excessive boron doping, where an abundance of boron atoms congregates near the boundaries, inducing more structural defects that hinder the growth of diamond grains. Additionally, more boron atoms lead to a considerable amount of secondary nucleation and facilitate the emergence of twinning phenomena on the diamond surface, thereby decreasing the average grain size [47, 54].

1.3.2. SP^2 CARBON CONTENT

In electrochemical applications, particularly for electrochemical sensing, electrodes with higher boron concentrations are often preferred due to their enhanced electrical conductivity and the high density of charge carriers on the electrode surface. However, as mentioned above, heavy boron doping under commonly used growth conditions leads to an increase in grain boundaries. It is at these boundaries that sp^2-bonded carbon impurities are commonly found. These sp^2 carbon sites typically exhibit properties similar to those of glassy carbon electrodes and possess electrochemical activity [58, 59]. It should be noted that highly doped BDD with negligible sp^2 carbon content can also be achieved by optimizing MW-CVD growth conditions [60].

The properties of BDD as an electrode material are primarily defined by two critical factors: the boron doping level and the sp^2 carbon content. As highlighted in the first paragraph of section 1.2, compared to conventional electrodes, BDD electrodes exhibit broader water potential windows and lower background currents. This is attributed to the catalytically inert nature of BDD's sp^3-bonded carbon surface, which lacks the catalytic sites necessary for the inner-sphere ET reactions of water electrolysis. On the other hand, the sp^2 carbon is more conductive, enhancing local current density on the electrode surface and facilitating water molecule electrolysis [47]. Therefore, the width of the BDD water potential window is often determined by the content of sp^2 carbon. In many polycrystalline BDD systems grown under standard conditions, increased boron doping leads to smaller BDD grains, a higher density of grain boundaries, and a greater amount of sp^2 carbon, which narrows the water potential window [61].

In electrochemical sensor applications, it is widely recognized that BDD electrodes with higher doping levels are more effective. Previous studies have shown that increasing the boron doping level enhances the electrochemical sensitivity for various analytes, including dopamine, ascorbic acid, organic molecules with a benzene ring (phenol, hydroquinone, catechol, and resorcinol), uric acid, and nitrate [52, 57, 62, 63]. However, there is no consensus on the impact of sp^2 carbon on the performance of BDD in electrochemical sensing. The presence of sp^2 carbon in BDD has been considered an inherent issue in electrochemical applications due to a reduction in the water potential window and an increase in background current, potentially affecting the limit of detection [64, 65]. Nonetheless, some studies have suggested that adding sp^2 carbon impurities to highly doped BDD is beneficial for applications requiring electrode activity [59, 66]. Isolating the effect of sp^2 carbon on electrochemical sensor applications has been challenging. This is because altering growth conditions to study the sole impact of sp^2 carbon can also affect other factors, such as surface roughness and boron doping level.

1.3.3. CRYSTAL ORIENTATION

Beyond boron doping level and sp^2 carbon content, the crystal orientation of BDD also significantly affects the electrochemical performance. For polycrystalline BDD electrodes, noticeable differences in electrochemical properties among various grain orientations are often observed. Revealing the relationship between grain orientation and electrochemical behaviour is crucial for fully realizing the potential of BDD in various applications, especially in electrochemical sensors. To this end, Pleskov et al. prepared (111)-, (110)-, and (100)-oriented single-crystal BDD electrodes through homoepitaxial CVD growth with the same boron/carbon ratio in the gas phase [67]. Electrochemical studies showed that in the $[Fe(CN)_6]^{3-/4-}$ and $[Ru(NH_3)_6]^{2+/3+}$ redox systems, the electrochemical activity of the three electrodes decreased in the following order: (111) > (110) > (100). The variation in the electrochemical activity across crystal orientations was attributed to the varying boron incorporation efficiency during the CVD process, which decreased in the same following order: (111) > (110) > (100) [67]. During the CVD process, using the same boron/carbon ratio in the gas phase, the boron concentration on (111) surfaces is about an order of magnitude higher compared to the (100) orientation [68, 69]. This higher boron dopant density present on the (111) facet was further confirmed by Ando et al., who successfully characterized the electrochemical properties of different facets of a single BDD particle, revealing significantly faster electron-transfer kinetics on the (111) facet compared to the (100) facet [70]. Consequently, boron atoms are distributed unevenly across the polycrystalline BDD surface, creating domains with varying doping levels, thus leading to a mosaic of conductivities (ranging from insulating to semiconducting to metal-like) and electrochemical activities.

Pleskov et al. concluded that the electrochemical kinetic differences between differently oriented diamond crystal faces can be eliminated if the acceptor concentration (boron) in the electrodes is the same [67]. They prepared (111)- and (100)-oriented single-crystal BDD electrodes with similar doping levels and compared the electron transfer kinetics within the $[Fe(CN)_6]^{3-/4-}$ and $[Ru(NH_3)_6]^{2+/3+}$ redox systems, indicating that the crystallographic orientation had a negligible effect [67].

In addition to studying single-crystal BDD electrodes with different grain orientations, researchers have used scanning electrochemical microscopy (SECM) to more directly investigate the impact of different grain orientations on the electrochemical properties of polycrystalline BDD surfaces. SECM microelectrode probes scan the BDD electrode surface, recording current signals at different positions to precisely measure local variations in surface electrochemical reactions. This technique provides high-resolution images of electrochemical activity, revealing the heterogeneity of BDD electrode surfaces. Holt et al. were the first to report SECM imaging of BDD electrodes using $[Ru(NH_3)_6]^{2+/3+}$ and they found that not all parts of the electrode exhibited electrochemical activity [71]. Even on the polished surface of heavily doped BDD electrodes (2×10^{20} B cm^{-3}), predominantly insulating and electrochemically non-active areas were observed [71]. SECM images suggested that the conductive and electrochemically active sites were primarily located at grain boundaries. Wilson et al. also studied highly doped BDD electrodes (5×10^{20} B cm^{-3}) using SECM and observed similar electrochemical heterogeneity on the BDD surface [72]. They attributed the variation in boron uptake among individual grains to the uneven boron doping levels at grain boundaries, resulting in different electrochemical performances. However, they did not find a significant enhancement of conductivity at the grain boundaries [72].

Holt et al. were the first to report SECM of BDD electrodes using $[Ru(NH_3)_6]^{2+/3+}$ and they found that not all parts of the electrode exhibited electrochemical activity [71]. Even on the polished surface of heavily doped BDD electrodes (2×10^{20} B cm^{-3}), regions exhibiting strongly suppressed electron-transfer activity were observed [71], rather than truly electrically insulating behavior. It should be noted that such observations were reported in early SECM studies, and later work on highly doped BDD electrodes has suggested more homogeneous electron-transfer behavior at the micrometer length scale.

By adjusting various parameters during the CVD preparation process, such as substrate temperature, gas composition, and film thickness, a predominantly (111)-oriented BDD electrode surface can be achieved [73–75], enhancing the electrode's surface activity. Dettlaff et al. prepared a new type of highly oriented (111) textured boron-doped diamond electrode using deuterium-rich microwave plasma CVD instead of a hydrogen chemistry [76]. This highly oriented diamond surface exhibited improved boron doping and activation, while the crystals displayed enhanced electron carrier acceptance and donation, accelerating ET in electrochemical processes. Therefore, for the application of BDD electrodes in electrochemical sensors, controlling the crystal surface orientation of the electrode is crucial.

1.3.4. SURFACE TERMINATION

Surface termination is the fourth key factor determining the electrochemical properties of BDD electrodes. Unlike boron doping level, sp^2 carbon content, and crystal orientation, the surface termination can be relatively easily altered through chemical reactions. This ease of modification makes it convenient for optimizing BDD electrodes for electrochemical sensor applications. However, it is important to recognize that surface terminations might change during practical use, potentially deviating from the intended design. Therefore, understanding the types of surface terminations, methods to modify them, and their specific effects on electrochemical properties is crucial for the effective application of BDD electrodes in electrochemical sensors.

Newly prepared BDD electrodes typically have a hydrogen-terminated surface, as they are manufactured in a hydrogen environment through CVD. This hydrogen-terminated surface can remain stable for weeks to months, largely depending on the electrode's frequency of use in electrochemical experiments, and eventually transitions to oxygen termination [77].

There are three common methods to achieve a hydrogen-terminated surface: heating the BDD electrode in a hydrogen atmosphere, where high-temperature hydrogen reacts with the BDD surface to remove oxides and other non-hydrogen functional groups [78]; placing the BDD electrode in a hydrogen plasma reactor, where the high reactivity of hydrogen atoms and ions under plasma conditions effectively removes surface oxides and other functional groups, replacing them with hydrogen atoms [60]; and a simpler method, cathodic reduction hydrogenation, where the electrode's surface condition is directly related to the applied electrochemical conditions, especially the concentration of H^+ ions and the applied negative potential. More precisely, using a solution with a lower pH value and more negative potential results in an increased degree of surface hydrogenation [79]. It should be emphasized that, under electrochemical conditions accessible to standard potentiostats, cathodic reduction does not fully hydrogenate the BDD surface but instead produces partial hydrogen termination, which has been shown to be sufficient for activating BDD electrodes for electrochemical measurements [80]. The third method has shown high practical value in electrochemical research, especially for electrochemical sensing studies, where a reproducible and sufficiently hydrogenated surface termination is crucial. Thus, conducting a standard pretreatment of the electrode before every electrochemical sensing experiment can make the results more reliable and reproducible. Intentional transitioning from H-termination to O-termination can be done by various techniques, including boiling in acid, alumina polishing, exposure to oxygen plasma, photochemical oxidation, reacting with oxygen at high temperatures, and anodic polarization [81–84].

The impact of surface termination on the electrochemical properties of the BDD electrode is evident. First, the surface termination influences the wettability of the electrode. Freshly prepared BDD, just coming out of the CVD reactor, is hydrogen-terminated. At this stage, the BDD surface exhibits hydrophobic properties, with a water contact angle reaching up to 90° [85]. This hydrophobicity helps reduce surface contamination by making it difficult for organic substances to adhere to the hydrophobic surface, thereby keeping the electrode clean and enhancing its stability and lifespan in electrochemical sensor applications [86]. When the hydrogen terminations on the electrode surface are converted to oxygen terminations, the contact angle decreases, making the BDD electrode surface more hydrophilic. This increased hydrophilicity improves the wettability and contact efficiency of the electrolyte solution on the electrode surface, enhancing its sensitivity in electrochemical sensor applications.

Furthermore, when the BDD electrode surface is hydrogen-terminated, the energy levels of both the valence band and conduction band are raised. Since the conduction band level is above the vacuum level, it creates a negative electron affinity, which means electrons can escape from the surface more easily. The increased ET efficiency facilitates faster kinetics in inner-sphere redox processes, thereby enhancing reaction rates. In contrast, oxygen termination lowers the valence and conduction band energy levels, resulting in positive electron affinity. This makes it more difficult for electrons to escape from or be injected into the BDD surface, reducing the efficiency of ET between the electrode and redox species. Consequently, the kinetics of inner-sphere redox processes slow down, leading to a decrease in reaction rates [87, 88].

When considering the applications of BDD electrodes in electrochemical sensors, it is natural to favor a more conductive surface. Specifically, hydrogen-terminated surfaces are preferred over oxygen-terminated ones because they facilitate more efficient ET. Higher conductivity leads to faster response to applied voltage and improved signal transmission efficiency in the sensors. For instance, Ivandini et al. studied the application of hydrogen-terminated and oxygen-terminated BDD electrodes in the electrochemical detection of oxalic acid [89]. They observed a distinct oxidation peak on the hydrogen-terminated BDD electrode, while no peak was detected on the oxygen-terminated electrode [89]. However, for electrochemical sensors, in addition to requiring high electron transfer kinetics, selectivity is also crucial. In this regard, Tryk et al. investigated the ability of BDD electrodes to detect dopamine in the presence of ascorbic acid [90]. They found that dopamine and ascorbic acid oxidized at nearly the same potential on hydrogen-terminated surfaces, but the oxidation potential of ascorbic acid shifted significantly on oxygen-terminated surfaces, allowing for their separate detection. Therefore, in practical applications of electrochemical sensors, the choice of surface termination depends on the analyte to be detected. It requires consideration of not only higher ET efficiency but also factors like selectivity, background current, and limit of detection to determine the optimal surface termination [90].

1.4. RESEARCH OBJECTIVES

The overarching aim of this research is to advance the understanding of BDD electrodes in electrochemical sensing and to contribute to innovations in BDD manufacturing for sensor applications. The following three specific objectives have been formulated:

- To investigate the localized variations in electrochemical activity of polycrystalline BDD electrodes. This objective focuses on the heterogeneity in microstructure-electroactivity relationships of BDD. Using techniques like scanning electron microscopy (SEM), Raman spectroscopy, and SECM, this study will map out how crystallographic orientation, sp^2 carbon content, and boron doping influence the electrochemical response. The objective ties into the literature's gap regarding how surface features like crystal orientation impact local electrochemical activity, a crucial factor for improving sensor performance.
- To assess the effect of critical properties (such as sp^2 carbon content and boron doping) on the efficacy of BDD electrodes in electrochemical sensing applications. This objective builds on the first by comparing single-crystal and polycrystalline BDD to examine their potential in detecting biologically relevant molecules like glucose and dopamine. The research will focus on understanding how different levels of sp^2 carbon and boron doping affect catalytic activity and anti-fouling properties. The outcomes will provide insights into optimizing BDD electrodes for real-world applications in biosensing.
- To innovate the fabrication of BDD sensing chips through inkjet printing technology. This objective aims to explore the use of inkjet printing for the production of BDD electrodes, optimizing ink composition, substrate preparation, and printing resolution. A comparative study will evaluate the electrochemical performance of inkjet-manufactured BDD against commercially available screen-printed versions. This approach addresses the existing limitations in manufacturing scalable, high-performance BDD sensor chips.

These objectives will provide a comprehensive understanding of the relationships between the material properties of BDD and their electrochemical behaviour, thereby contributing to the development of more efficient and scalable BDD-based electrochemical sensors.

1.5. RESEARCH OUTLINE

Chapter 1 of this thesis primarily focuses on reviewing existing literature on the fundamental properties of BDD electrodes. This chapter extensively discusses the use of BDD electrodes in electrochemical sensing and addresses the limitations found in previous studies related to BDD sensor electrodes. From a thorough review of past literature, three key research objectives are identified. The detailed research methods and results are presented in Chapters 2, 3, 4, and 5, each based on a published journal paper. Due to this structure, some repetition, especially in chapter introductions, is unavoidable.

Chapter 2 examines the first research objective: the heterogeneity of polycrystalline BDD electrodes. The electrodes studied were thick, freestanding BDD with both polished nucleation and growth surfaces. Various mapping techniques were used for visual representation of the heterogeneity in both microstructure and electroactivity. SEM was used to show the morphology of different electrode areas. Electron backscatter diffraction (EBSD) created orientation and boundary maps, identifying and quantifying primary and secondary twinning. Raman imaging mapped the distribution of sp^3 and sp^2

carbon, along with boron dopants on the BDD surface. Additionally, SECM mapping with an outer-sphere redox couple, $\mathrm{FcMeOH}^{+/0}$, was performed on the polished growth surface of the BDD electrodes to identify conductive and electrochemically active areas. Combining EBSD, Raman, and SECM mapping revealed the local electrochemical activity in relation to surface features like crystal orientation, twin boundary, and composition.

Chapters 3 and 4 systematically delve into the second research objective. Chapter 3 focuses on the influence of sp^2 carbon content in BDD on its electrochemical properties as an electrode material, using BDD surfaces of varying thickness to control sp^2 carbon levels and electrochemical methods to confirm them. The research in Chapter 3 is centered on the effect of sp^2 carbon towards the non-enzymatic electrochemical detection of glucose. Chapter 4 involves synthesizing large-area (1 cm^2) and heavily doped ($[B] > 10^{21}\ \mathrm{cm}^{-3}$) (100)-oriented single-crystal BDD electrodes using heteroepitaxial growth. Three single-crystal diamond samples with different surface morphologies were prepared, and the electrochemical properties of BDD layers grown on these heteroepitaxial diamond quasi-substrates were investigated and compared to conventional polycrystalline BDD. Cyclic voltammetry in solutions with supporting electrolyte (0.1 M KNO_3) and two redox probes was used to assess critical electrochemical characteristics, while SECM was employed to probe the electrochemical activity distribution of the single- and polycrystalline BDD surfaces. Finally, the various heteroepitaxial single-crystal BDD electrodes were tested with complex organic molecules like dopamine and anthraquinone-2,6-disulfonate (AQDS) to evaluate their sensing potential and anti-fouling properties.

Chapter 5 explores the third research objective, focusing on a novel fabrication process for BDD electrochemical sensor chips. A bottom-up approach for BDD sensor chip production is described, involving selective-area seeding via direct inkjet printing of nanodiamond particles. The seeding process, using a research inkjet printer, was optimized, focusing on the composition of the homemade diamond ink, substrate pretreatment, and printing parameters. The inkjet-seeded substrate underwent an MWCVD growth step to form miniaturized thin-film BDD working and counter electrodes. Silver ink was then inkjet-printed to complete the three-electrode sensor chip with a reliable reference electrode. The electrochemical performance of the new chip-based BDD electrodes was tested with redox markers and various organic molecules, including glucose, ascorbic acid, uric acid, dopamine, and tyrosine, and compared with commercial screen-printed BDD electrodes.

Finally, in Chapter 6, the conclusions of this research are outlined, and an outlook on future research is provided.

BIBLIOGRAPHY

[1] J. Wang, *Analytical electrochemistry*, 3rd (John Wiley & Sons, 2006), pp. 1–250.

[2] B. K. Bansod, T. Kumar, R. Thakur, S. Rana, and I. Singh, "A review on various electrochemical techniques for heavy metal ions detection with different sensing platforms", Biosensors and Bioelectronics **94**, 443–455 (2017).

[3] M. H. Hassan, R. Khan, and S. Andreescu, “Advances in electrochemical detection methods for measuring contaminants of emerging concerns”, Electrochemical Science Advances **2**, e2100184 (2022).

[4] J. Wang, “Real-time electrochemical monitoring: toward green analytical chemistry”, Accounts of Chemical Research **35**, 811–816 (2002).

[5] M. A. Eldeeb, V. N. Dhamu, A. Paul, S. Muthukumar, and S. Prasad, “Espial: electrochemical soil pH sensor for in situ real-time monitoring”, Micromachines **14**, 2188 (2023).

[6] G. Ozcelikay, L. Karadurmus, S. Bilge, A. Sinağ, and S. A. Ozkan, “New analytical strategies amplified with 2d carbon nanomaterials for electrochemical sensing of food pollutants in water and soils”, Chemosphere **296**, 133974 (2022).

[7] M. Nadporozhskaya, N. Kovsh, R. Paolesse, and L. Lvova, “Recent advances in chemical sensors for soil analysis: a review”, Chemosensors **10**, 35 (2022).

[8] C. Duc, M. L. Boukhenane, J. L. Wojkiewicz, and N. Redon, “Hydrogen sulfide detection by sensors based on conductive polymers: a review”, Frontiers in Materials **7**, 556223 (2020).

[9] S. You, G. Li, Z. Fan, X. Li, L. Fu, and W. Wu, “Nanotechnology-assisted sensors for the detection of carbon monoxide: a review”, International Journal of Electrochemical Science **18**, 100314 (2023).

[10] M. Amiri and S. Arshi, “An overview on electrochemical determination of cholesterol”, Electroanalysis **32**, 1391–1407 (2020).

[11] R. D. Crapnell, A. G. M. Ferrari, N. C. Dempsey, and C. E. Banks, “Electroanalytical overview: screen-printed electrochemical sensing platforms for the detection of vital cardiac, cancer, and inflammatory biomarkers”, Sensors & Diagnostics **1**, 405–428 (2022).

[12] P. Pirovano, M. Dorrian, A. Shinde, A. Donohoe, A. J. Brady, N. M. Moyna, G. Wallace, D. Diamond, and M. McCaul, “A wearable sensor for the detection of sodium and potassium in human sweat during exercise”, Talanta **219**, 121145 (2020).

[13] M. T. Ghoneim, A. Nguyen, N. Dereje, J. Huang, G. C. Moore, P. J. Murzynowski, and C. Dagdeviren, “Recent progress in electrochemical ph-sensing materials and configurations for biomedical applications”, Chemical Reviews **119**, 5248–5297 (2019).

[14] S. Das and M. Pal, “Review—non-invasive monitoring of human health by exhaled breath analysis: a comprehensive review”, Journal of the Electrochemical Society **167**, 037562 (2020).

[15] H. Teymourian, A. Barfidokht, and J. Wang, “Electrochemical glucose sensors in diabetes management: an updated review (2010–2020)”, Chemical Society Reviews **49**, 7671–7709 (2020).

[16] B. P. Kunnel and S. Demuru, “An epidermal wearable microfluidic patch for simultaneous sampling, storage, and analysis of biofluids with counterion monitoring”, Lab on a Chip **22**, 1793–1804 (2022).

[17] D. P. Ghumra, N. Shetty, K. R. McBrearty, J. V. Puthussery, B. J. Sumlin, W. D. Gardiner, B. M. Doherty, J. P. Magrecki, D. L. Brody, T. J. Esparza, J. A. O'Halloran, R. M. Presti, T. L. Bricker, A. C. M. Boon, C. M. Yuede, J. R. Cirrito, and R. K. Chakrabarty, "Rapid direct detection of SARS-CoV-2 aerosols in exhaled breath at the point of care", ACS Sensors **8**, 3023–3031 (2023).

[18] D. Olczuk and R. Priefer, "A history of continuous glucose monitors (CGMs) in self-monitoring of diabetes mellitus", Diabetes Metabolic Syndrome: Clinical Research Reviews **12**, 181–187 (2018).

[19] J. I. Joseph, "Review of the long-term implantable senseonics continuous glucose monitoring system and other continuous glucose monitoring systems", Journal of Diabetes Science and Technology **15**, 167–173 (2020).

[20] D. J. DeSalvo, N. Noor, C. Xie, S. D. Corathers, S. Majidi, R. J. McDonough, S. Polsky, R. Izquierdo, N. Rioles, R. Weinstock, K. Obrynba, A. Roberts, F. Vendrame, J. Sanchez, and O. Ebekozien, "Patient demographics and clinical outcomes among type 1 diabetes patients using continuous glucose monitors: data from t1d exchange real-world observational study", Journal of Diabetes Science and Technology **17**, 322–328 (2023).

[21] A. J. Bard and L. R. Faulkner, *Electrochemical methods: fundamentals and applications*, 2nd ed. (John Wiley Sons, 2001), p. 864.

[22] F. Terzi, L. Pigani, and C. Zanardi, "Unusual metals as electrode materials for electrochemical sensors", Current Opinion in Electrochemistry **16**, 157–163 (2019).

[23] A. C. Power, B. Gorey, S. Chandra, and J. Chapman, "Carbon nanomaterials and their application to electrochemical sensors: a review", Nanotechnology Reviews **7**, 19–41 (2018).

[24] G. A. East and M. A. D. Valle, "Easy-to-make Ag/AgCl reference electrode", Journal of Chemical Education **77**, 97 (2000).

[25] R. Šelešovská, T. Navrátil, V. Hrdlička, P. Michniak, M. Hatala, M. Vojs, M. Marton, O. Matvieiev, L. Janíková, and J. Chýlková, "Novel screen-printed sensors with chemically deposited boron-doped diamond and their use for voltammetric determination of attention deficit hyperactivity disorder medication atomoxetine", Electrochimica Acta **403**, 139642 (2022).

[26] J. R. Camargo, W. S. Fernandes-Junior, D. C. Azzi, R. G. Rocha, L. V. Faria, E. M. Richter, R. A. A. Muñoz, and B. C. Janegitz, "Development of new simple compositions of silver inks for the preparation of pseudo-reference electrodes", Biosensors **12**, 761 (2022).

[27] J. F. Vetelino and A. Reghu, *Introduction to sensors* (CRC Press, 2017), pp. 1–180.

[28] J. O. Carneiro, A. Ribeiro, F. Miranda, I. R. Segundo, S. Landi, V. Teixeira, and M. F. M. Costa, "Development of capacitive-type sensors by electrochemical anodization: humidity and touch sensing applications", Sensors **21**, 7317 (2021).

[29] N. Elgrishi, K. J. Rountree, B. D. McCarthy, E. S. Rountree, T. T. Eisenhart, and J. L. Dempsey, "A practical beginner's guide to cyclic voltammetry", Journal of Chemical Education **95**, 197–206 (2018).

[30]S. Baluchova, A. Danhel, H. Dejmkova, V. Ostatna, M. Fojta, and K. Schwarzova-Peckova, "Recent progress in the applications of boron doped diamond electrodes in electroanalysis of organic compounds and biomolecules - a review", Analytica Chimica Acta **1077**, 30–66 (2019).

[31]M. H. S. McLaughlin, E. Corcoran, A. C. Pakpour-Tabrizi, D. C. de Faria, and R. B. Jackman, "Influence of temperature on the electrochemical window of boron doped diamond: a comparison of commercially available electrodes", Scientific Reports **10**, 1–9 (2020).

[32]Y. Einaga, "Diamond electrodes for electrochemical analysis", Journal of Applied Electrochemistry **40**, 1807–1816 (2010).

[33]K. H. Yang and R. J. Narayan, "Biocompatibility and functionalization of diamond for neural applications", Current Opinion in Biomedical Engineering **10**, 60–68 (2019).

[34]M. Alcaide, A. Taylor, M. Fjorback, V. Zachar, and C. P. Pennisi, "Boron-doped nanocrystalline diamond electrodes for neural interfaces: in vivo biocompatibility evaluation", Frontiers in Neuroscience **10**, 87 (2016).

[35]L. S. Pan and D. R. Kania, eds., *Diamond: electronic properties and applications* (Springer, 1995).

[36]J. E. Field, "The mechanical and strength properties of diamond", Reports on Progress in Physics **75**, 126505 (2012).

[37]F. P. Bundy, H. T. Hall, H. M. Strong, and R. H. Wentorf, "Man-made diamonds", Nature **176**, 51–55 (1955).

[38]S. Ohmagari, "Single-crystal diamond growth by hot-filament CVD: recent advances for doping, growth rate, and defect controls", Functional Diamond **3**, 2259941 (2023).

[39]M. Kamo, Y. Sato, S. Matsumoto, and N. Setaka, "Diamond synthesis from gas phase in microwave plasma", Journal of Crystal Growth **62**, 642–644 (1983).

[40]J. C. Arnault and H. A. Girard, "Diamond nucleation and seeding techniques: two complementary strategies for the growth of ultra-thin diamond films", RSC Nanoscience and Nanotechnology, 221–252 (2014).

[41]M. Schreck, F. Hörmann, H. Roll, J. K. N. Lindner, and B. Stritzker, "Diamond nucleation on iridium buffer layers and subsequent textured growth: a route for the realization of single-crystal diamond films", Applied Physics Letters **78**, 192–194 (2001).

[42]M. Schreck, "Growth of single crystal diamond wafers for future device applications", 583–631 (2021).

[43]M. Schreck, J. Asmussen, S. Shikata, J. C. Arnault, and N. Fujimori, "Large-area high-quality single crystal diamond", MRS Bulletin **39**, 504–510 (2014).

[44]S. J. Cobb, Z. J. Ayres, and J. V. Macpherson, "Boron doped diamond: a designer electrode material for the twenty-first century", Annual Review of Analytical Chemistry **11**, 463–484 (2018).

[45] R. S. Balmer, J. R. Brandon, S. L. Clewes, H. K. Dhillon, J. M. Dodson, I. Friel, P. N. Inglis, T. D. Madgwick, M. L. Markham, T. P. Mollart, et al., “Chemical vapour deposition synthetic diamond: materials, technology and applications”, Journal of Physics: Condensed Matter **21**, 364221 (2009).

[46] E. A. Ekimov, V. A. Sidorov, E. D. Bauer, N. N. Mel’nik, N. J. Curro, J. D. Thompson, and S. M. Stishov, “Superconductivity in diamond”, Nature **428**, 542–545 (2004).

[47] J. V. Macpherson, “A practical guide to using boron doped diamond in electrochemical research”, Phys. Chem. Chem. Phys. **17**, 2935–2949 (2015).

[48] V. Mortet, I. Gregora, A. Taylor, N. Lambert, P. Ashcheulov, Z. Gedeonova, and P. Hubik, “New perspectives for heavily boron-doped diamond Raman spectrum analysis”, Carbon **168**, 319–327 (2020).

[49] V. Mortet, Z. Živcová, A. Taylor, M. Davydová, O. Frank, P. Hubík, J. Lorincik, and M. Aleshin, “Determination of atomic boron concentration in heavily boron-doped diamond by Raman spectroscopy”, Diamond and Related Materials **93**, 54–58 (2019).

[50] J. Cifre, J. Puigdollers, M. C. Polo, and J. Esteve, “Trimethylboron doping of cvd diamond thin films”, Diamond and Related Materials **3**, 628–631 (1994).

[51] A. F. Azevedo, M. R. Baldan, and N. G. Ferreira, “Doping level influence on chemical surface of diamond electrodes”, J. Phys. Chem. Solid. **74**, 599–604 (2013).

[52] Y. Gong, W. Jia, B. Zhou, K. Zheng, D. Ma, Z. Li, J. Gao, Y. Ma, H. Hei, S. Yu, Y. Xue, and Y. Wu, “Effect of boron doping levels on the microstructure and characteristics of high-quality boron-doped diamond electrodes prepared by mpcvd”, Diamond and Related Materials **139**, 110377 (2023).

[53] N. G. Ferreira, E. Abramof, E. J. Corat, and V. J. Trava-Airoldi, “Residual stresses and crystalline quality of heavily boron-doped diamond films analysed by micro-raman spectroscopy and x-ray diffraction”, Carbon **41**, 1301–1308 (2003).

[54] S. Baluchová, A. Taylor, V. Mortet, S. Sedláková, L. Klimša, J. Kopeček, O. Hák, and K. Schwarzová-Pecková, “Porous boron doped diamond for dopamine sensing: effect of boron doping level on morphology and electrochemical performance”, Electrochim. Acta **327**, 135025 (2019).

[55] T. Nishinaga, ed., *Handbook of crystal growth* (Elsevier, 2015).

[56] K. Schwarzová-Pecková, J. Vosáhlová, J. Barek, I. Šloufová, E. Pavlova, V. Petrák, and J. Zavázalová, “Influence of boron content on the morphological, spectral, and electroanalytical characteristics of anodically oxidized boron-doped diamond electrodes”, Electrochim. Acta **243**, 170–182 (2017).

[57] Z. Liu, H. Li, M. Li, C. Li, L. Qian, L. Su, and B. Yang, “Preparation of polycrystalline bdd/ta electrodes for electrochemical oxidation of organic matter”, Electrochimica Acta **290**, 109–117 (2018).

[58] S. Garcia-Segura, E. Vieira dos Santos, and C. A. Martínez-Huitle, “Role of sp^3/sp^2 ratio on the electrocatalytic properties of boron-doped diamond electrodes: a mini review”, Electrochem. Commun. **59**, 52–55 (2015).

[59] T. Watanabe, Y. Honda, K. Kanda, and Y. Einaga, “Tailored design of boron-doped diamond electrodes for various electrochemical applications with boron-doping level and sp^2-bonded carbon impurities”, Phys. Status Solidi **211**, 2709–2717 (2014).

[60] L. A. Hutton, J. G. Iacobini, E. Bitziou, R. B. Channon, M. E. Newton, and J. V. Macpherson, “Examination of the factors affecting the electrochemical performance of oxygen-terminated polycrystalline boron-doped diamond electrodes”, Analytical Chemistry **85**, 7230–7240 (2013).

[61] Y. Chen, X. Gao, G. Liu, R. Zhu, W. Yang, Z. Li, F. Liu, K. Zhou, Z. Yu, Q. Wei, and L. Ma, “Correlation of the role of boron concentration on the microstructure and electrochemical properties of diamond electrodes”, Functional Diamond **1**, 197–204 (2022).

[62] P. Yu, J. Zhang, T. Zheng, and T. Wang, “Influence of boron doped level on the electrochemical behavior of boron doped diamond electrodes and uric acid detection”, Colloids and Surfaces A: Physicochemical and Engineering Aspects **494**, 241–247 (2016).

[63] J. T. Matsushima, W. M. Silva, A. F. Azevedo, M. R. Baldan, and N. G. Ferreira, “The influence of boron content on electroanalytical detection of nitrate using BDD electrodes”, Applied Surface Science **256**, 757–762 (2009).

[64] S. A. Hara, T. R. Moen, K. Bennet, K. H. Lee, and J. R. Tomshine, “Removal and evaluation of non-diamond carbon on boron-doped diamond electrodes”, in 2017 IEEE International Symposium on Medical Measurements and Applications, MeMeA 2017 - Proceedings (2017), pp. 117–122.

[65] S. J. Cobb, F. H. J. Laidlaw, G. West, G. Wood, M. E. Newton, R. Beanland, and J. V. Macpherson, “Assessment of acid and thermal oxidation treatments for removing sp2 bonded carbon from the surface of boron doped diamond”, Carbon **167**, 1–10 (2020).

[66] Y. Einaga, “Boron-doped diamond electrodes: fundamentals for electrochemical applications”, Accounts of Chemical Research **55**, 3605–3615 (2022).

[67] Y. V. Pleskov, Y. E. Evstefeeva, M. D. Krotova, V. P. Varnin, and I. G. Teremetskaya, “Synthetic semiconductor diamond electrodes: electrochemical behaviour of homoepitaxial boron-doped films orientated as (111), (110), and (100) faces”, J. Electroanal. Chem. **595**, 168–174 (2006).

[68] K. Ushizawa, K. Watanabe, T. Ando, I. Sakaguchi, M. Nishitani-Gamo, Y. Sato, and H. Kanda, “Boron concentration dependence of Raman spectra on 100 and 111 facets of B-doped CVD diamond”, Diam. Relat. Mater. **7**, 1719–1722 (1998).

[69] T. Kondo, Y. Einaga, B. V. Sarada, T. N. Rao, D. A. Tryk, and A. Fujishima, “Homoepitaxial single-crystal boron-doped diamond electrodes for electroanalysis”, J. Electrochem. Soc. **149**, E179–E184 (2002).

[70] T. Ando, K. Asai, J. Macpherson, Y. Einaga, T. Fukuma, and Y. Takahashi, “Nanoscale reactivity mapping of a single-crystal boron-doped diamond particle”, Anal. Chem. **93**, 5831–5838 (2021).

[71] K. B. Holt, A. J. Bard, Y. Show, and G. M. Swain, “Scanning electrochemical microscopy and conductive probe atomic force microscopy studies of hydrogen-terminated boron-doped diamond electrodes with different doping levels”, Journal of Physical Chemistry B **108**, 15117–15127 (2004).

[72] N. R. Wilson, S. L. Clewes, M. E. Newton, P. R. Unwin, and J. V. Macpherson, “Impact of grain-dependent boron uptake on the electrochemical and electrical properties of polycrystalline boron doped diamond electrodes”, J. Phys. Chem. B **110**, 5639–5646 (2006).

[73] M. Grujicic and S. G. Lai, “Grain-scale modeling of cvd of polycrystalline diamond films”, Journal of Materials Synthesis and Processing **8**, 73–85 (2000).

[74] T. Liu, D. Raabe, and W.-M. Mao, “A review of crystallographic textures in chemical vapor-deposited diamond films”, Frontiers of Materials Science in China **4**, 1–16 (2010).

[75] W. Mao, H. Zhu, L. Chen, H. Feng, and F. Lü, “Grain orientation dependence on distance to surface of cvd diamond film”, Materials Science and Technology **21**, 1383–1386 (2005).

[76] A. Dettlaff, M. Sobaszek, T. Klimczuk, and R. Bogdanowicz, “Enhanced electrochemical kinetics of highly-oriented (111)-textured boron-doped diamond electrodes induced by deuterium plasma chemistry”, Carbon **174**, 594–604 (2021).

[77] E. Vanhove, J. D. Sanoit, J. C. Arnault, S. Saada, C. Mer, P. Mailley, P. Bergonzo, and M. Nesladek, “Stability of h-terminated bdd electrodes: an insight into the influence of the surface preparation”, Physica Status Solidi A **204**, 2931–2939 (2007).

[78] T. Ando, M. Ishii, M. Kamo, and Y. Sato, “Thermal hydrogenation of diamond surfaces studied by diffuse reflectance fourier-transform infrared, temperature-programmed desorption and laser raman spectroscopy”, Journal of the Chemical Society, Faraday Transactions **89**, 1783–1789 (1993).

[79] R. Hoffmann, A. Kriele, H. Obloh, J. Hees, M. Wolfer, W. Smirnov, N. Yang, and C. E. Nebel, “Electrochemical hydrogen termination of boron-doped diamond”, Applied Physics Letters **97**, `10.1063/1.3476346` (2010).

[80] S. Kasahara, K. Natsui, T. Watanabe, Y. Yokota, Y. Kim, S. Iizuka, Y. Tateyama, and Y. Einaga, “Surface hydrogenation of boron-doped diamond electrodes by cathodic reduction”, Analytical Chemistry **89**, 11341–11347 (2017).

[81] S. Ferro, M. D. Colle, and A. D. Battisti, “Chemical surface characterization of electrochemically and thermally oxidized boron-doped diamond film electrodes”, Carbon **43**, 1191–1203 (2005).

[82] I. Yagi, H. Notsu, T. Kondo, D. A. Tryk, and A. Fujishima, “Electrochemical selectivity for redox systems at oxygen-terminated diamond electrodes”, J. Electroanal. Chem. **473**, 173–178 (1999).

[83] A. Denisenko, C. Pietzka, A. Romanyuk, H. El-Hajj, and E. Kohn, “The electronic surface barrier of boron-doped diamond by anodic oxidation”, Journal of Applied Physics **103**, 014904 (2008).

[84] F. B. Liu, J. D. Wang, B. Liu, X. M. Li, and D. R. Chen, “Effect of electronic structures on electrochemical behaviors of surface-terminated boron-doped diamond film electrodes”, Diam. Relat. Mater. **16**, 454–460 (2007).

[85] Z. Živcová, V. Petrák, O. Frank, and L. Kavan, “Electrochemical impedance spectroscopy of polycrystalline boron doped diamond layers with hydrogen and oxygen terminated surface”, Diam. Relat. Mater. **55**, 70–76 (2015).

[86] X. Lu, Y. Peng, H. Qiu, X. Liu, and L. Ge, “Anti-fouling membranes by manipulating surface wettability and their anti-fouling mechanism”, Desalination **413**, 127–135 (2017).

[87] Y. Tateyama, Z. Futera, Y. Ootani, S. Iizuka, and L. T. Anh, “Computational aspects of surface and interface of BDD electrode”, Diamond Electrodes: Fundamentals and Applications, 57–71 (2022).

[88] N. J. Yang, S. Y. Yu, J. V. Macpherson, Y. Einaga, H. Y. Zhao, G. H. Zhao, G. M. Swain, and X. Jiang, “Conductive diamond: synthesis, properties, and electrochemical applications”, Chemical Society Reviews **48**, 157–204 (2019).

[89] T. A. Ivandini, T. N. Rao, A. Fujishima, and Y. Einaga, “Electrochemical oxidation of oxalic acid at highly boron-doped diamond electrodes”, Analytical Chemistry **78**, 3467–3471 (2006).

[90] D. A. Tryk, H. Tachibana, H. Inoue, and A. Fujishima, “Boron-doped diamond electrodes: the role of surface termination in the oxidation of dopamine and ascorbic acid”, Diamond and Related Materials **16**, 881–887 (2007).

2

2

UNRAVELLING MICROSTRUCTURE-ELECTROACTIVITY RELATIONSHIPS IN FREE-STANDING POLYCRYSTALLINE BORON-DOPED DIAMOND: A MAPPING STUDY

In this work, four mapping techniques were applied to study the relationship between local electroactivity and surface characteristics of free-standing polycrystalline BDD. Scanning electron microscopy, electron back-scatter diffraction, Raman mapping, and scanning electrochemical microscopy were used to probe morphology, grain orientation, composition, and local electrochemical activity, respectively. Both nucleation and growth surfaces of BDD were investigated, providing insights into the highly heterogeneous nature of polycrystalline BDD. Boron dopants were found to be non-uniformly distributed, with the highest electrochemical activity recorded on the heavily doped (111) crystal orientation. In contrast, the (100)-oriented facet showed non-conductive behavior. Increased boron and sp^2 *carbon contents in boundary regions were observed, but these did not enhance electrochemical activity, implying that boron atoms in intergrain areas are inactive. These findings highlight the importance of considering crystal orientation and boron doping when designing and evaluating polycrystalline BDD for micro- and nanoscale applications.*

The contents of this chapter have been published in:

- Z. Liu, S. Baluchová, Z. Li, Y. Gonzalez-Garcia, C. E. Hall, and J. G. Buijnsters, “Unravelling microstructure-electroactivity relationships in free-standing polycrystalline boron-doped diamond: A mapping study,” *Acta Materialia* **266**, 119671 (2024). DOI:10.1016/j.actamat.2024.119671

2.1. INTRODUCTION

Since its introduction some four decades ago, polycrystalline BDD has found extensive application in various fields including electroanalysis, development of novel electrochemical (bio)sensors [1, 2] and electrochemiluminescence systems [3], water treatment processes and mineralization of pollutants [4–6], electrosynthesis [7], electrocatalysis [8], and electrochemical energy storage [9]. Such wide spread of the BDD-based electrodes can be ascribed to their sp^3-hybridized carbon nature resulting in exceptional properties such as superior chemical and mechanical stability, wide potential window, low capacitive and background currents, reduced susceptibility towards corrosion and (bio)fouling, and biocompatibility [1, 10–12]. Moreover, BDD electrodes possess an adjustable electrical conductivity [13, 14] and surface termination [15, 16], representing two key material properties with major influence on electrode performance and applicability. Other parameters affecting the BDD characteristics are the fraction of grain boundaries with associated content of non-diamond (sp^2) carbon [13, 17, 18], surface finish [19–21] and crystallographic orientation [15, 22, 23].

In principle, all factors listed above are governed by conditions defined during the chemical vapor deposition (CVD) process that is typically used for the BDD synthesis. Boron doping is accomplished from the gas phase by adding a boron-containing compound, such as diborane, trimethyl borane, trimethyl borate or boron trioxide, into the CVD reaction chamber with the source gases, i.e., carbon-containing gas (typically methane) and hydrogen [10]. Depending on the boron amount, either semi-conductive or metal-like conductive BDD electrodes can be prepared; a threshold for metallic type conductivity was determined to be $1-3\times10^{20}\,\text{atoms cm}^{-3}$ [24, 25]. Consequently, the boron doping level influences the heterogeneous electron transfer kinetics at the electrode-electrolyte interface, which is then manifested in the recorded responses (potential positioning and signal intensity) of studied redox-active molecules [13, 14].

Notably, boron integrates within the diamond lattice in a non-uniform way. It has been shown that the amount of boron incorporated varies between the differently oriented diamond crystal faces and increases in the following order: (100) < (110) < (111) [26]. Using the same boron-to-carbon ratio in the gas phase during the CVD process results in approximately one order of magnitude higher boron concentration in the (111) surface, compared to the (100) orientation [27, 28]. Consequently, boron atoms are heterogeneously distributed across the polycrystalline BDD surfaces, which generates domains of various doping levels and thus conductivity (possibly spanning from insulating to semiconducting to metal-like) and electrochemical activity [29, 30]. Recently, Ando et al. investigated the electrochemical properties of (100) and (111) crystal facets of isolated single BDD microparticles using the nanoscale reactivity mapping technique [31]. The results revealed significantly faster HET kinetics, and thus higher activity, on the (111) facet, compared to the (100) facet and such difference was ascribed to the higher boron dopant density present on the (111)-oriented crystal [31].

Further, the CVD process is of non-equilibrium nature, which results in the formation of various structural defects, such as twinned crystal domains with corresponding twin boundaries [32, 33]. Via the formation of twin boundaries, the diamond lattice effectively manages accumulated stress created by the incorporation of impurities (boron dopant) during the CVD growth [33]. Notably, (111) orientations are prone to easily formed twinning and defects [34], which is in contrast to (100) faces typically containing fewer structural defect sites [35]. Several researchers have claimed preferential accumulation of boron dopant at such defective sites and at twin, or in general, grain boundaries [33, 36, 37]. Others, though, have reported no enhanced boron doping at the inter-grain regions [38], which also serve as sites for the enrichment of sp^2 carbon impurities possessing electrocatalytic activity [39]. These factors undoubtedly contribute to significant non-uniformity across the polycrystalline BDD electrode surfaces. Evidently, surface heterogeneities considerably influence the concentration and mobility of charge carriers at the BDD electrode surface and their effect is often manifested by differences in electrochemical activity.

Several attempts have been made to address BDD heterogeneity using a range of techniques including electrogenerated chemiluminescence [40], cathodoluminescence [30], photoluminescence and micro-secondary-ion mass spectrometry [41], scanning transmission electron microscopy and electron energy-loss spectroscopy [33], Raman spectroscopy and imaging [36, 38], scanning electrochemical microscopy (SECM) [29, 30, 39], conductive atomic force microscopy (AFM) [30, 39], and impedance imaging [37, 42]. However, contradictory results and conclusions have been reported in the literature: Bard et al. [39] investigated differently doped polycrystalline BDD electrodes ([B] ranging from 2×10^{17} to 2×10^{20} atoms cm^{-3}) using conductive AFM and SECM and claimed that their surfaces are predominantly insulating with non-uniformly distributed conducting areas creating "hot spots" of electrochemical activity. Also, grain boundaries were identified as high conductivity regions, where boron atoms are possibly accumulated [39], which agrees with the findings acquired by local impedance imaging presented in [37]. In contrast, works by Macpherson & Unwin et al. [29, 30, 43] indicated that the entire surface of highly doped (~5×10^{20} atoms cm^{-3}) polycrystalline BDD electrodes is electrochemically active; however, local heterogeneities in electroactivity (more vs. less conducting regions) were identified and correlated with the facet-dependent variations in boron doping level. This was concluded from SECM-based surface analyses which also did not reveal any enhanced conductivity nor increased electroactivity at grain boundaries [29, 30, 43].

Apparently, unravelling direct and conclusive links between particular variations in BDD surface characteristics and localized electrochemical activity continues to be a challenge. Therefore, this work aims to gain deeper understanding on the heterogeneity of self-supported, polycrystalline BDD electrodes. They possess, in general, so-called nucleation and growth surfaces, which can be either in their "as-deposited" or polished state. In this work, the polished nucleation and growth surfaces as well as the cross-section area of the free-standing, polycrystalline BDD material were subjected to thorough investigation using several techniques. Scanning electron microscopy (SEM) was used to analyze the morphological characteristics and electron back-scatter diffraction (EBSD) was applied to create orientation and boundary maps of the individual electrode regions, which allowed for the confirmation and quantification of primary and secondary twins. Raman spectroscopic imaging was employed to map the distribution of sp^3 (diamond) and sp^2 (non-diamond) carbon as well as boron dopants throughout the different BDD surfaces. Moreover, the polished growth surface of the BDD electrode, the most commonly employed in electrochemical studies, was subjected to SECM mapping experiments to probe its conductive and electrochemically active areas using an outer-sphere ferrocenemethanol ($FcMeOH^{+/0}$) redox couple. The exclusive combination of EBSD, Raman and SECM mapping, performed on a single electrode, allowed to illuminate the interplay between local electrochemical activity and investigated surface characteristics, including crystal orientation, grain (twin) boundaries, boron doping, and carbon phase composition.

2.2. EXPERIMENTAL

2.2.1. PREPARATION OF FREE-STANDING BDD ELECTRODES

Two free-standing ~700 μm thick BDD electrodes with a boron content of ~3×10^{20} cm^{-3} and a resistivity of 0.50 mΩm were sourced from Diafilm EP Grade BDD (Element Six, UK) and acquired from Mintres B.V. (The Netherlands). Both BDD samples were synthesized by Element Six using a proprietary microwave plasma CVD process, the specific details of which are not publicly available. The growth and nucleation surfaces of the first BDD electrode (1.5×1.5 cm^2) were mechanically polished until a surface mean roughness of <10 nm was achieved. In the case of the second BDD electrode (1.0×0.5 cm^2), resulting from the fragmentation of a larger sample, only the cross-sectional area was chem-mechanically polished and analyzed, while its growth and nucleation surfaces were preserved in "as-deposited" state and were not exposed to any measurements.

Prior to use, both studied BDD samples were firstly ultrasonicated in acetone, isopropanol, and deionized water (5 min in each medium) and subsequently acid cleaned by boiling for 5 min in a mixture composed of concentrated HCl, H_2SO_4, and HNO_3 in a ratio of 2:2:3, which resulted in clean and stable oxygen-terminated surfaces. Finally, the electrodes were extensively rinsed with deionized water and dried with compressed air.

To ensure performing various measurements (SEM, EBSD, Raman and SECM mapping) on the same location within the polished growth BDD surface and to enable their correlation, a reference cross with lines of 30 μm in width was laser cut on the sample.

2.2.2. MICROSCOPIC AND SPECTROSCOPIC MEASUREMENTS

The surface morphology, crystal orientation, and grain boundary information of the processed BDD electrodes were acquired using an SEM operating at a 15 kV accelerating voltage (JEOL JSM6500F, Japan) and equipped with an EBSD detector (Helios G4 PFIBUXe, Thermo Fisher Scientific, USA). EBSD orientation maps were created using the OIM Analysis software (EDAX, USA), which evaluated the recorded Kikuchi diffraction patterns. The grain boundaries were identified as regions where the angular misorientation between two contiguous crystalline grains exceeds 2°. In addition, primary and secondary twinning boundaries were classified based on the distinct crystallographic parameters. Specifically, primary twinning boundaries exhibit a misorientation defined by a <111> rotational axis coupled with an angular deviation ranging from 58° to 62°. In contrast, secondary twinning boundaries are identified by a <110> rotational axis with an associated misorientation angle spanning from 36.9° to 40.9° [44]. X-ray diffraction (XRD) analysis was performed using a Bruker D8 Advance diffractometer with a Bragg-

Brentano geometry and a Lynxeye XE position sensitive detector using CuKα radiation. Surface roughness was determined from AFM measurements with a JPK Nanowizard 4 (Bruker, USA) in tapping mode with silicon tips over a scanned area of 100×100 μm^2. Raman spectra were acquired with a Horiba LabRAM HR (Japan) device equipped with a solid state Cobolt Fandango^{TM} laser operating at 515 nm wavelength (Hübner Photonics, Germany). Raman imaging was performed using a 100× objective with a spot size of ~ 300 nm and a step size of 1 μm; during the surface mapping, the full spectra in the range from 200 to 1800 cm^{-1} for each point were recorded and stored. As-recorded Raman spectra were used without any background correction to compose Raman intensity maps corresponding to the dominant spectral features. Particularly, the width and the intensity of the peak located at ~ 1330 cm^{-1} and the band intensity at ~ 1550 cm^{-1} were evaluated and employed for Raman imaging.

2.2.3. ELECTROCHEMICAL MEASUREMENTS

Cyclic voltammograms of FcMeOH$^{+/0}$ redox probe were recorded on the polished growth surface of the polycrystalline BDD working electrode, placed in a lab-made PTFE cell, using an Autolab PGSTAT 128N controlled by Nova 2.1 software (Metrohm, The Netherlands). A conventional three-electrode configuration was completed with a platinum counter electrode (5.7 cm long wire) and a silver-silver chloride reference electrode (both ALS Co Japan).

SECM measurements were performed using a Scanning Electrochemical Workstation Model 370 (Ametek Scientific Instruments, USA). A Pt microelectrode probe, sealed in a glass tube, with a 10 μm diameter tip was employed as a working electrode; the ratio of the radius of the insulating glass sheath to the radius of the Pt disk (RG) was 5. The cell was completed with a reference Ag/AgCl (3 M KCl) electrode and a Pt wire serving as the counter electrode. The SECM was operated under feedback mode using 1 mM FcMeOH$^{+/0}$ (in 0.1 M KNO$_3$) as a redox mediator. The redox potential of +0.5 V, selected based on cyclic voltammograms recorded with the same set-up, was applied at the Pt electrode to oxidize this mediator, while the BDD electrode was kept under open circuit potential (OCP). The SECM map of the polished growth BDD surface was recorded in an area of 100 × 80 μm^2 with a scanning rate of 2 μm s^{-1} and a tip-substrate distance fixed to 2 μm. Besides, approach curves were recorded to probe the electrochemical nature of the individual spots (six in total) located at the polished growth BDD surface, i.e., to identify whether they are active or inactive. The Pt probe tip carefully approached to the substrate (BDD) in the feedback mode at a rate of 0.1 μm s^{-1}. Curves were displayed using normalised current (I) and distance (L). I corresponds to the ratio between the measured probe current (i_T) and the steady-state current ($i_{T\infty}$) recorded far from the substrate. L represents the ratio between substrate-to-probe tip distance (d) and the tip radius (r). All cyclic voltammetry (CV) and SECM measurements were conducted at room temperature (23 ± 1 °C).

2.2.4. CHEMICALS

Ferrocenemethanol (97%), potassium nitrate (≥99%), sulphuric acid (95 – 98%), hydrochloric acid (37%), nitric acid (70%), isopropanol, and acetone were purchased from

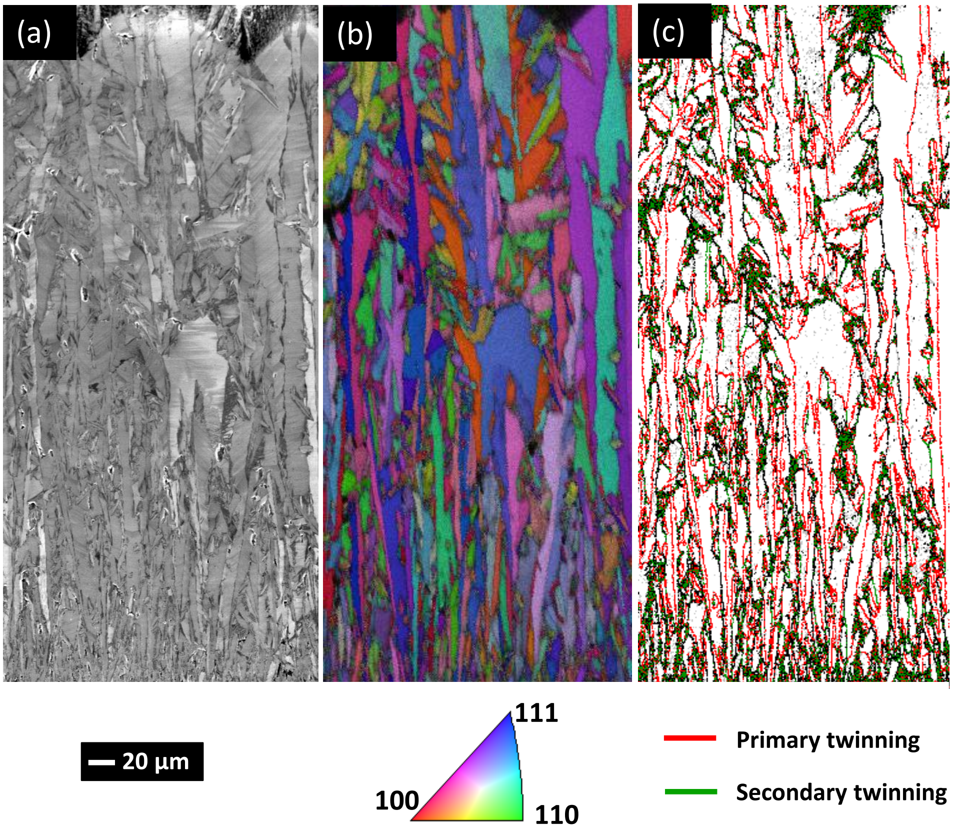

Figure 2.1: (a) SEM image, (b) EBSD map visualizing crystalline orientation, and (c) grain boundary map acquired from the cross-section of the free-standing, polycrystalline BDD electrode.

Merck and used as-received. Deionized water (resulting resistivity of >18.0 MΩ cm), purified with a LWTN Genie A system (Laboratorium Water Technologie Nederland), was used to prepare all aqueous solutions.

2.3. RESULTS AND DISCUSSION

2.3.1. SEM AND EBSD ANALYSIS

The morphological characteristics of the polycrystalline BDD samples were observed using SEM, whereas crystal orientation and grain boundary maps were imaged based on the EBSD measurements. The cross-section area of the BDD material was probed and is depicted in Fig. 2.1. The nucleation side consisting of smaller grains is visualized at the bottom of the images. As the images progress to the top, larger crystals can be clearly identified. The columnar structure typical for the CVD diamond growth was visualized by SEM (Fig. 2.1(a)), while EBSD mapping revealed a rich mixture of crystal orientations

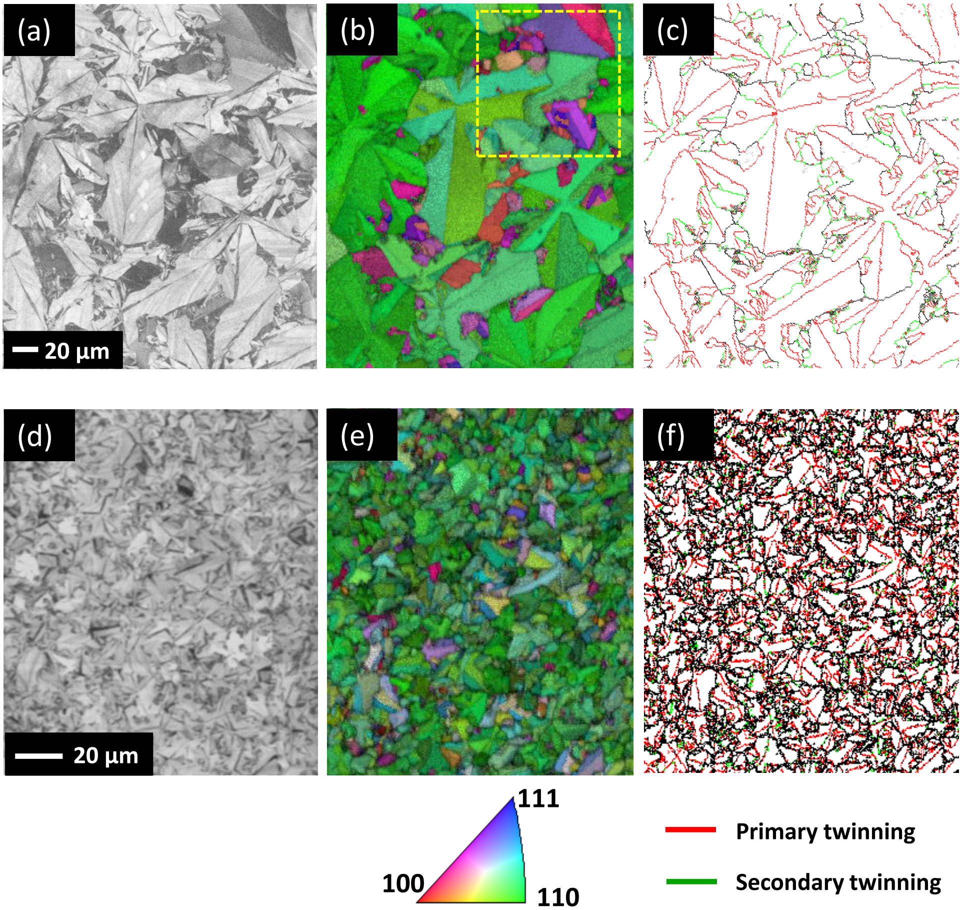

Figure 2.2: (a, d) SEM images, (b, e) EBSD maps visualizing crystalline orientation (with a colour map), and (c, f) grain boundary maps acquired from the polished (a-c) growth surface and (d-f) nucleation surface of the free-standing, polycrystalline BDD electrode.

(Fig. 2.1(b)). Grains either possessing or leaning toward (100), (110) and (111) orientations are clearly observed in Fig. 2.1(b) across the entire sample cross-section area. No preferential development of a specific orientation along the growth direction (i.e., from nucleation toward growth surface) can be distinguished. Further, the boundary map displayed in Fig. 2.1(c) shows a significant number of grain boundaries (marked as black lines) as well as primary and secondary twin boundaries (in red and green colour) whose quantity was estimated to be 19 % and 12 %, respectively. Such twinning operations are a typical feature of columnar crystal growth of the polycrystalline diamond.

The same coupled SEM/EBSD analysis was conducted on the polished nucleation and growth surfaces of the BDD material; the obtained micrographs and maps are vi-

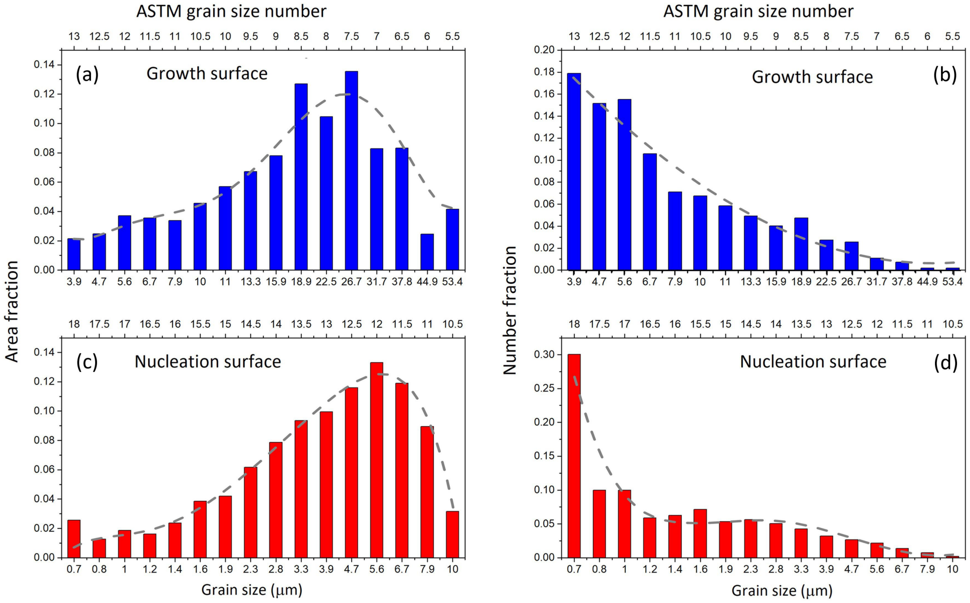

Figure 2.3: Grain size distribution histograms for the polished (a, b) growth and (c, d) nucleation surface expressed by (a, c) area fraction and (b, d) number fraction. Data are plotted as a function of grain size (μm) and ASTM grain size number, respectively [45]. Grey dashed lines represent the fitting curves.

sualized in Fig. 2.2. The SEM images clearly show that the growth surface consists of crystals of different dimensions including relatively large grains up to several tens of microns in diameter, while on average smaller grains down to ~ 1 μm are identified on the nucleation surface. This is further supported by the histograms provided in Fig. 2.3, which show the distribution of the diamond grain sizes within the individual surfaces. The growth side includes grains whose diameter widely ranges between 4 and 53 μm, whereas the grain size range is narrower on the nucleation surface, where the largest crystals do not exceed 10 μm in diameter. As can be further derived from the dashed fitting curves in Fig. 2.3(a, c), the most prevailing grain size on the growth and nucleation BDD surface (i.e., in terms of area fraction) is located at ~ 26 μm and ~ 6 μm, respectively.

The EBSD orientation maps (Fig. 2.2(b, e)) demonstrate that the majority of both growth and nucleation surfaces consist of (110) orientation with a small contribution from (100) and (111) to the overall surface textures. This is presumably related to the fact that <110> is the direction of the fastest growth [46]. Similarly, previous works also reported on the dominance of (110) orientation over (100) and (111) in polycrystalline (doped) diamond, in the form of both a thin film (thickness of ≤ 0.5 μm) [21] and a free-standing electrode (thickness of several hundred μm) [46, 47]. Besides, EBSD enabled to visualize the boundary maps for the polished growth and nucleation surfaces (Fig. 2.2(c, f)); the latter contains much more grain boundaries due to the smaller grain sizes, where sp^2-hybridized carbon typically resides [17, 48]. Primary and secondary twins between the crystallites on the nucleation surface represent a fraction of 29 % and 14 % of all grain boundaries, respectively. In contrast, a higher fraction of primary twin boundaries, i.e.,

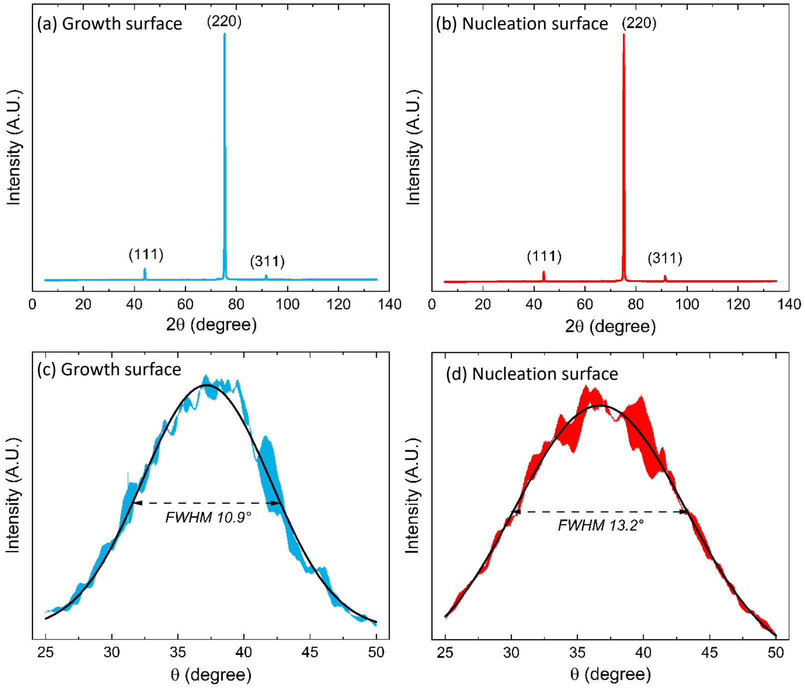

Figure 2.4: (a, b) XRD patterns and (c, d) XRD rocking curve scans of the (220), or (110), crystalline planes recorded on the (a, c) polished growth side and (b, d) nucleation side of the free-standing BDD electrode. The curves in (c, d) include Gaussian fitting (black lines) and values of full width at half maximum (FWHM).

44 %, was found on the polished growth side (Fig. 2.2(a)), however, the secondary twins occur with a similar incidence of 13 %. Noticeably, thicker and darker grain boundaries recognized in the SEM image of the growth surface were identified as primary twins in the boundary map (marked by red arrows in Fig. 2.2(c)), while thinner and lighter boundaries appeared as ‘regular’ grain boundaries (marked by black arrows in Fig. 2.2(c)).

Further, the recorded XRD patterns, shown in Fig. 2.4(a, b), display small peaks belonging to (111) and (311) planes, and importantly, a very sharp and intense signal for the (220), or (110) plane. This thus confirms the significant prevalence of the (110) orientation on both polished and nucleation BDD surfaces, which is well in line with the EBSD mapping analysis discussed above. Moreover, the XRD rocking curve scans were acquired for the (110) plane of both the growth and nucleation sides, see Fig. 2.4(c, d). The curves are very broad (with FWHM > 10°) which indicates that the BDD surfaces are not sharply (110) textured. Besides, the relatively large grains (see Fig. 2.3) contribute to intense reflections, which cause the rocking curves not to have the character of a smooth line, but involve wide, irregular ‘features’.

In the rest of the study, a smaller area of $100 \times 100\,\mu\mathrm{m}^2$ localized in the upper right corner of the SEM/EBSD images of the polished growth BDD surface was selected for further investigation (see yellow dashed square in Fig. 2.2(b)). A detail of the EBSD ori-

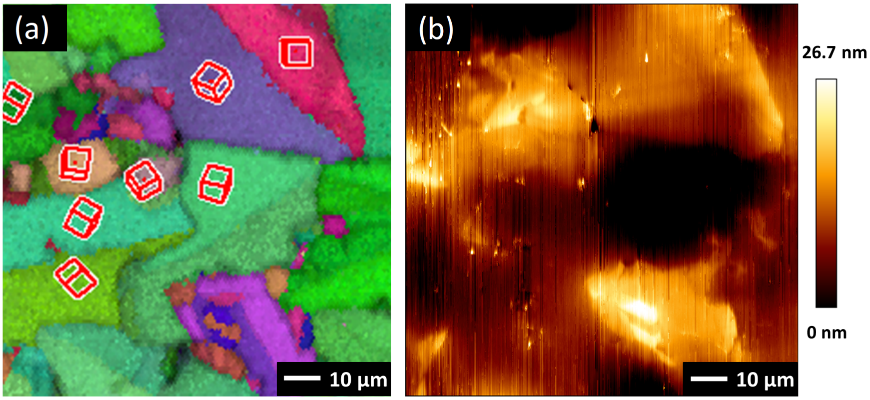

Figure 2.5: (a) Crystal orientation map obtained by EBSD including oriented unit cells ("cubes") for various selected spots and (b) atomic force micrograph of the same area on the polished growth surface of the free-standing, polycrystalline BDD electrode.

entation map for the chosen region, along with the oriented unit cells for several spots of interest, is provided in Fig. 2.5(a). In addition, Fig. 2.5(b) displays the corresponding topographic AFM image, where a notable difference in polishing 'efficiency' can be recognized as minor height variations of individual diamond grains. In particular, (110)-oriented crystals were smoothed down by polishing more effectively than the grains having (111) orientations, which protrude from the surface. Markedly, (111)-oriented crystals are harder to polish, even though they appear to be most heavily boron-doped (see below Section 2.3.2). Typically, though, higher impurity (boron) content leads to deteriorated wear resistance, as previously reported in [49]. Observed differences in wear resistance in the present study translated into local variations in the surface topography, however, the averaged surface roughness of the polished growth side of the polycrystalline BDD is very low at a level of ca 6 nm.

2.3.2. RAMAN ANALYSIS

Non-destructive Raman spectroscopy was used to assess the composition of the polished growth surface of the BDD electrode, which is most commonly subjected to electrochemical measurements. The same area previously examined by SEM/EBSD was analyzed by Raman mapping to find the correlation between on the one hand the morphology and crystal orientation and on the other hand the content of boron dopants and sp^2 carbon impurities. In particular, six different spots were identified in the EBSD orientation map, depicted in Fig. 2.6(a), and labelled with numbers 1–6 for easier description: 1, 2 – green, 3 – pink, and 4 – purple crystals leaning towards (110), (100), and (111) orientations, respectively; 5, 6 – twin boundaries.

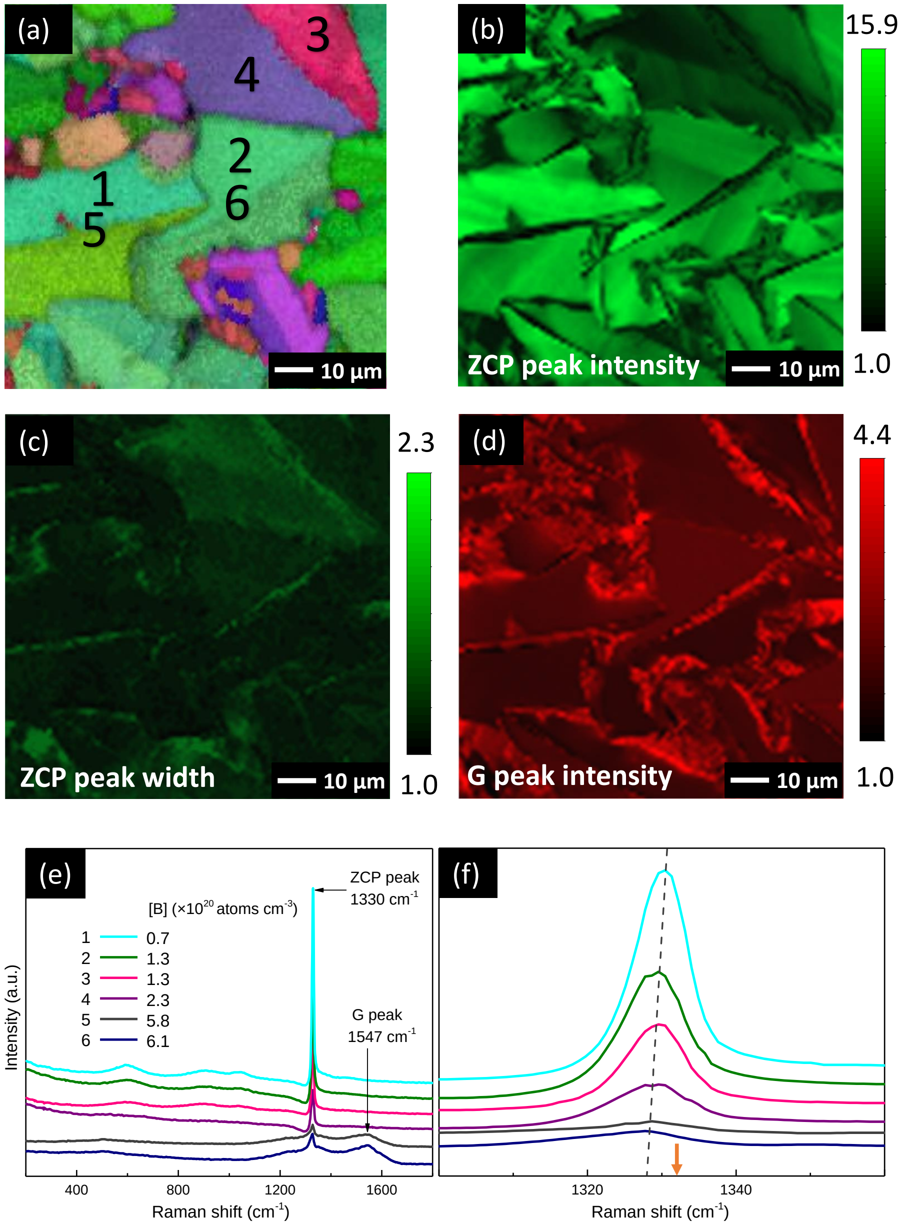

Figure 2.6: (a) EBSD orientation map and (b)-(d) corresponding Raman maps of the polished growth surface of the free-standing, polycrystalline BDD electrode based on: (b) ZCP peak intensity, (c) ZCP peak width, and (d) G peak intensity. (e) Raman spectra recorded at the six different spots indicated in (a). (f) Respective zoomed-in ZCP diamond peaks where the dashed line follows a trend of peak downshift with increasing boron concentration. The orange arrow points to the Raman shift value (i.e., 1332 cm^{-1}) of an undoped single-crystal diamond sample.

RAMAN MAPPING OF THE POLISHED GROWTH SURFACE

Fig. 2.6(b)–(d) presents a series of Raman spectral maps derived from (b) the diamond's zone-center phonon (ZCP) peak intensity, (c) the ZCP peak width, both indirectly related to the boron doping, and (d) the G peak intensity associated with the presence of non-diamond (sp^2) carbon. The position, width and intensity of the diamond's ZCP line (at ∼1330 cm^{-1} in Fig. 2.6(e)) are affected by the lattice structure, strain, and incorporated boron impurities. Particularly, with increasing boron content, the ZCP peak gradually decreased in intensity, broadened and shifted toward a lower wavenumber [38, 43, 50]. This is demonstrated in Fig. 2.6(f), showing in detail the ZCP peak extracted from the Raman spectra acquired from the six selected locations within the investigated BDD region.

The Raman map of the ZCP line intensity in Fig. 2.6(b) correlates very well with the SEM image (see top right corner in Fig. 2.2(a)) and EBSD orientation map (Fig. 2.6(a)), and allows to identify all individual crystals. Notably, the line intensity in the map varies by almost a factor of 16 between the darker and brighter areas. The former ones, represented predominantly by spot 4 (purple crystal with (111) orientation) and spots 5 and 6 (twin boundaries), signalize lesser diamond (sp^3) content and simultaneously increased amount of boron and/or non-diamond (sp^2) carbon. In contrast, the brightest regions in the ZCP line intensity Raman map are mostly associated with (110)-faceted diamond crystals (e.g., spots 1 and 2 in Fig. 2.6(a)).

Fig. 2.6(c) depicts the Raman map constructed from the ZCP peak width, which can be used to indirectly determine the uptake of boron dopants within the investigated region [50]. However, it must be emphasized that the ZCP peak recorded by Raman spectroscopy is generally affected by the quantity of all defects, including the ones unrelated to boron incorporation [51]. Particularly, two types of areas of brighter contrast signalizing wider ZCP peaks, and thus possibly higher boron doping, were identified and were found complementary to the darker regions in the previous map constructed from the ZCP peak intensity (Fig. 2.6(b)): (i) spot 4 in the EBSD map representing a (111)-oriented crystal, which agrees with previous works reporting higher boron incorporation efficiency for the (111) crystals, compared to the (110)- and (100)-oriented facets [26–28], and (ii) twin (grain) boundaries, including spots 5 and 6. This also supports previous studies claiming on enrichment of boron atoms at twin boundaries [33, 36] whose formation represents a highly effective coping mechanism for stress induced in the diamond lattice due to the impurity incorporation. Thus, our Raman mapping strongly indicates that boron atoms are non-uniformly distributed across the BDD electrode surface.

The third Raman map, shown in Fig. 2.6(d), was created based on the intensity of the G-band, a broad Raman signal centred at around 1547 cm^{-1}, whose origin is associated with the presence of sp^2 (non-diamond) carbon [52]. The highest intensity regions correspond to twin (grain) boundaries, where sp^2 carbon is, indeed, expected to reside [48]. Simultaneously, these areas are presumably enriched by incorporated boron atoms, as suggested by the Raman map shown in Fig. 2.6(c). Similar detection of predominant non-diamond carbon at sites showing increased boron concentration was made in [38].

RAMAN SPECTRA OF THE POLISHED GROWTH SURFACE

Individual Raman spectra recorded at the six different spots indicated in the EBSD map (see Fig. 2.6(a)) are displayed in Fig. 2.6(e). Naturally, the spectra differ depending on boron concentration ([B]) and presence or absence of sp^2 carbon phase. However, the common feature for all spectra is the diamond's ZCP line located in the range of 1327–1330 cm^{-1}, which is simultaneously the most pronounced signal. Magnification of this Raman peak is provided in Fig. 2.6(f) to clearly show its asymmetric and broadened line shape. As already mentioned, the ZCP line is downshifted from the expected position of a reference single-crystal undoped diamond (1332 cm^{-1}; indicated by the orange arrow in Fig. 2.6(f)). The differences in signal intensity and downshifts ranging from 2 to 5 cm^{-1} imply surface areas of various boron doping level. This is supported by the [B] values determined using the Raman analysis tool thoroughly described in [53, 54] and available at [55]. This fitting tool, developed for highly B-doped diamond (i.e., [B] > 5×10^{19} cm^{-3}), was used over the range from 1100 cm^{-1} to 1500 cm^{-1} as it is based on the analysis of two characteristic Raman peaks located at ~1200 cm^{-1} and ~1330 cm^{-1} attributed to the Fano-shaped maximum of phonon density of states and zone-centre phonon (ZCP) line of highly doped BDD, respectively. Importantly, both the position and the width of the ZCP (diamond) peak, which were proved to be proportional to the boron concentration [53], are considered in the fitting tool, among other parameters. Notably, for the selected spots in the investigated region of the polished growth surface, [B] spans over one order of magnitude from 7.0×10^{19} to 6.1×10^{20} atoms cm^{-3}; all values are listed in Fig. 2.6(e). This range accurately covers the average [B] value declared by the manufacturer (i.e., 3×10^{20} cm^{-3}).

For spots 1–3, also low-intensity peaks are present at ca 610, 925 and 1045 cm^{-1}, which are typical characteristics for BDD with boron doping levels in the range of 10^{18}–10^{20} cm^{-3} [38, 56], corresponding well with the boron estimation ([B]) above. Lastly, the G peak at 1547 cm^{-1} only arises in the Raman spectra acquired from twin boundaries, denoted as spots 5 and 6.

RAMAN MAPPING OF THE CROSS-SECTION AREA

The exact same cross-section area, previously visualized using SEM and EBSD techniques (see Fig. 2.1), was subjected to Raman imaging. Fig. 2.7 displays two Raman maps which were created based on the intensity of the ZCP peak and the G band associated with the presence of sp^3 and sp^2 carbon, respectively. The mapping was not performed in one run but divided into smaller sections to avoid problems associated with overall cross-section non-uniformity and laser focusing. Note that the very edge (~10 μm) of the lower nucleation side was affected by the sample preparation procedure, which appears as a 'grey strip' in the Raman images, and thus no conclusions can be made on this area.

The acquired Raman maps demonstrate distinctive columnar growth of a polycrystalline diamond microstructure, which is consistent with the observations based on the SEM and EBSD images presented above. Also, the Raman maps of the cross-section area are quite complementary. For example, bright areas of the highest ZCP peak intensity in Fig. 2.7(a) are simultaneously the least intense in Fig. 2.7(b), and vice versa. The ZCP peak intensity varies by a factor of ~24 across the cross-section area, which indicates

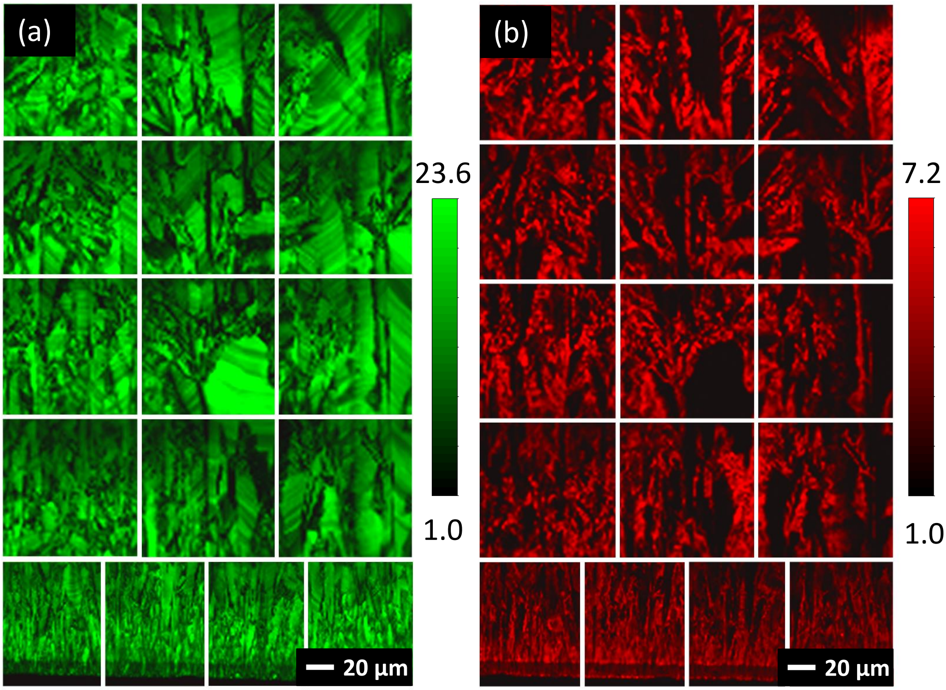

Figure 2.7: Raman maps of the cross-section area of the BDD electrode based on the intensity of the (a) ZCP peak (sp^3 carbon) and (b) G peak (sp^2 carbon).

heterogeneous character of the BDD material across the whole film thickness. Such variations and particularly a decrease in intensity can be ascribed to the incorporation of boron dopants and/or the presence of sp^2 carbon phase. This is consistent with the trends observed for the polished growth surface of the BDD electrode.

SCANNING ELECTROCHEMICAL MICROSCOPY (SECM) MEASUREMENTS

Next, the surface probe technique SECM, in its feedback mode, was employed to map the electrochemically active regions on the polished growth surface of the BDD electrode. The effect of topography on the obtained signals could be completely neglected as AFM measurements (see Fig. 2.5(b)) confirmed that the roughness of the investigated surface is at the nanometer scale. This allowed to conduct SECM mapping in constant-height mode, while using a Pt probe (10 μm tip diameter) in a solution of redox marker, 1 mM $FcMeOH^{+/0}$ (in 0.1 M KNO_3), with applied Pt tip potential of +0.5 V (vs. Ag/AgCl). The SECM map was recorded in the exact same area as the EBSD orientation and Raman maps to draw correlation between local electrochemical activity and surface texture and composition, respectively.

The $FcMeOH^{+/0}$ redox probe was selected based on its outer-sphere character of electron transfer, which is insensitive to surface characteristics, including termination and extent of oxidation. The CV curve of $FcMeOH^{+/0}$ recorded on the polished growth

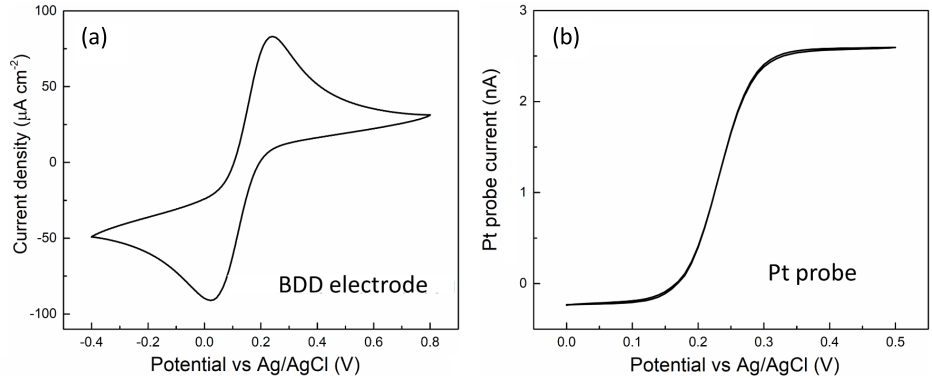

Figure 2.8: Cyclic voltammograms of 1 mM $FcMeOH^{+/0}$ in 0.1 M KNO_3 recorded on (a) the polished growth surface of the BDD electrode and (b) a Pt microprobe (10 μm in diameter) used in SECM measurements.

surface, shown in Fig. 2.8(a), displays a well-developed pair of redox peaks with a peak-to-peak separation value of 0.21 V. At the applied tip potential, oxidation of $FcMeOH^0$ to $FcMeOH^{1+}$ occurs at the Pt probe as verified, prior to the SECM measurements, by performing CV experiments; a representative CV is shown in Fig. 2.8(b). Also, information on the steady-state current, i_{ss} of 2.8 nA, was extracted from the CV. The scanned polycrystalline BDD substrate was kept under OCP conditions, thus no potential control was implemented.

The SECM map is shown in normalized current scale in Fig. 2.9(b) and displays non-uniform distribution of electrochemical activity across the investigated region with currents detected by the Pt probe (i_T) ranging from 2.7 nA to 5.5 nA. In general, a ratio of $i_T/i_{ss} < 1$ reflects suppressed feedback relative to bulk conditions; however, this criterion alone does not imply electrically insulating behavior and must be interpreted by comparison with the response above a truly insulating surface. In the recorded image, only one spot, denoted as “3” (around 15 μm in diameter), exhibited a strongly reduced feedback current, indicative of markedly hindered electron-transfer kinetics. This spot corresponds to a crystal with orientation leaning towards the (100) plane (see Fig. 2.9(a) and Fig. 2.2(b)). It was also the only spot for which approach curves displayed near-negative-feedback behavior, as shown in Fig. 2.9(c), despite having an estimated boron concentration of [B] $\sim 1 \times 10^{20}$ cm^{-3} (see Fig. 2.6(e)). This indicates that, although not truly insulating, this region exhibits significantly lower electrochemical activity compared to the surrounding grains. This implies that the effect of crystal orientation may have a more dominant effect on the electrochemical response than the boron concentration. A similar remark was made in the work of Ivandini et al., where equally doped (100) and (111)-faceted single crystal BDD electrodes ([B] $\sim 4 \times 10^{20}$ cm^{-3}) were compared and hindered electron transfer kinetics and peaks of lower intensity were recorded for redox probes on the (100) facet, compared to the (111) crystal [15].

Nevertheless, the majority of the studied surface area showed $i_T/i_{ss} > 1$, and thus manifested electrochemically active and conductive behaviour, which was also con-

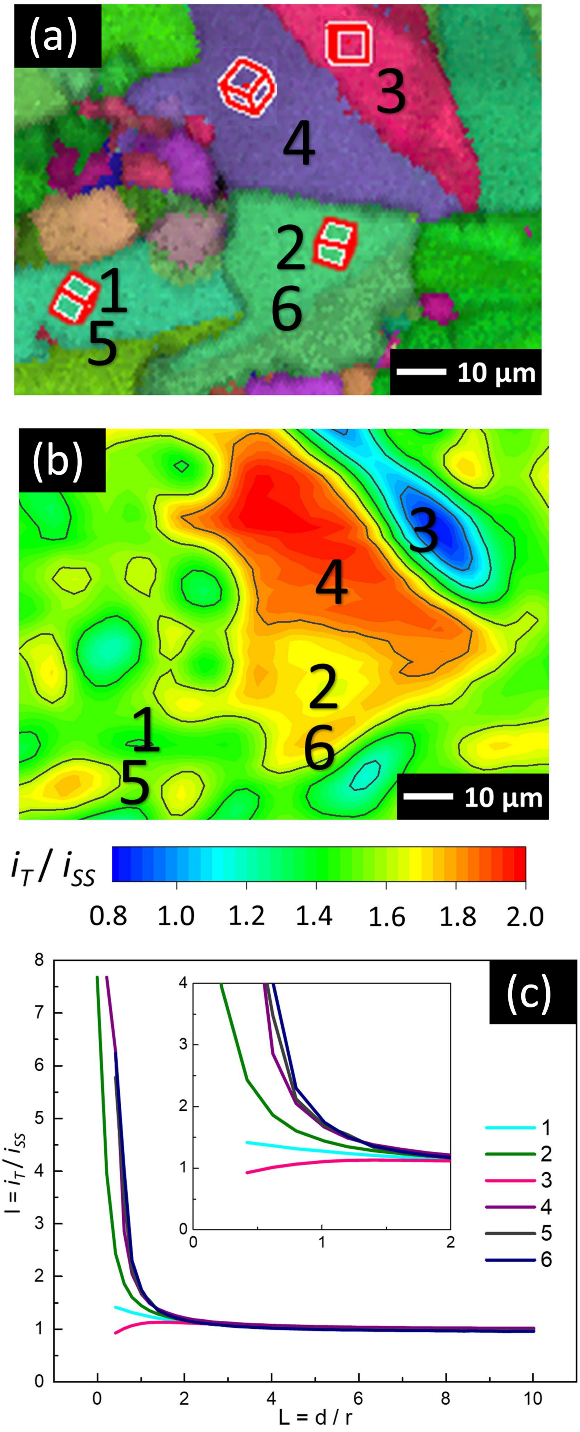

Figure 2.9: (a) EBSD orientation map and (b) SECM map ($100 \times 80\,\mu m^2$) of the polished growth surface (same area) obtained with a 10-μm diameter Pt tip in 1 mM $FcMeOH^{+/0}$ (in 0.1 M KNO_3), with a tip potential of +0.5 V (vs. Ag/AgCl) and the BDD substrate kept under OCP. (c) Experimental probe approach curves recorded at the six different spots, as indicated by the numbers in (a) and (b).

firmed by probe approach curves performed at the remaining five spots demonstrating positive feedback. Markedly, ‘less pronounced’ positive feedback was distinguished at spot 1, which corresponds to the (110)-oriented crystal having, according to Raman analysis, the lowest doping ([B] of 7×10^{19} cm^{-3}) among the investigated sites. A clear trend of gradual development of much more distinct positive feedback responses with increasing boron contents (see corresponding values in Fig. 2.6(e)) can be identified in Fig. 2.9(c), the only exception being spot 3, addressed above. However, when [B] exceeds 2×10^{20} cm^{-3}, i.e., metallic threshold [24, 25], which is the case of spots 4, 5, and 6, the recorded probe approach curves become very comparable. This is presumably caused by the limited mass transfer rate of the redox marker to the Pt microprobe tip. As further evident from Fig. 2.9, the highest electrochemical activity was recorded at spot 4, i.e., the large crystal with (111) orientation and the highest boron concentration among the various grains (excluding the grain boundary regions). Local variations in electrochemical activity between different BDD crystal facets were evidenced by SECM-based techniques also in [29, 38, 43] and were correlated directly with differences in the local boron doping levels. It was postulated that the higher boron concentration yields increased density of states and electron transfer kinetics for outer-sphere redox probes [29].

Remarkably, twinning boundaries, exemplified by spots 5 and 6, showed no considerable increase in electrochemical activity even though the inter-grain regions are undoubtedly enriched by boron and sp^2 carbon. Apparently, such enrichment extracted from a series of Raman maps (see Fig. 2.6) and [B] estimation does not translate into enhanced electrochemical activity. This may be associated with the fact that Raman spectroscopy is sensitive to the overall amount of defect(s), i.e., also defects unrelated to boron incorporation into the diamond lattice can potentially affect the position, width and intensity of the ZCP diamond peak. Both electrically active and non-active boron atoms and other types of defects can contribute to the final ZCP lines displayed in Raman spectra [51]. Our observations are consistent with several previous works employing SECM-based techniques to probe the electrochemical activity of the BDD surfaces, in which no evidence confirming enhanced activity at grain boundaries was found [29, 30, 38, 43].

2.3.3. MICROSTRUCTURE-ELECTROACTIVITY RELATIONSHIPS

Polycrystalline BDD is characterized by a columnar grain structure and, consequently, a highly non-uniform microstructure and composition is developed as a function of its thickness, which is schematically displayed in Fig. 2.10. The distinctive columnar structure was visualized by SEM images as well as by EBSD and Raman maps. In addition, for the cross-section area, EBSD revealed a mixture of crystal orientations and significant number of grain and twin boundaries, while Raman mapping demonstrated variations in intensities of ZCP (diamond) and G (sp^2 carbon) peaks. All three characterization techniques thus confirm heterogeneous character of the polycrystalline BDD material across the whole film thickness.

Such heterogeneity naturally also translated into the characteristics of the polished growth BDD surface, which was thoroughly investigated. The grains of various shapes and sizes (up to tens of μm in diameter) possessed predominantly (110) orientation. However, a portion of (100)- and (111)-oriented crystal facets was also identified. Dif-

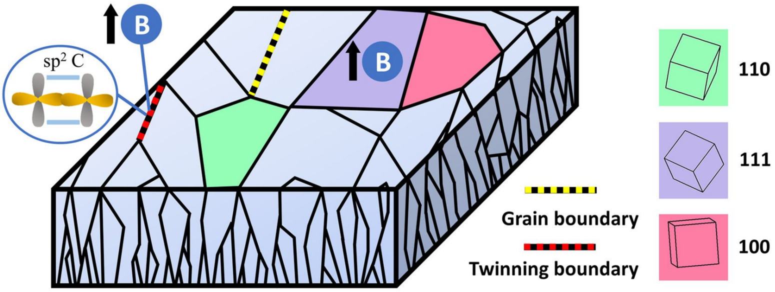

Figure 2.10: Schematic representation of the investigated features on the free-standing, polycrystalline BDD electrode.

ferent crystal orientations affected the boron uptake by the individual grains, while the highest incorporation efficiency was confirmed for the (111) crystals. Moreover, Raman spectroscopy detected elevated amount of boron dopants in the boundary regions, where also sp^2 carbon phase was predominantly present (see Fig. 2.10). However, no evidence of enhanced electrochemical responses was found for inter-grain regions despite their enrichment in boron and sp^2 carbon impurities; they are presumably residing in their electrically 'non-active forms'. In contrast, the most highly boron-doped (111) facet demonstrated the most pronounced electrochemical activity. Nevertheless, the intensity of the electrochemical responses cannot be ascribed only to localized boron doping levels. In particular, (100)-oriented grains, despite having an average [B] of $\sim 1 \times 10^{20}$ cm^{-3}, exhibited markedly reduced electrochemical activity, consistent with strongly hindered electron-transfer kinetics. This strongly suggests that crystal orientation is a leading factor controlling the electrochemical responses.

The crystal orientation of the individual BDD grains has been quite an overlooked parameter in the literature, while much more effort has been devoted into the investigation of other (however, still important) factors such as boron doping, sp^2 carbon content, and surface termination. Only recently, the significant effect of crystal orientation on the electrochemical behaviour of BDD electrodes has gained more attention. In several previous works, differences between crystal orientations were ascribed to different boron incorporation efficiency and resulting doping levels [27, 30, 43]. However, the more recent study comparing similarly doped (100)- and (111)-oriented BDD electrodes proved the superiority of the (111) facet over (100), which was associated with the different degrees of band bending and various thickness of space charge layer [15]. Further investigations at the atomic scale using low-temperature scanning tunnelling microscopy (STM) revealed that the dependence of the electrochemical activity of BDD electrodes on the crystal orientation originates from the boron-related deformation of the diamond lattice structure [54]. Specifically, graphitized domains related to boron incorporation were exclusively confirmed only in (111) facets, which could possibly explain their enhanced electrochemical activity, when compared to (100)-oriented crystals [57]. Besides, (113), (115) and (118)-oriented BDD electrodes of comparable [B] manifested different electrochemical responses, which was ascribed to the effect of crystal orientation and particularly to '(100)/(111) step' density [22].

All in all, boron atoms were found to be non-uniformly distributed over the polycrystalline BDD surface, but their presence was not always directly linked with greater electrochemical activity. Notably, next to boron concentration, crystallographic orientation has been identified as one of the dominating factors that largely govern the local electrochemical activity of the polycrystalline BDD electrodes.

This is expected to be true not only for thick, free-standing BDD electrodes but also for BDD thin films, composed of grains with various crystal orientations. However, one needs to be particularly careful to draw other parallel conclusions from the present study for thin films, often with submicron- or even nano-crystalline structures. This is because the scale of anisotropy and the resulting (doped) diamond's properties are primarily determined by the grain size, which in turn directs the amount of grain and twin boundaries. Markedly, as the diamond grains become smaller, the density of grain boundaries increases, and the non-diamond (sp^2) content becomes more prevalent [58, 59]. Besides, a significant decline in doping efficiency was demonstrated for nanocrystalline BDD thin films, compared to the microcrystalline ones, which was ascribed to the fact that boron atoms incorporate in a significant manner in positions (such as grain boundaries) that do not contribute to the conductivity in the same way as boron dopants incorporated in the grains [59]. Therefore, all these factors and the interplay between them must be carefully considered in order to unravel the micro/nanostructure-electroactivity relationships within thin-film BDD.

2.4. CONCLUSION

Highly doped, free-standing polycrystalline BDD is a complex electrode material with distinct columnar structure and uneven distribution of boron dopants across the whole cross-section, which naturally manifest also in the characteristics and behaviour of the BDD growth surface. The individual grains showed considerably different electrochemical responses as a consequence of their various crystal orientations whose significant impact is not only related to varying boron uptake efficiency but also to the inherent structure of each individual facet. In our work, the highest doped (111)-oriented crystal demonstrated the highest electrochemical activity, as probed by SECM results. However, the averagely boron-doped (100) facet exhibited markedly reduced electrochemical activity. This therefore implies that the local electrochemical activity of the BDD surface is strongly grain dependent and the most significant factors governing the obtained electrochemical responses are the (previously often neglected) crystallographic orientation in addition to the boron doping level.

Besides, EBSD enabled to visualize the boundary regions at the polished growth surface, where increased content of boron atoms and sp^2 carbon was recognized by Raman mapping. However, such enrichment in impurities did not translate into enhanced electrochemical activity probed by SECM, which implies that boron atoms at the inter-grain spots are predominantly of electrically inactive nature.

Finally, it is essential to consider all relevant material characteristics (i.e., grain size distribution, presence of sp^2 carbon, boron content, surface finish and surface termination, and grain orientation) when working with, or designing, polycrystalline BDD electrodes, but also thin-film BDD and single-crystal BDD. This is particularly important for electrochemical applications where micro- to nano-meter scale phenomena are to be monitored or exploited, such as in neural interfacing or *in-vivo* analysis.

BIBLIOGRAPHY

[1] S. Baluchová, A. Daňhel, H. Dejmková, V. Ostatná, M. Fojta, and K. Schwarzová-Pecková, "Recent progress in the applications of boron doped diamond electrodes in electroanalysis of organic compounds and biomolecules – a review", Analytica Chimica Acta **1077**, 30–66 (2019).

[2] M. Yence, A. Cetinkaya, G. Ozcelikay, S. I. Kaya, and S. A. Ozkan, "Boron-doped diamond electrodes: recent developments and advances in view of electrochemical drug sensors", Crit. Rev. Anal. Chem. **52**, 1122–1138 (2022).

[3] K. Sakanoue, A. Fiorani, C. I. Santo, Irkham, G. Valenti, F. Paolucci, and Y. Einaga, "Boron-doped diamond electrode outperforms the state-of-the-art electrochemiluminescence from microbeads immunoassay", ACS Sens. **7**, 1145–1155 (2022).

[4] Y. He, H. Lin, Z. Guo, W. Zhang, H. Li, and W. Huang, "Recent developments and advances in boron-doped diamond electrodes for electrochemical oxidation of organic pollutants", Sep. Purif. Technol. **212**, 802–821 (2019).

[5] O. M. Cornejo, M. F. Murrieta, L. F. Castañeda, and J. L. Nava, "Characterization of the reaction environment in flow reactors fitted with BDD electrodes for use in electrochemical advanced oxidation processes: a critical review", Electrochim. Acta **331**, 135373 (2020).

[6] D. S. Babu, J. M. C. Mol, and J. G. Buijnsters, "Experimental insights into anodic oxidation of hexafluoropropylene oxide dimer acid (GenX) on boron-doped diamond anodes", Chemosphere **288**, 132417 (2022).

[7] S. Lips and S. R. Waldvogel, "Use of boron-doped diamond electrodes in electro-organic synthesis", ChemElectroChem **6**, 1649–1660 (2019).

[8] C. Guo, J. Zheng, H. Deng, P. Shi, and G. Zhao, "Photoelectrocatalytic interface of boron-doped diamond: modification, functionalization and environmental applications", Carbon **175**, 454–466 (2021).

[9] S. Yu, N. Yang, S. Liu, and X. Jiang, "Diamond supercapacitors: progress and perspectives", Curr. Opin. Solid State Mater. Sci. **25**, 100922 (2021).

[10] N. J. Yang, S. Y. Yu, J. V. Macpherson, Y. Einaga, H. Y. Zhao, G. H. Zhao, G. M. Swain, and X. Jiang, "Conductive diamond: synthesis, properties, and electrochemical applications", Chemical Society Reviews **48**, 157–204 (2019).

[11] S. Yu, S. Liu, X. Jiang, and N. Yang, "Recent advances on electrochemistry of diamond related materials", Carbon **200**, 517–542 (2022).

[12] Z. Deng, R. Zhu, L. Ma, K. Zhou, Z. Yu, and Q. Wei, "Diamond for antifouling applications: a review", Carbon **196**, 923–939 (2022).

[13] S. Baluchová, A. Taylor, V. Mortet, S. Sedláková, L. Klimša, J. Kopeček, O. Hák, and K. Schwarzová-Pecková, "Porous boron doped diamond for dopamine sensing: effect of boron doping level on morphology and electrochemical performance", Electrochim. Acta **327**, 135025 (2019).

[14] K. Schwarzová-Pecková, J. Vosáhlová, J. Barek, I. Šloufová, E. Pavlova, V. Petrák, and J. Zavázalová, "Influence of boron content on the morphological, spectral, and electroanalytical characteristics of anodically oxidized boron-doped diamond electrodes", Electrochimica Acta **243**, 170–182 (2017).

[15] T. Ivandini, T. Watanabe, T. Matsui, Y. Ootani, S. Iizuka, R. Toyoshima, H. Kodama, H. Kondoh, Y. Tateyama, and Y. Einaga, "Influence of surface orientation on electrochemical properties of boron-doped diamond", J. Phys. Chem. C **123**, 5336–5344 (2019).

[16] S. Baluchová, A. Mamaloukou, R. H. J. M. Koldenhof, and J. G. Buijnsters, "Modification-free boron-doped diamond as a sensing material for direct and reliable detection of the antiretroviral drug nevirapine", Electrochim. Acta **450**, 142238 (2023).

[17] Z. Liu, A. F. Sartori, and J. G. Buijnsters, "Role of sp^2 carbon in non-enzymatic electrochemical sensing of glucose using boron-doped diamond electrodes", Electrochem. Commun. **130**, 107096 (2021).

[18] J. Anaya, S. Rossi, M. Alomari, E. Kohn, L. Tóth, B. Pécz, K. D. Hobart, T. J. Anderson, T. I. Feygelson, B. B. Pate, and M. Kuball, "Control of the in-plane thermal conductivity of ultra-thin nanocrystalline diamond films through the grain and grain boundary properties", Acta Mater. **103**, 141–152 (2016).

[19] Z. Liu, A. F. Sartori, and J. G. Buijnsters, "Role of sp^2 carbon in non-enzymatic electrochemical sensing of glucose using boron-doped diamond electrodes", Electrochem. Commun. **130**, 107096 (2021).

[20] J. V. Macpherson, "A practical guide to using boron doped diamond in electrochemical research", Physical Chemistry Chemical Physics **17**, 2935–2949 (2015).

[21] M. Zelenský, J. Fischer, S. Baluchová, L. Klimša, J. Kopeček, M. Vondráček, L. Fekete, J. Eidenschink, F. M. Matysik, S. Mandal, O. A. Williams, M. Hromadová, V. Mortet, K. S. Pecková, and A. Taylor, "Chem-mechanical polishing influenced morphology, spectral and electrochemical characteristics of boron doped diamond", Carbon **203**, 363–376 (2023).

[22] A. Taylor, S. Baluchová, L. Fekete, L. Klimša, J. Kopeček, D. Šimek, M. Vondráček, L. Míka, J. Fischer, K. Schwarzová-Pecková, and V. Mortet, "Growth and comparison of high-quality MW PECVD grown B-doped diamond layers on {118}, {115} and {113} single crystal diamond substrates", Diam. Relat. Mater. **123**, 108815 (2022).

[23] Z. Liu, S. Baluchová, A. F. Sartori, Z. Li, Y. Gonzalez-Garcia, M. Schreck, and J. G. Buijnsters, "Heavily boron-doped diamond grown on scalable heteroepitaxial quasi-substrates: a promising single crystal material for electrochemical sensing applications", Carbon **201**, 1229–1240 (2023).

[24] M. Bernard, A. Deneuville, and P. Muret, "Non-destructive determination of the boron concentration of heavily doped metallic diamond thin films from Raman spectroscopy", Diam. Relat. Mater. **13**, 282–286 (2004).

[25] J. P. Lagrange, A. Deneuville, and E. Gheeraert, "Activation energy in low compensated homoepitaxial boron-doped diamond films", Diam. Relat. Mater. **7**, 1390–1393 (1998).

[26] Y. V. Pleskov, Y. E. Evstefeeva, M. D. Krotova, V. P. Varnin, and I. G. Teremetskaya, "Synthetic semiconductor diamond electrodes: electrochemical behaviour of homoepitaxial boron-doped films orientated as (1 1 1), (1 1 0), and (1 0 0) faces", Journal of Electroanalytical Chemistry **595**, 168–174 (2006).

[27] K. Ushizawa, K. Watanabe, T. Ando, I. Sakaguchi, M. Nishitani-Gamo, Y. Sato, and H. Kanda, "Boron concentration dependence of raman spectra on 100 and 111 facets of b-doped cvd diamond", Diamond and Related Materials **7**, 1719–1722 (1998).

[28] T. Kondo, Y. Einaga, B. V. Sarada, T. N. Rao, D. A. Tryk, and A. Fujishima, "Homoepitaxial single-crystal boron-doped diamond electrodes for electroanalysis", Journal of The Electrochemical Society **149**, E179 (2002).

[29] H. V. Patten, S. C. S. Lai, J. V. Macpherson, and P. R. Unwin, "Active sites for outer-sphere, inner-sphere, and complex multistage electrochemical reactions at polycrystalline boron-doped diamond electrodes (pBDD) revealed with scanning electrochemical cell microscopy (SECCM)", Anal. Chem. **84**, 5427–5432 (2012).

[30] N. R. Wilson, S. L. Clewes, M. E. Newton, P. R. Unwin, and J. V. Macpherson, "Impact of grain-dependent boron uptake on the electrochemical and electrical properties of polycrystalline boron doped diamond electrodes", Journal of Physical Chemistry B **110**, 5639–5646 (2006).

[31] T. Ando, K. Asai, J. Macpherson, Y. Einaga, T. Fukuma, and Y. Takahashi, "Nanoscale reactivity mapping of a single-crystal boron-doped diamond particle", Analytical Chemistry **93**, 5831–5838 (2021).

[32] J. E. Butler and I. Oleynik, "A mechanism for crystal twinning in the growth of diamond by chemical vapour deposition", Philos. Trans. Royal Soc. A **366**, 295–310 (2008).

[33] Y. G. Lu, S. Turner, J. Verbeeck, S. D. Janssens, P. Wagner, K. Haenen, and G. V. Tendeloo, "Direct visualization of boron dopant distribution and coordination in individual chemical vapor deposition nanocrystalline b-doped diamond grains", Appl. Phys. Lett. **101**, 041907 (2012).

[34] A. Boussadi, A. Tallaire, O. Brinza, M. A. Pinault-Thaury, and J. Achard, "Thick heavily boron doped CVD diamond films homoepitaxially grown on (111)-oriented substrates", Diam. Relat. Mater. **79**, 108–111 (2017).

[35] C. Wild, R. Kohl, N. Herres, W. Müller-Sebert, and P. Koidl, "Oriented CVD diamond films: twin formation, structure and morphology", Diam. Relat. Mater. **3**, 373–381 (1994).

[36] K. E. Bennet, K. H. Lee, J. N. Kruchowski, S. Y. Chang, M. P. Marsh, A. A. V. Orsow, A. Paez, and F. S. Manciu, "Development of conductive boron-doped diamond electrode: a microscopic, spectroscopic, and voltammetric study", Materials **6**, 5726–5741 (2013).

[37] A. Zieliński, R. Bogdanowicz, J. Ryl, L. Burczyk, and K. Darowicki, "Local impedance imaging of boron-doped polycrystalline diamond thin films", Appl. Phys. Lett. **105**, 131908 (2014).

[38] S. Szunerits, M. Mermoux, A. Crisci, B. Marcus, P. Bouvier, D. Delabouglise, J. P. Petit, S. Janel, R. Boukherroub, and L. Tay, “Raman imaging and kelvin probe microscopy for the examination of the heterogeneity of doping in polycrystalline boron-doped diamond electrodes”, J. Phys. Chem. B **110**, 23888–23897 (2006).

[39] K. B. Holt, A. J. Bard, Y. Show, and G. M. Swain, “Scanning electrochemical microscopy and conductive probe atomic force microscopy studies of hydrogen-terminated boron-doped diamond electrodes with different doping levels”, Journal of Physical Chemistry B **108**, 15117–15127 (2004).

[40] K. Honda, T. Noda, M. Yoshimura, K. Nakagawa, and A. Fujishima, “Microstructural heterogeneity for electrochemical activity in polycrystalline diamond thin films observed by electrogenerated chemiluminescence imaging”, J. Phys. Chem. B **108**, 16117–16127 (2004).

[41] J. W. Steeds, A. Gilmore, S. Charles, P. Heard, B. Howarth, and J. E. Butler, “Use of novel methods for the investigation of the boron distribution in CVD diamond”, Acta Mater. **47**, 4025–4030 (1999).

[42] A. Zielinski, M. Cieslik, M. Sobaszek, R. Bogdanowicz, K. Darowicki, and J. Ryl, “Multi-frequency nanoscale impedance microscopy (M-NIM): a novel approach towards detection of selective and subtle modifications on the surface of polycrystalline boron-doped diamond electrodes”, Ultramicroscopy **199**, 34–45 (2019).

[43] H. V. Patten, K. E. Meadows, L. A. Hutton, J. G. Iacobini, D. Battistel, K. McKelvey, A. W. Colburn, M. E. Newton, J. V. Macpherson, and P. R. Unwin, “Electrochemical mapping reveals direct correlation between heterogeneous electron-transfer kinetics and local density of states in diamond electrodes”, Angew. Chem., Int. Ed. **51**, 7002–7006 (2012).

[44] T. Liu, D. Raabe, W. Mao, and S. Zaefferer, “Microtexture and grain boundaries in free-standing CVD diamond films: growth and twinning mechanisms”, Adv. Funct. Mater. **19**, 3880–3891 (2009).

[45] ASTM E112-13, “Standard test methods for determining average grain size”, (2004).

[46] C. Wild, N. Herres, and P. Koidl, “Texture formation in polycrystalline diamond films”, J. Appl. Phys. **68**, 973–978 (1990).

[47] D. Q. Liu, C. H. Chen, D. Perry, G. West, S. J. Cobb, J. V. Macpherson, and P. R. Unwin, “Facet-resolved electrochemistry of polycrystalline boron-doped diamond electrodes: microscopic factors determining the solvent window in aqueous potassium chloride solutions”, ChemElectroChem **5**, 3028–3035 (2018).

[48] M. Mohr, L. Daccache, S. Horvat, K. Brühne, T. Jacob, and H. J. Fecht, “Influence of grain boundaries on elasticity and thermal conductivity of nanocrystalline diamond films”, Acta Mater. **122**, 92–98 (2017).

[49] J. G. Buijnsters, M. Tsigkourakos, T. Hantschel, F. O. V. Gomes, T. Nuytten, P. Favia, H. Bender, K. Arstila, J. P. Celis, and W. Vandervorst, “Effect of boron doping on the wear behavior of the growth and nucleation surfaces of micro- and nanocrystalline diamond films”, ACS Appl. Mater. Interfaces **8**, 26381–26391 (2016).

[50] K. Srimongkon, S. Ohmagari, Y. Kato, V. Amornkitbamrung, and S.-i. Shikata, "Boron inhomogeneity of HPHT-grown single-crystal diamond substrates: Confocal micro-Raman mapping investigations", Diam. Relat. Mater. **63**, 21–25 (2016).

[51] A. Taylor, P. Ashcheulov, P. Hubík, Z. Weiss, L. Klimša, J. Kopeček, J. Hrabovsky, M. Veis, J. Lorinčík, I. Elantyev, and V. Mortet, "Comparative determination of atomic boron and carrier concentration in highly boron doped nano-crystalline diamond", Diam. Relat. Mater. **135**, 109837 (2023).

[52] A. Merlen, J. G. Buijnsters, and C. Pardanaud, "A guide to and review of the use of multiwavelength Raman spectroscopy for characterizing defective aromatic carbon solids: from graphene to amorphous carbons", Coatings **7**, 153 (2017).

[53] V. Mortet, Z. V. Živcová, A. Taylor, M. Davydová, O. Frank, P. Hubík, J. Lorincik, and M. Aleshin, "Determination of atomic boron concentration in heavily boron-doped diamond by raman spectroscopy", Diamond and Related Materials **93**, 54–58 (2019).

[54] V. Mortet, I. Gregora, A. Taylor, N. Lambert, P. Ashcheulov, Z. Gedeonova, and P. Hubik, "New perspectives for heavily boron-doped diamond raman spectrum analysis", Carbon **168**, 319–327 (2020).

[55] Determination of boron concentration in diamond from Raman spectroscopy, Online Raman analysis tool available at https://ramantool.pythonanywhere.com/ (accessed 21-02-2025).

[56] A. Crisci, M. Mermoux, and B. Saubat-Marcus, "Deep ultra-violet Raman imaging of CVD boron-doped and non-doped diamond films", Diam. Relat. Mater. **17**, 1207–1211 (2008).

[57] F. C. I. Catalan, L. T. Anh, J. Oh, E. Kazuma, N. Hayazawa, N. Ikemiya, N. Kamoshida, Y. Tateyama, Y. Einaga, and Y. Kim, "Localized graphitization on diamond surface as a manifestation of dopants", Adv. Mater. **33**, 2103250 (2021).

[58] O. A. Williams, A. Kriele, J. Hees, M. Wolfer, W. Müller-Sebert, and C. E. Nebel, "High young's modulus in ultra thin nanocrystalline diamond", Chemical Physics Letters **495**, 84–89 (2010).

[59] P. W. May, W. J. Ludlow, M. Hannaway, P. J. Heard, J. A. Smith, and K. N. Rosser, "Raman and conductivity studies of boron-doped microcrystalline diamond, facetted nanocrystalline diamond and cauliflower diamond films", Diam. Relat. Mater. **17**, 105–117 (2008).

3

3

ROLE OF SP^2 CARBON IN NON-ENZYMATIC ELECTROCHEMICAL SENSING OF GLUCOSE USING BORON-DOPED DIAMOND ELECTRODES

Boron-doped diamond (BDD) is of increasing interest for applications in electrochemical sensing. It is well known that the sp^2 carbon content in BDD influences its electrochemical properties as electrode material. In this work, evidence is provided that the surface sp^2 carbon content plays a crucial role in the electrochemical sensitivity of BDD towards glucose. Single-crystal BDD, freestanding polycrystalline BDD, and glassy carbon (sp^2 carbon reference material) were examined by voltammetry. Neither single-crystal BDD, which is free of sp^2 carbon, nor pure sp^2 glassy carbon could detect glucose in the range of 0.2–1.0 V. On the other hand, glucose oxidation was observed on polycrystalline BDD, and with increasing intensity with increase of sp^2 carbon content. Thus, an optimum amount of (B-doped) sp^2 carbon in the BDD electrode is needed for best sensing performance. Understanding this and being able to control the composition of BDD are not only important to glucose detection but to any electrochemical sensing application involving BDD.

The contents of this chapter have been published in:

- Z. Liu, A. F. Sartori, and J. G. Buijnsters, “Role of sp^2 carbon in non-enzymatic electrochemical sensing of glucose using boron-doped diamond electrodes,” *Electrochemistry Communications* **130**, 107096 (2021). DOI:10.1016/j.elecom.2021.107096

3.1. INTRODUCTION

Glucose detection and monitoring are extremely important procedures in healthcare and in the lives of millions of people who suffer from diabetes around the world. The World Health Organization has pointed out that the number of diabetic patients increased from 108 million in 1980 to 422 million in 2014 [1]. This number is predicted to grow to 578 million by 2030 [2]. Therefore, there is a continuous urgent need to develop affordable and easy-to-use medical instruments for diabetics to monitor their blood glucose levels. The main commercial products on the market at present are electrochemical enzyme-based glucose sensors. However, the enzyme is easily inactivated by environmental factors such as temperature, pH, and humidity [3], and its immobilization on the electrode is complicated and time-consuming. All these factors lead to high cost, short life, and insufficient stability [4] of the glucose sensors. Consequently, there is high demand for the development of non-enzymatic glucose sensors to overcome the inherent shortcomings of enzymatic detection [5–7]. Various metallic materials including pure metals, metal alloys, metal hydrates, metal sulfides, metal nitrides, and metal oxides have been studied for non-enzymatic glucose detection via oxidation [8–11]. However, the glucose oxidation products will easily adsorb on the surface of the metallic electrode and poison it.

BDD with its extreme electrochemical stability, low background current, wide potential window, resistance to fouling, and excellent biocompatibility [12], is recognised as an ideal material for electrochemical sensing of glucose. In 2005, Lee and Park reported for the first time that BDD electrodes can directly detect glucose without any modification with enzymes or metallic catalysts [13]. A number of following studies reported on improving the sensitivity of BDD towards glucose oxidation, such as by changing the boron doping level, surface morphology and surface termination, by creating 3D structures or by introducing metal-containing catalysts [14–16]. However, the influence of sp^2 carbon, which mainly exists in the grain boundaries of BDD, has been little explored. It is well known that changing the level of boron doping and/or changing the grain sizes of the polycrystalline thin-film BDD material, the sp^2 carbon content also changes. In general, the more sp^2 carbon content in the BDD electrode, the higher the conductivity of the electrode, resulting in higher voltammetric background current and narrower water potential window [17]. This was found to be unfavourable for glucose sensing [18]. On the other hand, BDD electrodes with higher sp^2 carbon content behave as "active anodes", showing higher catalytic activity towards analytes (e.g., dissolved oxygen, pH, and hypochlorite [19, 20]) that may be exploited for glucose sensing. Other contradictory observations on the non-enzymatic detection of glucose using bare BDD electrodes were reported as well. For example, Zhao et al. [21], Luo et al. [18], and Zou et al. [15] reported that as-grown BDD can directly detect glucose, while Watanabe et al. [22] and Dai et al. [23] reported no glucose oxidation signal on bare BDD electrodes. One of the main difficulties in making sense of these reports lies in the fact that the BDD electrodes used were fabricated under different processing conditions and had distinct grain sizes, boron-doping levels, surface morphologies, substrates, and were potentially exposed to different contaminants.

In this work, carefully prepared BDD model electrodes with defined microstructure and controlled amounts of sp^2 carbon were employed for non-enzymatic electrochemical detection of glucose, in order to properly identify the role of sp^2 carbon in the electrocatalytic activity of BDD towards this molecule. Four substrate-free BDD electrodes with distinct sp^2 carbon content were prepared by microwave plasma chemical vapor deposition (MWPCVD): including single-crystal BDD (boron content of 1.5×10^{20} atoms/cm^3) and freestanding polycrystalline BDD (boron content of 3×10^{20} atoms/cm^3) with nucleation side and both as-grown and polished growth surfaces. Linear sweep voltammetry (LSV) was used and the peak current densities were derived for glucose concentrations in the range from 0 to 15 mM.

3.2. EXPERIMENTAL

3.2.1. PREPARATION OF BDD ELECTRODES

Solid, freestanding BDD (FS-BDD) samples (15×15 mm^2 in size, 0.7 mm thickness, and boron content of 3×10^{20} atoms/cm^3) originating from Diafilm EP Grade BDD (Element Six, UK) were obtained from Mintres B.V. (The Netherlands). The respective growth (FS-BDD-gr) and nucleation (FS-BDD-nucl) surfaces were used as received. The polished surface (FS-BDD-pol) was obtained by chemical mechanical polishing of the growth surface until a surface mean roughness (S_a) of $\approx$ 1.3 nm was reached.

Solid, freestanding BDD (FS-BDD) samples (15×15 mm^2 in size, 0.7 mm thickness, and boron content of 3×10^{20} atoms/cm^3) originating from Diafilm EP Grade BDD (Element Six, UK) were obtained from Mintres B.V. (The Netherlands). The respective growth (FS-BDD-gr) and nucleation (FS-BDD-nucl) surfaces were used as received. The polished surface (FS-BDD-pol) was provided by the supplier and obtained by chemical mechanical polishing of the growth surface using a proprietary process until a surface mean roughness (S_a) of $\approx$ 1.3 nm was reached.

A single-crystal BDD electrode was grown by MWPCVD using two steps as described in Ref. [24], first the heteroepitaxial growth of undoped diamond on Ir/YSZ/Si(001), up to ~1 mm thickness, followed by growth of a ~5 μm thick B-doped layer after mechanical polishing and cleaning by reactive ion etching (RIE).

3.2.2. BRIEF DESCRIPTION OF FS-BDD AND RESPECTIVE ELECTRODE SURFACES

The grain structure of FS-BDD (Fig. 3.1) is highly non-uniform due to the growth process. During the nucleation phase ('nucleation surface'), small and randomly orientated grains form at the interface with the substrate (see Fig. 2.2(d,e)). Crystallites with facets favoured by the growth conditions then convert into large grains which are elongated in the direction of growth (see Fig. 2.1). The 'growth surface' of 0.7-mm thick FS-BDD is therefore characterized by large crystal facets and relatively high surface roughness. When processed ('polished surface'), a smooth but inhomogeneous surface of many orientations is obtained.

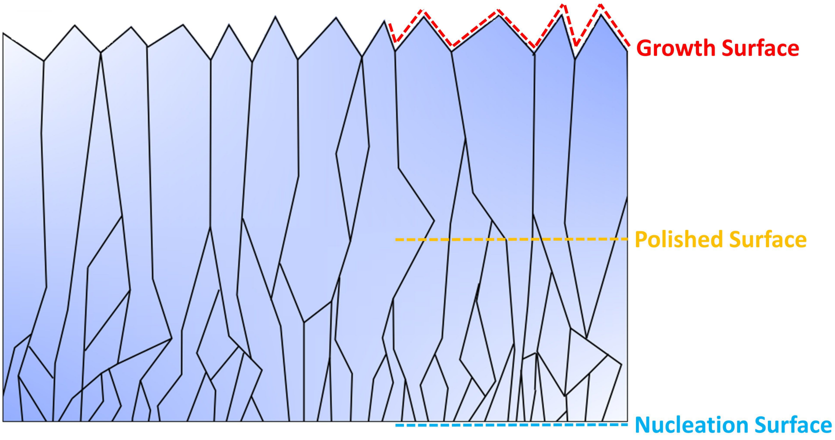

Figure 3.1: Schematic representation of the FS-BDD electrode. The respective growth (FS-BDD-gr) and nucleation (FS-BDD-nucl) surfaces were used as received. The polished surface (FS-BDD-pol) was obtained by chemical mechanical polishing of the growth surface until a surface mean roughness (S_a) of ≈ 1.3 nm was reached. (Figure adapted from [12].)

3.2.3. SURFACE CHARACTERIZATION

Scanning electron microscopy (SEM) characterization was done with a JEOL JSM-6010LA setup at 15 keV. Atomic force microscopy (AFM) measurements were done using a NaniteAFM system (Nanosurf AG) in tapping mode with silicon tips. The scanned area was $50 \times 50\ \mu\text{m}^2$. The FS-BDD-gr surface was exclusively analyzed using a VHX-6000 digital microscope (Keyence) with an area of $1000 \times 1000\ \mu\text{m}^2$. A Horiba LabRAM HR device equipped with an argon ion laser operating at 514 nm wavelength was used to record Raman spectra with a spectral resolution of about 0.3 cm^{-1}.

3.2.4. ELECTROCHEMICAL MEASUREMENTS

The electrochemical measurements were carried out at room temperature in a home-built cylindrical PTFE cell (100 mL) using a classical three-electrode configuration. Electrochemical measurements were performed using the various BDD samples as working electrodes (WE), a 5.7-cm long platinum wire as counter electrode (CE, from ALS Co.), and a RE-1B Ag/AgCl reference electrode (RE, from ALS Co.). The WE was mounted in the PTFE cell from underneath, exposed to the solution by a circular aperture of 7.7 mm, and sealed by a chemically resistant O-ring (Kalrez® Spectrum™ 6375, model AS568). Electric contact to the single-crystal BDD electrode surface was achieved with conductive silver paint, applied from the four corners towards the backside, and contacted by a copper disc wired to the potentiostat. For comparative electrode measurements, all electrodes were cleaned and stabilized in the same way. This involved sonicating the BDD electrodes in acetone, isopropanol, and DI water each for 5 min and running cyclic voltammetry experiments in 0.1 M NaOH, at 0.1 V/s, from 0 V to 1 V for 20 cycles. In

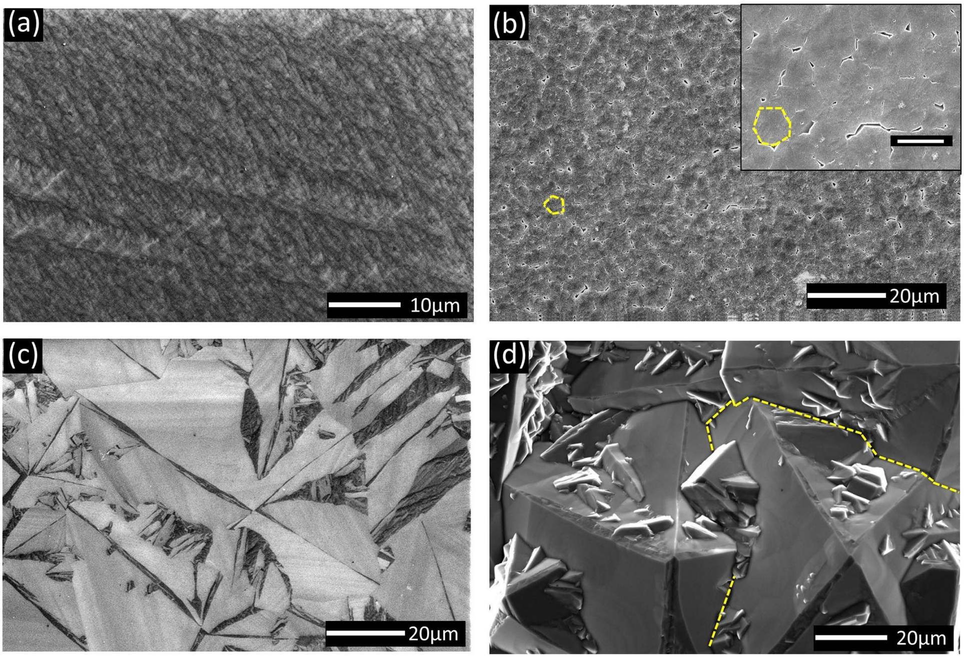

Figure 3.2: SEM images of the (a) single-crystal BDD, (b) FS-BDD-nucl, (c) FS-BDD-pol, and (d) FS-BDD-gr electrode surfaces. The inset in (b) shows a magnified image of the same surface (scale bar 5 μm). A few selected grains and grain boundaries are marked by yellow dashed lines.

addition, anodic oxidation for 1 hour at 5 V (vs. Ag/AgCl) was applied to the FS-BDD-pol and FS-BDD-nucl samples prior to further electrochemical analysis.

The electrochemical experiments were controlled with a μ-AUTOLAB III potentiostat (PGSTAT128N, Eco-Chemie, The Netherlands) running a Nova (Version 2.1.3) software. LSV was done in 0.1 M NaOH aqueous solution without and with varying glucose concentration (in the range from 0 to 15 mM) at a scan rate of 0.1 V/s. The current densities reported in this work were calculated using the O-ring defined geometric area corrected with roughness (AFM measured).

3.2.5. CHEMICALS

The water used to prepare electrolyte solutions and clean glassware was deionized and ultra-filtrated with a Millipore Milli-Q system (resistivity = 18.2 MΩ·cm and TOC < 5 ppb). Sodium hydroxide (≥97.0%), glucose (≥99.5%), and sulfuric acid were purchased from Merck. All chemicals were used without any further purification.

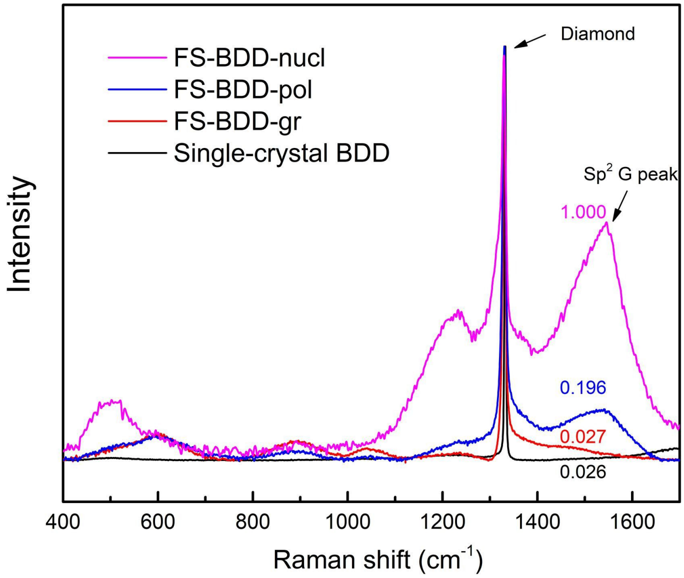

Figure 3.3: Raman spectra of the various BDD electrode surfaces. The as-measured curves were normalized relative to the diamond one-phonon line at 1332 cm^{-1}.

3.3. RESULTS AND DISCUSSION

3.3.1. SURFACE CHARACTERIZATION OF BDD ELECTRODES

SEM images of the different BDD electrode surfaces were recorded before any treatment, and they are shown in Fig. 3.2. A strong variation in grain size, surface roughness, and boundary line density among the different samples was observed. The single-crystal BDD surface (Fig. 3.2(a)) exhibits triangular features indicating small growth steps. It presents a smooth surface ($S_a \approx 5.1$ nm) and no misoriented crystals or twins can be observed. The three SEM images in Fig. 3.2(b, c, and d) reveal very different features of the various polycrystalline FS-BDD surfaces. The growth surface (Fig. 3.2(d)) shows relatively large crystal facets (up to ~60 μm in lateral size) and also some smaller grains on top of them, resulting in a relatively high roughness ($S_a \approx 15$ μm). The polished surface (Fig. 3.2(c)) presents a much lower roughness ($S_a \approx 1.3$ nm) and highlights the non-uniform composition of the grain structure of FS-BDD, which is due to the growth process. The nucleation surface (Fig. 3.2(b)) has the smallest average grain size (≈ 1 μm) and consequently more boundaries. Also, a large number of voids between grains are present (see inset of Fig. 3.2(b)).

Raman spectroscopic analysis (Fig. 3.3) was done to evaluate the crystalline quality, boron incorporation and presence of sp^2 carbon on the BDD electrode surfaces. The intense sharp peak at 1332 cm^{-1} observed for all samples is assigned to sp^3-hybridized carbon. This diamond zone-centre phonon line is narrowest in the case of the single-crystal BDD (FWHM $\approx$ 3.7 cm^{-1}). The line width broadens in the order FS-BDD-gr <

FS-BDD-pol < FS-BDD-nucl, which coincides with the decrease in average grain size of the electrode surfaces and thus shorter phonon lifetime. The sp^3 peak of FS-BDD-nucl is strongly distorted, forming a separated branch around 1200 cm^{-1} due to the Fano resonance effect [25]. The broad bands observed between 450 and 600 cm^{-1} are attributed to Raman scattering involving boron–carbon vibrations [26]. The G-band at around 1580 cm^{-1} is contributed from graphitic material (i.e., sp^2-C) present in the grain boundaries of the BDD material [27, 28], and normalized G-band values (maximum value to 1) are presented. The highest intensity is recorded on FS-BDD-nucl, because its boundary density is highest. FS-BDD-gr with the largest average grain size and lowest boundary density shows very minor G-band signal. An insignificant G-band signal was detected on single-crystal BDD, indicating negligible sp^2 carbon.

Furthermore, sp^2 carbon content was also electrochemically measured with a more surface-sensitive approach reported by Ayres et al. [29]. This method is based on the electroactive quinone groups present on sp^2 carbon sites. Due to the relatively large electrode area and different electrochemical setup, the noise of the CVs within pH 2 buffer solution was too high to detect the quinone oxidation peak at 0.420 V vs. SCE (0.465 V vs. Ag/AgCl). However, quinone-related oxidation peaks (e.g., hydrogen peroxide electrogenerated in the presence of quinone groups) were found in 0.1 M H_2SO_4 solution, as shown in Fig. 3.4. The shape of the observed peaks suggests that the electrochemical response is governed primarily by surface-associated redox sites rather than diffusion of species from the bulk electrolyte. Normalized peak values (maximum value set to 1) are shown. No oxidation peak was observed on single-crystal BDD. In the case of FS-BDD, the peak currents increased in the order FS-BDD-gr < FS-BDD-pol < FS-BDD-nucl, reflecting an increasing density of electrochemically active sp^2-related surface sites rather than a purely diffusion-controlled response.

3.3.2. ELECTROCHEMICAL DETECTION OF GLUCOSE ON BDD ELECTRODES

The electrochemical sensing of glucose on the BDD electrodes was investigated using LSV in 0.1 M NaOH solution with and without 15 mM glucose. In the absence of glucose (Fig. 3.5(a)), no oxidation peaks were detected for all BDD electrodes in the range from 0.2 to 1 V. In 15 mM glucose (Fig. 3.5(b)), oxidation peaks with increasing intensity were detected with FS-BDD-gr, FS-BDD-pol, and FS-BDD-nucl at 0.72 V, 0.75 V, and 0.76 V, respectively, which coincide with the potentials previously reported for glucose oxidation on thin-film and nanostructured BDD electrodes [13, 14, 18]. However, no oxidation could be observed at all with single-crystal BDD. Peak current densities of BDD electrodes within 15 mM glucose solution versus normalized Raman G-band values (see Fig. 3.3) and quinone-related oxidation peak values (see Fig. 3.4) are shown in Fig. 3.5(c). There, it can be clearly seen that the glucose oxidation peak increased with the increase of sp^2 carbon content, indicating thus higher catalytic activity.

Fig. 3.6 shows the linear sweep voltammetry curves for various glucose concentrations from 0 to 15 mM recorded with the four different BDD electrodes. It can be seen that the curves from single-crystal BDD with different glucose concentrations overlap each other, indicating that single-crystal BDD with its negligible sp^2 carbon is not catalytically active towards glucose oxidation. On the contrary, the three different FS-BDD electrode surfaces do catalyse glucose oxidation, and an increase in peak currents was

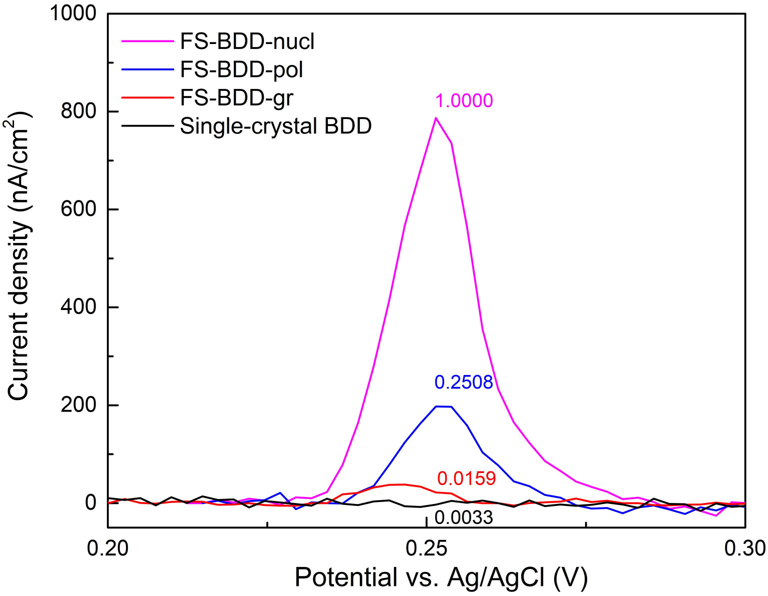

Figure 3.4: Quinone-related oxidation peaks for FS-BDD-nucl, FS-BDD-pol, FS-BDD-gr, and single-crystal BDD, in 0.1 M H_2SO_4 solution, at a scan rate of 0.1 V/s.

observed with increase in glucose concentration. Noticeable differences in response are evident though. There was a weak response towards glucose for FS-BDD-gr, which contains a relatively small amount of sp^2 carbon. The strongest response was found for FS-BDD-nucl, which is also richest in sp^2-bonded carbon.

In the sensitivity analysis, the response of the peak current density (i_{pa}) with varying glucose concentration was analysed for all BDD electrodes. Results are shown in Fig. 3.7. Because there is no apparent glucose oxidation peak on LSV using single-crystal BDD, the corresponding peak current densities were taken at the selected potential of 0.75 V. The response towards glucose for the FS-BDD-gr is linear in the range from 2 mM to 10 mM, which well covers the physiological range of 3–8 mM [14]. From a linear regression fit (see Table 3.1), a sensitivity of 0.78 μA mM^{-1} cm^{-2} was derived. FS-BDD-pol showed higher sensitivity of 1.37 μA mM^{-1} cm^{-2}, while FS-BDD-nucl demonstrated the highest sensitivity of 7.25 μA mM^{-1} cm^{-2} among all the BDD electrodes. The limit of detection for each of the three FS-BDD surfaces was estimated at a signal-to-noise ratio of 3, and is shown in Table 3.1. The likely explanation is that the relatively higher sp^2 carbon content within FS-BDD-nucl contributes to the enhanced electrocatalytic activity towards glucose. Since pure sp^2 carbon (glassy carbon) cannot detect glucose in the range of 0.2–1.0 V (see Fig. 3.8 and previous work [30]), this enhanced catalytic activity could either originate from boron-doped sp^2 carbon [31] or unsaturated catalytically active sites located between grain boundaries and grains [32].

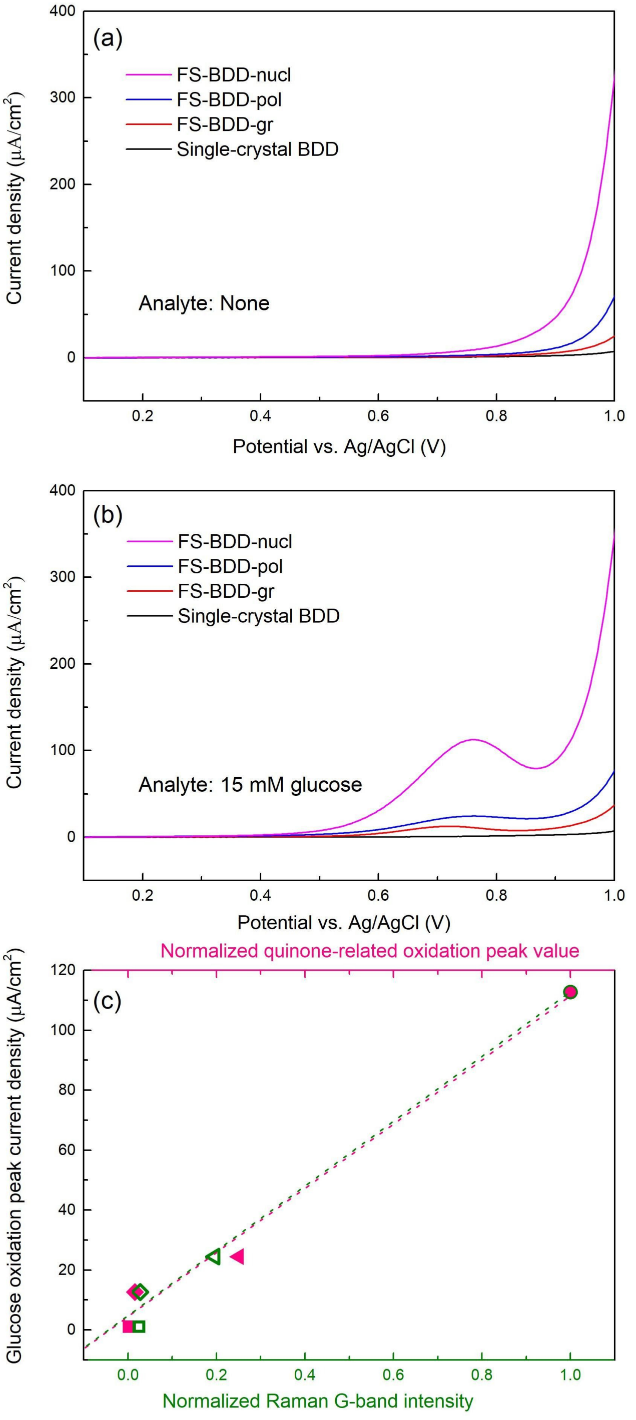

Figure 3.5: Linear sweep voltammetry of the various BDD electrodes measured in 0.1 M NaOH solution: (a) without glucose and (b) with 15 mM glucose. (c) Glucose oxidation peak current densities within 15 mM glucose solution versus normalized Raman G-band intensity (bottom x-axis) and quinone-related oxidation peak values (top x-axis), respectively.

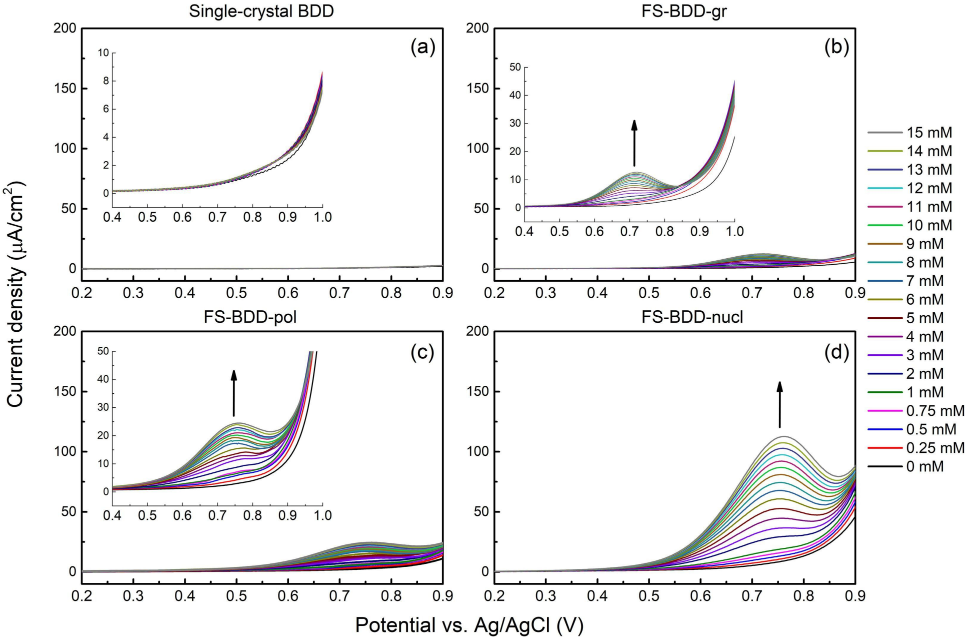

Figure 3.6: Linear sweep voltammetry of the various BDD electrodes measured in 0.1 M NaOH solution with glucose concentrations in the range from 0 to 15 mM.

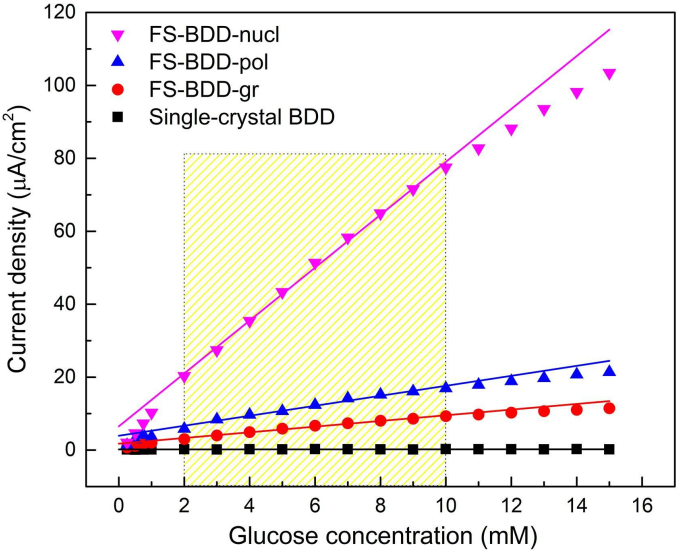

Figure 3.7: Peak current densities from the LSV curves of the various BDD electrodes in the range of 0–15 mM glucose. Linear fitting lines in the range from 2 to 10 mM are shown.

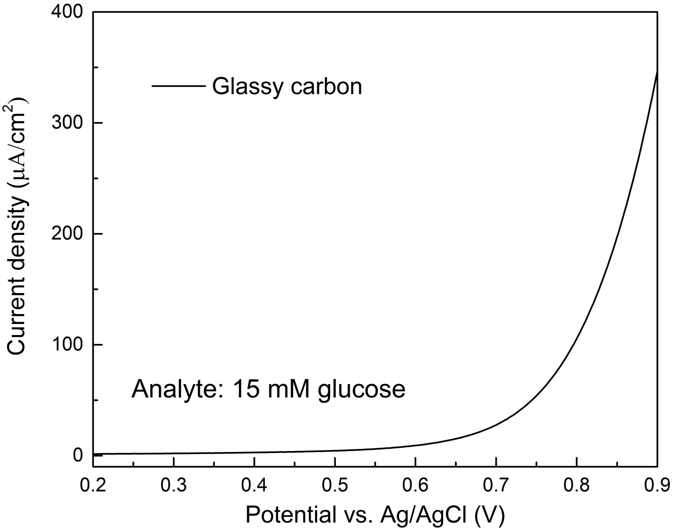

Figure 3.8: Linear sweep voltammetry of a glassy carbon electrode measured in 0.1 M NaOH solution with 15 mM glucose.

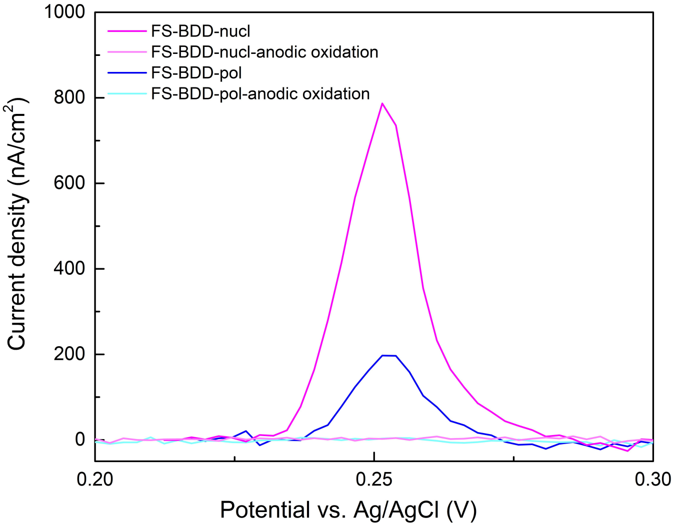

Figure 3.9: Quinone-related oxidation peaks for FS-BDD-pol and FS-BDD-nucl before and after anodic oxidation, in 0.1 M H_2SO_4 solution, at a scan rate of 0.1 V/s.

Table 3.1: Fitted data for the various FS-BDD electrode surfaces. Linear regression equations were derived from the data shown in Fig. 3.7 in the range from 2 to 10 mM, i_{pa} (μA) = $a + bC$, with b being the slope (sensitivity in μA mM^{-1} cm^{-2}) and C being the glucose concentration in mM. The limit of detection (LOD) for each of the three FS-BDD electrode surfaces was estimated at a signal-to-noise ratio of 3.

Material	***a***	***b (sensitivity)***	**Correlation coefficient**	**LOD**
FS-BDD-gr	1.58	0.78	0.99	750 μM
FS-BDD-pol	3.95	1.37	0.98	250 μM
FS-BDD-nucl	6.53	7.25	0.99	50 μM

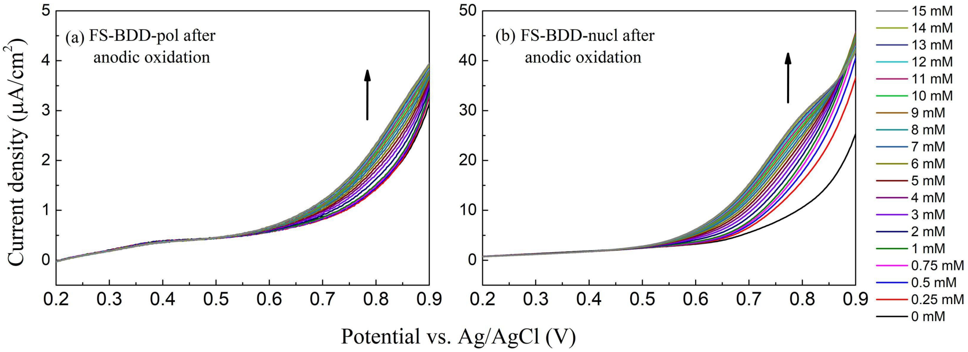

Figure 3.10: Linear sweep voltammetry performed with (a) FS-BDD-pol and (b) FS-BDD-nucl after 1-hour anodic oxidation treatment. Glucose concentrations in the range from 0 to 15 mM in 0.1 M NaOH solution.

3.3.3. Effect of sp^2 Carbon Removal on Glucose Detection

To prove the important role of sp^2 carbon in BDD-based electrochemical sensing towards glucose, FS-BDD-pol and FS-BDD-nucl were exposed to one hour anodic oxidation at 5 V to remove sp^2 carbon from the electrode surfaces [33]. It can be seen from Fig. 3.9 that quinone-related oxidation peaks of FS-BDD-pol and FS-BDD-nucl disappeared after anodic treatment, thus indicating negligible sp^2 was left. The linear sweep voltammetry curves for various glucose concentrations and the corresponding peak current densities recorded on FS-BDD-pol and FS-BDD-nucl after the anodic oxidation treatment are shown in Fig. 3.10 and Fig. 3.11, respectively.

It can be seen from Fig. 3.10(a) that the LSV curves for FS-BDD-pol changed drastically compared with the ones shown in Fig. 3.6(c), and, only when considering up to 5 μA cm^{-2}, a weak current response can be observed with varying glucose concentration. The current response of FS-BDD-nucl after removal of sp^2 carbon (Fig. 3.10(b)) was reduced with even greater magnitude as compared with the curves in Fig. 3.6(d). Linear regression of the peak current density vs. glucose concentration (Fig. 3.11) shows that the sensitivity of FS-BDD-pol dropped from 1.37 to 0.62 μA mM^{-1} cm^{-2}, and the sensitivity of FS-BDD-nucl decreased by nearly 9 times from 7.25 to 0.78 μA mM^{-1} cm^{-2}. These results provide strong indication that (B-doped) sp^2 carbon content is essential

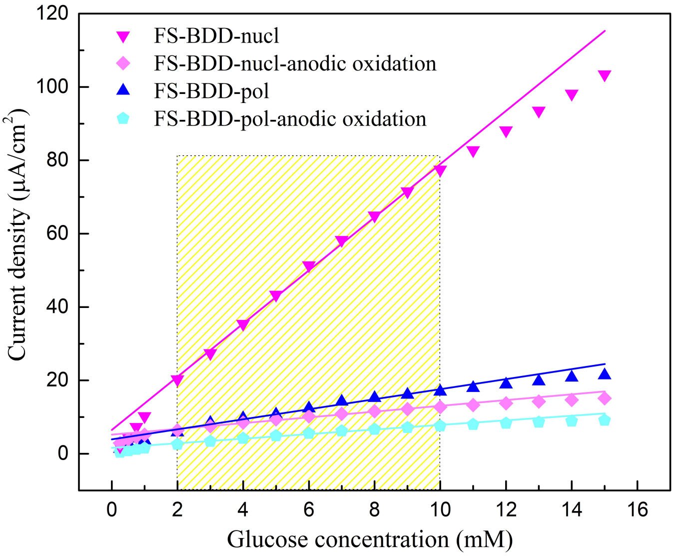

Figure 3.11: Peak current densities from the LSV curves of FS-BDD-pol and FS-BDD-nucl in the range of 0–15 mM glucose before and after anodic oxidation.

for electrochemical sensing of glucose using BDD electrodes.

3.4. CONCLUSION

In this work, BDD electrodes with controlled amounts of sp^2 carbon were systematically studied for non-enzymatic electrochemical detection of glucose. It was found that glucose oxidation on BDD electrodes is strongly affected by the surface sp^2 carbon content. Single-crystal BDD with negligible amount of sp^2 carbon is catalytically inert towards glucose oxidation. The FS-BDD electrode surfaces with different grain structures and sp^2-carbon content but equal boron-doping levels displayed different catalytic activities towards glucose sensing. Glucose oxidation in 0.1 M NaOH enhanced with the increase of the sp^2 carbon content. FS-BDD-gr with a small amount of sp^2 carbon showed a sensitivity of 0.78 μA mM^{-1} cm^{-2}, and the sensitivity of FS-BDD-pol was 1.37 μA mM^{-1} cm^{-2}. The FS-BDD-nucl electrode with the highest sp^2 carbon demonstrated the highest sensitivity of 7.25 μA mM^{-1} cm^{-2}. After removing sp^2 carbon by anodic oxidation, the sensitivities of FS-BDD-pol and FS-BDD-nucl dropped to 0.62 and 0.78 μA mM^{-1} cm^{-2}, respectively. Based on the above findings, we conclude that the electrocatalytic activity towards glucose oxidation is dependent on the amount of sp^2 carbon on the surface of the electrode.

BIBLIOGRAPHY

[1] E. G. Krug, “Trends in diabetes: sounding the alarm”, Lancet **387**, 1485–1486 (2016).

[2] E. Snouffer, “Latest figures show 463 million people now living with diabetes worldwide as numbers continue to rise”, Diabetes Res. Clin. Pract. **157**, 107932 (2019).

[3] J. M. Harris, C. Reyes, and G. P. Lopez, “Common causes of glucose oxidase instability in in vivo biosensing: a brief review”, J. Diabetes Sci. Technol. **7**, 1030–1038 (2013).

[4] W. C. Lee, K. B. Kim, N. G. Gurudatt, K. K. Hussain, C. S. Choi, D. S. Park, and Y. B. Shim, “Comparison of enzymatic and non-enzymatic glucose sensors based on hierarchical Au-Ni alloy with conductive polymer”, Biosens. Bioelectron. **130**, 48–54 (2019).

[5] S. Park, H. Boo, and T. D. Chung, “Electrochemical non-enzymatic glucose sensors”, Anal. Chim. Acta **556**, 46–57 (2006).

[6] K. E. Toghill and R. G. Compton, “Electrochemical non-enzymatic glucose sensors: a perspective and an evaluation”, Int. J. Electrochem. Sci. **5**, 1246–1301 (2010).

[7] D. W. Hwang, S. Lee, M. Seo, and T. D. Chung, “Recent advances in electrochemical non-enzymatic glucose sensors – a review”, Anal. Chim. Acta **1033**, 1–34 (2018).

[8] V. Sridhar and H. Park, “Carbon encapsulated cobalt sulfide nano-particles anchored on reduced graphene oxide as high capacity anodes for sodium-ion batteries and glucose sensor”, J. Alloys Compd. **764**, 490–497 (2018).

[9] P. Liu, M. Zhang, S. Xie, S. Wang, W. Cheng, and F. Cheng, “Non-enzymatic glucose biosensor based on palladium-copper oxide nanocomposites synthesized via galvanic replacement reaction”, Sensors Actuators, B Chem. **253**, 552–558 (2017).

[10] C. L. Sun, W. L. Cheng, T. K. Hsu, C. W. Chang, J. L. Chang, and J. M. Zen, “Ultrasensitive and highly stable nonenzymatic glucose sensor by a CuO/graphene-modified screen-printed carbon electrode integrated with flow-injection analysis”, Electrochem. Commun. **30**, 91–94 (2013).

[11] C. Xia and W. Ning, “A novel non-enzymatic electrochemical glucose sensor modified with FeOOH nanowire”, Electrochem. Commun. **12**, 1581–1584 (2010).

[12] J. V. Macpherson, “A practical guide to using boron doped diamond in electrochemical research”, Phys. Chem. Chem. Phys. **17**, 2935–2949 (2015).

[13] J. Lee and S. M. Park, “Direct electrochemical assay of glucose using boron-doped diamond electrodes”, Anal. Chim. Acta **545**, 27–32 (2005).

[14] Q. Wang, P. Subramanian, M. Li, W. S. Yeap, K. Haenen, Y. Coffinier, R. Boukherroub, and S. Szunerits, “Non-enzymatic glucose sensing on long and short diamond nanowire electrodes”, Electrochem. Commun. **34**, 286–290 (2013).

[15] Y. Zou, L. He, K. Dou, S. Wang, P. Ke, and A. Wang, “Amperometric glucose sensor based on boron doped microcrystalline diamond film electrode with different boron doping levels”, RSC Adv. **4**, 58349–58356 (2014).

[16] Z. Gong, N. Hu, W. Ye, K. Zheng, C. Li, L. Ma, Q. Wei, Z. Yu, K. Zhou, N. Huang, C. T. Lin, and J. Luo, “High-performance non-enzymatic glucose sensor based on Ni/Cu/boron-doped diamond electrode”, J. Electroanal. Chem. **841**, 135–141 (2019).

[17] D. Medeiros De Araújo, P. Canizares, C. A. Martínez-Huitle, and M. A. Rodrigo, “Electrochemical conversion/combustion of a model organic pollutant on BDD anode: role of sp^2/sp^3 ratio”, Electrochem. Commun. **47**, 37–40 (2014).

[18] D. Luo, L. Wu, and J. Zhi, “Fabrication of boron-doped diamond nanorod forest electrodes and their application in nonenzymatic amperometric glucose biosensing”, ACS Nano **3**, 2121–2128 (2009).

[19] T. L. Read, S. J. Cobb, and J. V. Macpherson, “An sp^2 patterned boron doped diamond electrode for the simultaneous detection of dissolved oxygen and pH”, ACS Sensors **4**, 756–763 (2019).

[20] A. J. Lucio, R. E. P. Meyler, M. A. Edwards, and J. V. Macpherson, “Investigation of sp^2-carbon pattern geometry in boron-doped diamond electrodes for the electrochemical quantification of hypochlorite at high concentrations”, ACS Sensors **5**, 789–797 (2020).

[21] J. Zhao, L. Wu, and J. Zhi, “Non-enzymatic glucose detection using as-prepared boron-doped diamond thin-film electrodes”, Analyst **134**, 794–799 (2009).

[22] T. Watanabe, T. A. Ivandini, Y. Makide, A. Fujishima, and Y. Einaga, “Selective detection method derived from a controlled diffusion process at metal-modified diamond electrodes”, Anal. Chem. **78**, 7857–7860 (2006).

[23] W. Dai, M. Li, S. Gao, H. Li, C. Li, S. Xu, X. Wu, and B. Yang, “Fabrication of nickel/nanodiamond/boron-doped diamond electrode for non-enzymatic glucose biosensor”, Electrochim. Acta **187**, 413–421 (2016).

[24] Z. Liu, S. Baluchová, A. F. Sartori, Z. Li, Y. Gonzalez-Garcia, M. Schreck, and J. G. Buijnsters, “Heavily boron-doped diamond grown on scalable heteroepitaxial quasi-substrates: a promising single crystal material for electrochemical sensing applications”, Carbon **201**, 1229–1240 (2023).

[25] K. Ushizawa, K. Watanabe, T. Ando, I. Sakaguchi, M. Nishitani-Gamo, Y. Sato, and H. Kanda, “Boron concentration dependence of Raman spectra on 100 and 111 facets of B-doped CVD diamond”, Diam. Relat. Mater. **7**, 1719–1722 (1998).

[26] D. M. Popova, B. N. Mavrin, V. N. Denisov, and E. A. Skryleva, “Spectroscopic and first-principles studies of boron-doped diamond: Raman polarizability and local vibrational bands”, Diam. Relat. Mater. **18**, 850–853 (2009).

[27] A. Merlen, J. G. Buijnsters, and C. Pardanaud, “A guide to and review of the use of multiwavelength Raman spectroscopy for characterizing defective aromatic carbon solids: from graphene to amorphous carbons”, Coatings **7**, 153 (2017).

[28] A. F. Sartori, S. Orlando, A. Bellucci, D. M. Trucchi, S. Abrahami, T. Boehme, T. Hantschel, W. Vandervorst, and J. G. Buijnsters, “Laser-induced periodic surface structures (LIPSS) on heavily boron-doped diamond for electrode applications”, ACS Appl. Mater. Interfaces **10**, 43236–43251 (2018).

[29] Z. J. Ayres, S. J. Cobb, M. E. Newton, and J. V. Macpherson, “Quinone electrochemistry for the comparative assessment of sp^2 surface content of boron doped diamond electrodes”, Electrochem. Commun. **72**, 59–63 (2016).

[30] A. Raziq, M. Tariq, R. Hussian, M. H. Mehmood, M. S. Khan, and A. Hassan, “Electrochemical investigation of glucose oxidation on a glassy carbon electrode using voltammetric, amperometric, and digital simulation methods”, ChemistrySelect **2**, 9711–9717 (2017).

[31] K. Siuzdak, M. Ficek, M. Sobaszek, J. Ryl, M. Gnyba, P. Niedziałkowski, N. Malinowska, J. Karczewski, and R. Bogdanowicz, “Boron-enhanced growth of micron-scale carbon-based nanowalls: a route toward high rates of electrochemical biosensing”, ACS Appl. Mater. Interfaces **9**, 12982–12992 (2017).

[32] J. Zhang, D. S. Su, R. Blume, R. Schlogl, R. Wang, X. Yang, and A. Gajović, “Surface chemistry and catalytic reactivity of a nanodiamond in the steam-free dehydrogenation of ethylbenzene”, Angew. Chemie **122**, 8822–8826 (2010).

[33] S. J. Cobb, F. H. J. Laidlaw, G. West, G. Wood, M. E. Newton, R. Beanland, and J. V. Macpherson, “Assessment of acid and thermal oxidation treatments for removing sp^2 bonded carbon from the surface of boron doped diamond”, Carbon **167**, 1–10 (2020).

4

4

HEAVILY BORON-DOPED DIAMOND GROWN ON SCALABLE HETEROEPITAXIAL QUASI-SUBSTRATES: A PROMISING SINGLE CRYSTAL MATERIAL FOR ELECTROCHEMICAL SENSING APPLICATIONS

This work focuses on fabricating and characterizing three heteroepitaxial single-crystal boron-doped diamond (SC-BDD) electrodes. The heteroepitaxy method enabled the synthesis of large-area (1 cm^2), heavily-doped (100)-oriented SC-BDD electrodes. Cyclic voltammetry (CV) showed wide potential windows, low double-layer capacitance, and near-reversible redox response. Scanning electrochemical microscopy highlighted homogeneously distributed activity, with minor performance differences linked to surface morphology. Dopamine sensing demonstrated practical application potential, while enhanced fouling resistance was confirmed using anthraquinone-2,6-disulfonate. These findings establish heteroepitaxial SC-BDD as a scalable and high-performance material for advanced electrochemical applications.

The contents of this chapter have been published in:

- Z. Liu, S. Baluchová, A. F. Sartori, Z. Li, Y. Gonzalez-Garcia, M. Schreck, and J. G. Buijnsters, “Heavily boron-doped diamond grown on scalable heteroepitaxial quasi-substrates: A promising single crystal material for electrochemical sensing applications,” *Carbon* **201**, 1229–1240 (2023). DOI:10.1016/j.carbon.2022.10.023

4.1. INTRODUCTION

Electrically conductive boron-doped diamond (BDD) is a remarkably versatile electrode material [1], which has been extensively employed in numerous electrochemical applications, such as electroanalysis and (bio)sensors development [2, 3], pollutant degradation and waste-water treatment [4–7], electro-organic synthesis [8], electrocatalysis [9], and electrochemical energy storage [10] as well as in “non-electrochemical” research fields, including biomedicine and neuroscience [11, 12]. The unprecedented popularity of BDD, particularly in electroanalysis, results from a large range of outstanding characteristics, distinguishing BDD from other commonly employed carbonaceous and metallic electrodes. These properties include exceptional chemical and mechanical stability, resistance towards corrosion and (bio)fouling, wide working potential window, possibility of *in-situ* electrochemical activation, dopant-controlled adjustable conductivity, low noise and background current, and biocompatibility [1, 2].

Notably, a vast majority of BDD electrodes produced and employed for sensor development are of polycrystalline nature with diamond grains composed of various crystal facets and with related grain boundaries. The polycrystalline BDD surface is thus inhomogeneous, and the following aspects must be considered carefully:

- The incorporation efficiency of boron dopant into the diamond layer is strongly influenced by the crystallographic orientation of the growth facets; the uptake decreases in the following order: (111) > (110) > (100) [13, 14]. This naturally results in heterogeneous doping and distribution of boron carriers within the BDD layer, creating less or more conductive domains [15], influencing the diffusion field and kinetics of electron transfer (ET) reactions.

- As-prepared BDD electrodes are hydrogen (H)-terminated with hydrophobic, non-polar surfaces, which can be, however, converted into oxygen (O)-terminated, and thus hydrophilic and polar surfaces [16, 17], by suitable (*in-situ*) pre-treatment procedures. The conversion from H- to O-termination is, though, also affected by the crystallographic orientation of the diamond grains as the propensity towards oxidation differs between the individual grain planes: (110) facet was identified to be more prone to oxidation than (100) and (111) facets [18].

- Non-diamond (sp^2) carbon impurity typically resides in the grain boundary phases [1, 17]. The presence of sp^2 carbon impurities, more pronounced in heavily doped BDD electrodes [19], is electrochemically indicated by narrowed potential windows, increased background currents and higher proclivity towards adsorption [17, 20], which are all detrimental phenomena in electroanalysis.

The polycrystalline character of BDD thus significantly affects the electrochemical properties, and consequently ET kinetics at the electrode–electrolyte interface. To study the inherent electrochemical features of BDD, the above-mentioned factors contributing to its heterogeneity must be eliminated. This can be achieved by preparing and using a single-crystal (SC) form of conductive diamond with a well-defined surface composition and orientation. Until now, only a few studies have utilised and clarified the performance of high-quality SC-BDD electrodes, while most attention has been paid to the crystallographic orientations which naturally occur in polycrystalline diamond, i.e., (100) and (111) [14, 21–24].

Substantially faster ET kinetics for $[Ru(NH_3)_6]^{3+/2+}$ and $[Fe(CN)_6]^{3-/4-}$ redox markers have been observed on (111) facet compared to (100)-oriented SC-BDD [22]. This was explained by the fact that both SC-BDD electrodes were deposited using the same B/C ratio, but due to the differences in boron uptake efficiency of (100) and (111) surfaces, the resulting boron concentration ([B]) in the diamond films varied by one order of magnitude ([B] of 2×10^{18} cm^{-3} for (100) vs. 2×10^{19} cm^{-3} for (111)). Such variation in doping level, and thus conductivity, naturally manifested in the obtained electrochemical responses for tested redox couples. In another work, Pleskov et al. concluded that identically doped (100) and (111)-oriented SC-BDD electrodes ([B] of 6×10^{18} cm^{-3}) provided comparable ET kinetics of $[Ru(NH_3)_6]^{3+/2+}$ and $[Fe(CN)_6]^{3-/4-}$, unaffected by the crystallographic orientation [14]. However, Ivandini et al. [23] studied (100) and (111)-faceted SC-BDD electrodes of higher boron doping (both facets contained [B] $\sim 4 \times 10^{20}$ cm^{-3}) and, despite the similar doping level, more sluggish ET kinetics and smaller peak currents of $[Ru(NH_3)_6]^{3+/2+}$ and $[Fe(CN)_6]^{3-/4-}$ couples were recorded on (100) surface in comparison with the (111) crystal. In this case, crystallographic orientation, particularly the difference in magnitude in band bending and the thickness of the space charge layer, was identified as the main factor responsible for different electrochemical behaviour of tested (100) and (111) SC-BDD electrodes [23]. Besides, less “conventional” monocrystalline diamond facets such as (113), (115) and (118) have been recently prepared and used as a substrate for SC-BDD deposition [25, 26]; among them, the highest boron incorporation efficiency was confirmed for the (113) plane [25].

It is important to point out that all SC-BDD electrodes examined in these reports were homoepitaxially grown on synthetic single-crystal diamond substrates with a size of few mm^2. Such limitation in the crystal size presents the major drawback of homoepitaxial growth and restricts the use of SC-BDD for electrochemical sensing and pollutant degradation; particularly for the latter application satisfactorily high surface area is essential. One promising approach to effectively tackle the size issue is to employ heteroepitaxy, in which epitaxial nucleation and growth of diamond is controlled upon the surface of a different crystalline material [27]. Consequently, the selection of optimal substrate and suitable nucleation method is crucial for successful fabrication of high-quality heteroepitaxial diamond layers [27, 28]. The combination of iridium-based materials and bias-enhanced nucleation technique has been recognized as the most suitable for diamond heteroepitaxy and has resulted in the preparation of the free-standing monocrystalline diamond wafer with a diameter of 9.2 cm by Schreck’s group [28]. The same group investigated boron doping of heteroepitaxial SC diamond films and evaluated their composition, structure and functionality for the realization of competitive electronic devices and sensors [29, 30].

In the present study, the diamond heteroepitaxy approach was applied for the first time to synthesize large-area (1 cm^2) and heavily-doped ([B] > 10^{21} cm^{-3}) (100)-oriented SC-BDD electrodes. BDD layers were grown on both on-axis and off-axis quasi-substrates to study the impact of a small off-cut angle. A total of three SC-BDD samples were prepared differing in their surface morphology. Scanning electron microscopy (SEM), atomic force microscopy (AFM) and two-dimensional X-ray diffraction (2D XRD) were used for surface and crystallographic analysis. The electrochemical properties of the BDD layers grown on heteroepitaxial diamond quasi-substrates were investigated and compared to the performance of conventional poly-BDD. Cyclic voltammetry (CV) was performed in solutions of a supporting electrolyte (0.1 M KNO_3) and two redox probes ($[Ru(NH_3)_6]^{3+/2+}$ and $[Fe(CN)_6]^{3-/4-}$) to assess important electrochemical characteristics such as the width of the potential window, double-layer capacitance (C_{dl}) and peak-to-peak separation (ΔE_p) values reflecting the rate of ET kinetics. Besides, scanning electrochemical microscopy (SECM) was employed to probe the distribution of the electrochemical activity of the SC-BDD and poly-BDD surfaces. Finally, the heteroepitaxial SC-BDD electrodes were subjected to voltammetric experiments with more complex organic molecules, namely dopamine to evaluate their perspective for sensing applications, and anthraquinone-2,6-disulfonate (AQDS) to demonstrate their anti-fouling property.

4.2. EXPERIMENTAL

4.2.1. PREPARATION OF THE IR/YSZ/SI(100) SUBSTRATE

The preparation of the substrate used for heteroepitaxial diamond growth has been reported in [29]. Briefly, pulsed laser deposition of a heteroepitaxial yttria-stabilized zirconia (YSZ) film of several tens of nanometers thickness was carried out on a 3-mm thick, 4° off-axis Si(100) wafer (4 inch). Subsequently, a ~150 nm thick single-crystal iridium layer was grown using e-beam evaporation at 650 °C on the top of the YSZ film. To grow a monocrystalline intrinsic diamond, the Ir/YSZ/Si(100) substrate was first subjected to a bias-enhanced nucleation process in a microwave plasma-enhanced chemical vapor deposition reactor (MWPCVD) by applying a bias voltage of −300V in an atmosphere of 3% CH_4 in H_2. Then, a ~1.3 – 1.4 mm thick diamond layer was grown on the nucleated Ir/YSZ/Si(100) stack in a high-power microwave setup at 150 – 200 mbar with a gas phase consisting of 8% CH_4 in H_2 and several tens of ppm of N_2.

4.2.2. FABRICATION OF HETEROEPITAXIAL SC-BDD LAYERS

Fig. 4.1 illustrates the preparation of the three heteroepitaxial SC-BDD electrodes using the multi-layered stack (Fig. 4.1(a)). Prior to BDD growth, the YSZ/Si(100) was etched away, the iridium layer was removed by mechanical polishing, and the wafer (4 inch) was sliced by an IR laser into 1 × 1 cm^2 pieces which resulted in free-standing single crystal diamond samples, as depicted in Fig. 4.1(b). Then, the heteroepitaxial diamond quasi-substrates were exposed to the following processing (Fig. 4.1(c)): For samples A and B, 4° off-axis was preserved and the top (growth) side of sample A was polished (the back side of both samples was already polished due to removal of iridium layer), while sample C was polished on both sides to eliminate the off-axis angle. This also resulted in a lower thickness of sample C than samples A and B (0.26 mm vs. 1.37–1.29 mm, respectively). Finally, reactive ion etching was applied to remove polishing-induced crystal damage that is known to cause the nucleation of dislocations in subsequent homoepitaxial growth steps.

As further shown in Fig. 4.1(d), the BDD layers were grown either on the polished

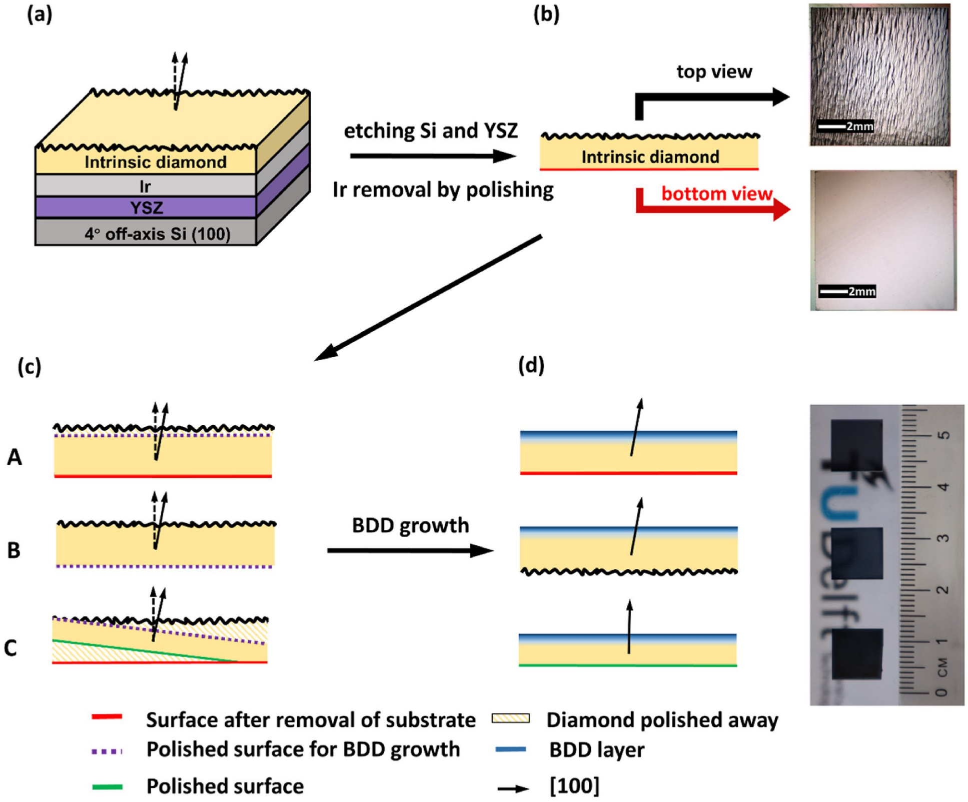

Figure 4.1: Schematic displaying the fabrication of the three heteroepitaxial SC-BDD electrodes. (a) The layered stack was subjected to etching to remove YSZ and Si(100) and then to polishing to remove the Ir layer, which resulted in (b) free-standing, heteroepitaxially grown intrinsic diamond with 4° off-axis (100) plane, whose top and bottom views were visualized by a digital microscope. (c) The intrinsic diamond was further processed: For samples A and B, 4° off-axis was preserved, and the top (growth) side of sample A was polished (the back side of both samples was already polished due to Ir layer removal), while sample C was polished on both sides to eliminate the off-axis angle. (d) BDD layers were grown either on the polished top side (samples A and C) or the back side (sample B; flipped by 180° prior to BDD growth step) of the heteroepitaxial diamond quasi-substrate. Prepared (100)-faceted SC-BDD electrodes (1 cm^2) are shown in the picture (ruler with cm-scale).

top side (samples A and C) or the back side (sample B) of the heteroepitaxial (100) diamond quasi-substrate. The main difference between the top and back side of the heteroepitaxial diamond is the dislocation density, being higher on the back side (originally interfacing the iridium layer) [31, 32]. To test if the increased amount of dislocations impacts substantially the final electrode performance, both sides were used for the BDD growth carried out under the following conditions: 1.1 kW microwave power, 750–850 °C substrate temperature, 50 mbar pressure and 4 h growth duration, while the gas mixture consisting of CH_4 and trimethylboron diluted in H_2 was carefully controlled to achieve heavy boron doping of $[B] > 10^{21}$ atoms cm^{-3}. To be more specific, the BDD growth process on the heteroepitaxial diamond pseudo-substrates was divided into three phases in order to achieve high boron doping levels:

A. 1 hour: 71 sccm H_2, 8 sccm CH_4, 320 sccm trimethylborane (TMB; 1000 ppm diluted in H_2), 1 sccm CO_2;

B. 1 hour: 0 sccm H_2, 8 sccm CH_4, 392 sccm TMB, 0.5 sccm CO_2;

C. 2 hours: 0 sccm H_2, 8 sccm CH_4, 392 sccm TMB, 0 sccm CO_2.

In phases (B) and (C), the hydrogen was introduced into the deposition chamber along with the (diluted) TMB. As-produced SC-BDD electrodes will be labelled as SC-BDD A, SC-BDD B and SC-BDD C, respectively, from here onwards.

As shown in Fig. 4.1, heteroepitaxial SC-BDD electrodes with dimensions of 1 × 1 cm^2 were prepared, which already represents a significant improvement in size compared to previously reported studies utilizing homoepitaxially grown SC-BDD (with an area of a few mm^2). This size of the electrodes was selected purely for practical reasons (fitting into a home-built voltammetric cell); however, the herein reported heteroepitaxy approach allows scaling up to even larger areas [28], if required by intended applications, e.g., in wastewater treatment, electrosynthesis, and electrocatalysis.

4.2.3. SURFACE AND CRYSTALLOGRAPHIC CHARACTERIZATION

The surface morphology of the heteroepitaxial SC-BDD layers and poly-BDD was visualized using a scanning electron microscope (JEOL JSM6500F) in a secondary electron imaging mode operated at 15 keV. Surface roughness was determined from AFM measurements performed with a JPK Nanowizard 4 in tapping mode using silicon tips over a scanned area of 60 × 60 μm^2. Raman spectra were measured with a Horiba LabRAM HR device equipped with an argon-ion laser operating at a 514 nm wavelength. 2D XRD patterns were recorded using a Bruker D8 Discover diffractometer with an Eiger 2500k detector and CuKα radiation. Optical images of the top and bottom views of the free-standing intrinsic diamond were taken with a digital microscope (VHX-6000, Keyence, Belgium), and a photo of the final heteroepitaxial SC-BDD electrodes was captured using an EOS M50 Canon camera.

4.2.4. ELECTROCHEMICAL MEASUREMENTS

Electrochemical measurements, including CV, differential pulse voltammetry (DPV), and Mott-Schottky analysis, were carried out using an Autolab PGSTAT 128N equipped with the FRA module and controlled by Nova 2.1 software (Metrohm, The Netherlands) in a home-built cylindrical PTFE cell (100 mL). A standard three-electrode setup was used in which an Ag/AgCl (3 M KCl) and a 5.7 cm long platinum wire (both obtained from ALS Co, Japan) served as the reference and counter electrodes, respectively. The heteroepitaxially grown SC-BDD samples and poly-BDD electrode were employed as the working electrode. A free-standing poly-BDD sample (1.5 × 1.5 cm^2, 0.7 mm thickness, and [B] of 3×10^{20} cm^{-3} [33]) originating from Diafilm EP Grade BDD (Element Six, UK) was obtained from Mintres B.V. (The Netherlands). The growth side of the poly-BDD subjected to examination was chemically mechanically polished until a surface roughness of ~5 nm was reached.

The BDD-based working electrode was placed in the PTFE cell from underneath and sealed by a chemically resistant O-ring (Kalrez® Spectrum™ 6375, model AS568), while a geometrical area of 0.22 cm^2 was exposed to the measuring solution. The current densities reported in this work were calculated using the O-ring defined geometric area. Since the heteroepitaxial SC-BDD electrodes are only one-side doped, electric contact to the doped surface was realized with conductive silver paint, applied from the four corners towards the backside, and contacted by a copper disc wired to the potentiostat.

To ensure satisfactory surface cleanliness and repeatability of the measurements, all BDD electrodes were cleaned and pre-treated in the same way. In the first step, BDD electrodes were boiled for 5 min in an acid mixture prepared by mixing concentrated HCl, H_2SO_4, and HNO_3 in a ratio of 2:2:3, which generated a highly stable O-terminated surface [34]. Previous studies showed that hydroxyl/ether (-C-O-H/-C-O-C) and carbonyl (>C=O) groups are the most abundant oxygen functionalities present on the oxidized (100)-oriented crystal facet [23, 35]. The second step involved ultrasonic cleaning of the oxidized BDD samples in acetone, isopropanol, and deionized water, each for 5 min. Lastly, the electrodes were subjected to 20 consecutive CV scans in the potential range from 0 V to +1.0 V in 0.1 M KNO_3 at a scan rate of 0.1 V s^{-1} to stabilize the baseline. At the beginning of every measuring day, the BDD samples were anodically treated and renewed by applying a high positive potential of +2.5 V for 15 min in 0.1 M H_2SO_4.

Further, CVs were recorded in 0.1 M KNO_3 in the potential range between 0 V and +1.0 V, and the following equation (Eq. 4.1) was employed to estimate C_{dl} values:

$$C_{dl} = \frac{\Delta I_{AV}}{A_{geom} \cdot v} \tag{4.1}$$

where ΔI_{AV} (in A) is the average background current difference between the forward and reversed scan at a potential of +0.5 V, A_{geom} represents the geometric surface area (0.22 cm^2), and v is the scan rate (0.1 V s^{-1}).

To probe the anti-fouling property of the electrodes, CV experiments were performed in a solution of 1 mM AQDS in 0.1 M $HClO_4$ (n = 20, at a scan rate of 0.1 V s^{-1}). Next, electrodes were rinsed 5 times with deionized water to remove weakly adsorbed species. After rinsing, the electrodes were immersed only in 0.1 M $HClO_4$ (without AQDS) to repeat the CV measurements. This set of experiments was performed not only with BDD-based electrodes but also with a glassy carbon electrode (GCE, A_{geom} of 0.20 cm^2; obtained from ALS Co, Japan) pre-treated by polishing on alumina slurry.

DP voltammograms were recorded using a pulse amplitude of +50 mV, pulse width of 80 ms, potential step of 10 mV, and a scan rate of 20 mV s^{-1}. The concentration dependences were plotted from the average of four replicate DPV measurements for each dopamine standard solution and evaluated by the least squares linear regression method. Limits of detection (LOD) were calculated as a threefold and limits of quantification (LOQ) as a tenfold of the standard deviation of the intercept, divided by the slope of the corresponding calibration plot.

The Mott-Schottky (MS) plots were measured in 0.1 M KNO_3 solution in the potential range from −0.4 V to +0.8 V at a frequency of 160 Hz, and subsequently, the Mott-

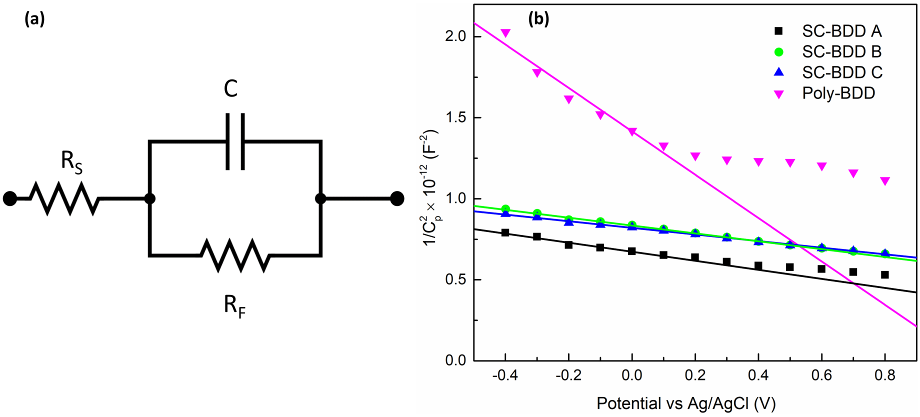

Figure 4.2: (a) Simplified Randles equivalent circuit consisting of a solution resistance (R_S) in series with a parallel combination of a capacitance (C_p) and a film resistance (R_F), used to extract C_p values from the impedance data. (b) Mott-Schottky curves measured at a frequency of 160 Hz of (—) SC-BDD A, (—) SC-BDD B, (—) SC-BDD C, and (—) poly-BDD. Red dashed lines indicate the range used for fitting.

Schottky equation (Eq. 4.2) was used to estimate charge carrier concentration (N_A) [36]:

$$N_A = \frac{-2}{e\varepsilon_0\varepsilon_r A^2 \frac{d(C_p^{-2})}{dE}} \tag{4.2}$$

where e is an elementary charge, ε_0 is the permittivity of vacuum, ε_r is the relative permittivity of diamond material, A is the electrode area, and C_p^{-2} is the capacitance obtained at various potential values E. C_p values were evaluated from impedance data (1 Hz–25 kHz frequency range, 10 mV amplitude) fitted with the simplified Randles equivalent circuit depicted in Fig. 4.2.

SECM measurements were conducted using a Scanning Electrochemical Workstation Model 370 (Ametek Scientific Instruments, USA) to evaluate the (in)homogeneous distribution of electrochemical activity of the different BDD surfaces. A four-electrode cell was used with a Pt microelectrode probe tip (10 μm diameter) and the BDD samples as working electrodes (WE1 - Pt and WE2 - BDD). The cell was completed with an Ag/AgCl (3 M KCl) and a Pt wire serving as the reference and counter electrodes, respectively. The SECM was operated under feedback mode using 1 mM $[\mathrm{Ru(NH_3)_6}]^{3+/2+}$ (0.1 M $\mathrm{KNO_3}$) as a redox mediator. The redox potential used for the reduction of the mediator at the Pt microprobe tip was −0.4 V. At the same time, the BDD samples were polarized at 0 V.

Approach curves were carried out to elucidate the electrochemical nature of the BDD surface (active or inactive). The Pt probe tip was carefully approached to the substrate (BDD surface) in the feedback mode at a rate of 0.1 μm s^{-1}. Whether the reduced species diffuse to an electrochemically active (conductive) or inactive (non-conductive) site on the BDD electrodes, the Pt probe shows a positive or negative feedback response, respectively. The positive feedback results from the oxidation of the mediator at the conductive sites. Curves were displayed using normalized current (I) and distance (L). I corresponds to the ratio between the measured probe current (i_T) and the steady-state current ($i_{T\infty}$) recorded far from the substrate. L represents the ratio between substrate-to-probe tip distance (d) and the tip radius (r). The SECM maps of the BDD electrodes were recorded in an area of 60 × 60 μm^2 with a scanning rate of 5 μm s^{-1}, while the tip-substrate distance was fixed to 20 μm.

The electroanalytical measurements were carried out at room temperature (23 ± 1 °C). All reported potential values are referred to the Ag/AgCl electrode.

4.2.5. CHEMICALS

Hexaammineruthenium(III) chloride (≥98.0%), potassium hexacyanoferrate(II) trihydrate (≥98.5%), potassium nitrite (≥99.0%), sulphuric acid (95.0–98.0%), hydrochloric acid (37%), nitric acid (70%), phosphate buffered saline (powder, pH 7.4), isopropanol, acetone, disodium anthraquinone-2,6-disulfonate (AQDS, ≥97.0%), and dopamine hydrochloride (≥98.0%) were purchased from Merck and used without any further purification. Deionized water, ultra-filtrated with a Millipore Milli-Q system (resulting resistivity of 18.2 MΩ cm), was used to prepare all aqueous solutions.

4.3. RESULTS AND DISCUSSION

4.3.1. SURFACE CHARACTERRIZATION

Table 4.1: Morphological and electrochemical characteristics of studied BDD electrodes.

BDD electrode	**SC-BDD A**	**SC-BDD B**	**SC-BDD C**	**Poly-BDD**
Overall thickness (mm)	1.37	1.29	0.26	0.72
S_a (nm)	3.9	3.4	8.8	5.2
Potential window (V)	3.31	3.30	3.34	2.51
C_{dl} (μF cm^{-2})	3.5	3.7	3.9	4.6
$[B]_{\text{Raman}}$ (atoms cm^{-3})	2.7×10^{21}	2.5×10^{21}	4.4×10^{21}	1.8×10^{20}
$[B]_{\text{MS}}$ (atoms cm^{-3})	2.0×10^{21}	2.2×10^{21}	2.7×10^{21}	2.0×10^{20}
ΔE_p – $[\text{Ru(NH}_3)_6]^{3+/2+}$ (V)	0.067	0.068	0.067	0.067
ΔE_p – $[\text{Fe(CN)}_6]^{3-/4-}$ (V)	0.232	0.276	0.305	0.371
$E_{pA,\text{DA}}$ (V)	+0.637	+0.691	+0.752	+0.630
ΔE_p – DA/o-DQ (V)	0.642	0.703	0.793	0.673
Decrease in $I_{pA,\text{DA}}$ (for $n = 5$, %)	13.7	13.4	12.7	42.1

The surface morphology of all SC-BDD and poly-BDD electrodes was observed by SEM and AFM; the representative micrographs are depicted in Fig. 4.3. Moreover, AFM provided information on the arithmetic mean surface roughness (*Sa*), and the values are summarized in Table 4.1. Variations in surface morphological features of the individual

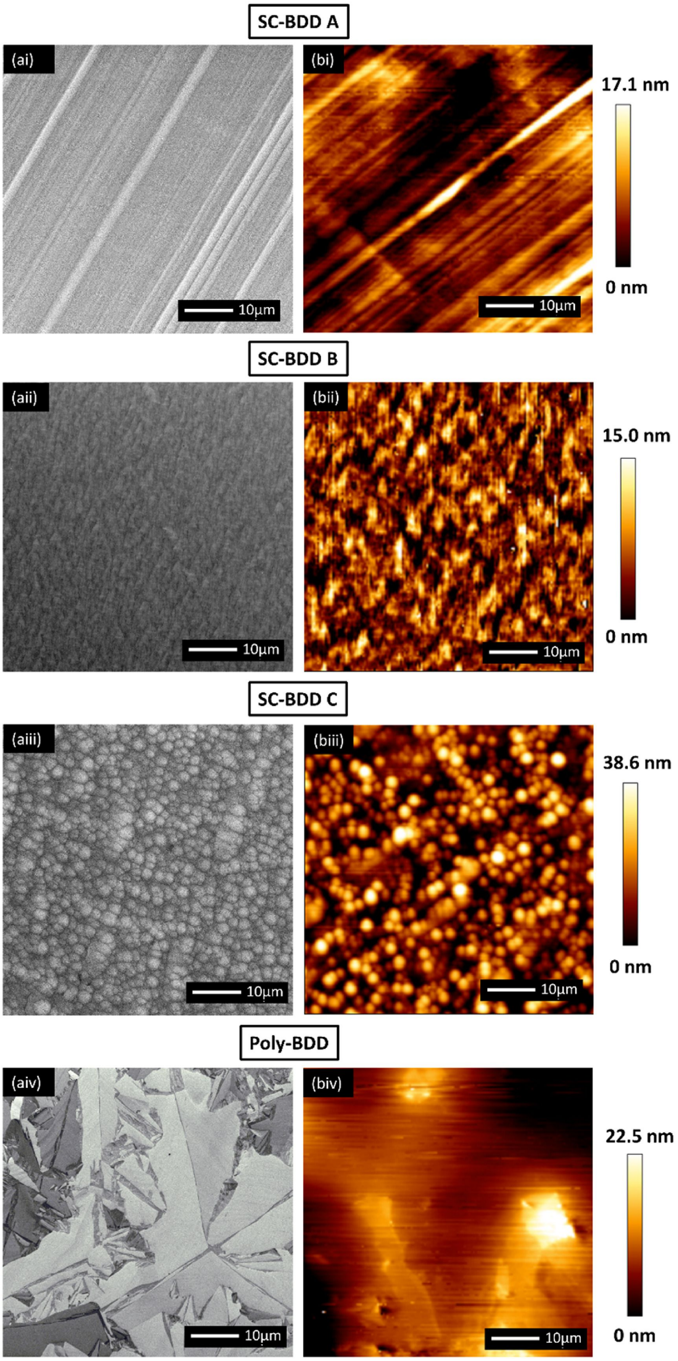

Figure 4.3: (a) SEM images and (b) AFM images visualizing surface morphology of (i) SC-BDD A, (ii) SC-BDD B, (iii) SC-BDD C, and (iv) poly-BDD electrodes.

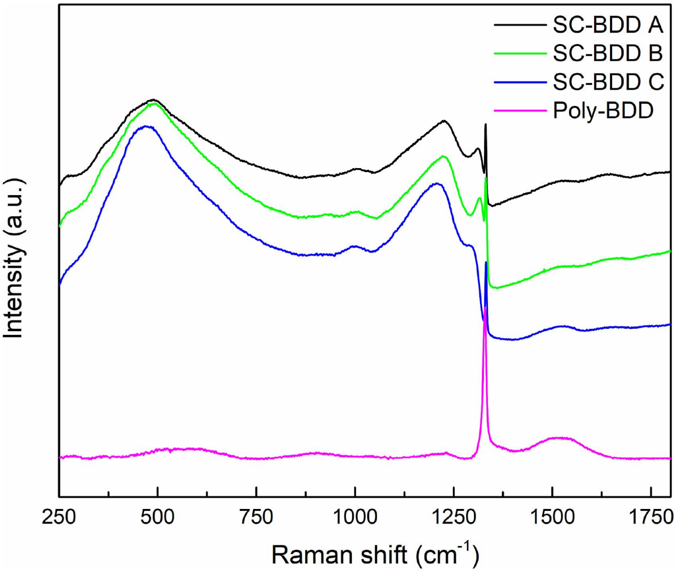

Figure 4.4: Raman spectra of (—) SC-BDD A, (—) SC-BDD B, (—) SC-BDD C, and (—) poly-BDD.

heteroepitaxial SC-BDD electrodes can be clearly distinguished in Fig. 4.3. Samples A and B possess similar absolute values in surface roughness; however, the characteristic features are completely different. On the SC-BDD A, the surface is dominated by polishing lines owing to the rough mechanical polishing of the top side of the heteroepitaxial diamond quasi-substrate. Between the polishing lines, the surface is very flat, indicating that growth is controlled by lateral step flow. On the other hand, the features identified on the SC-BDD B sample grown on the back surface close to the diamond nucleation layers apparently reflect the small angle grain boundary structure typical for heteroepitaxial diamond after several microns of growth. The on-axis SC-BDD C sample shows round hillocks, which are typical for 3D on-axis growth when the absence of an off-axis angle prevents an efficient step-flow growth mode. With a height of ~10 nm and a lateral dimension of ~1 μm, these hillocks are still quite flat (see Fig. 4.3(iii)). As expected, relatively large crystal facets with clearly visible grain boundaries can be observed on the poly-BDD surface, which demonstrates its heterogeneous nature resulting from the growth process. Nevertheless, the surface roughness of poly-BDD is comparable to the values obtained for SC-BDD samples due to the applied chemical-mechanical polishing.

Next, Raman spectroscopy was employed to assess the composition and quality of the BDD electrodes and to evaluate their boron content. The common feature of the recorded Raman spectra for all samples (displayed in Fig. 4.4) is the sharp diamond peak located at 1332 cm^{-1}. In addition, the Raman spectra recorded from the heteroepitaxial SC-BDD electrodes exhibit two strong features reflecting boron incorporation into the diamond lattice and indicating heavily doped diamond: (i) the intense broad band at around 480 cm^{-1} attributable to a combination of electronic Raman scattering and a Fano-shaped band [37], and (ii) the asymmetric band centred at ca 1200 cm^{-1} originat-

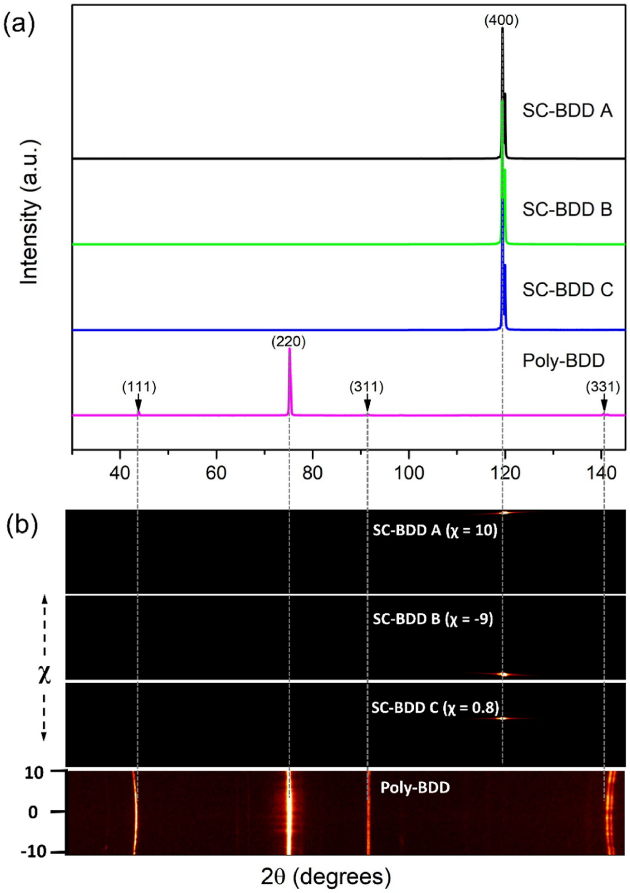

Figure 4.5: (a) XRD patterns of (—) SC-BDD A, (—) SC-BDD B, (—) SC-BDD C, and (—) poly-BDD. (b) 2D XRD images captured on all BDD samples.

ing from the phonon density of states [38]. Both characteristic peaks, however, are much less pronounced in the spectrum of poly-BDD, which also includes the G-band at 1580 cm^{-1} resulting from graphitic sp^2 carbon still present in the grain boundaries [39, 40], despite the acid and anodic oxidation treatments [41]. In contrast, the absence of the G-band peak in the Raman spectra of the heteroepitaxial SC-BDD samples indicates that the monocrystalline electrodes are largely free of sp^2 carbon impurities, and are thus of very high phase purity.

Moreover, the fitting tool [42], based on the analysis of the two Raman peaks located at ~1200 cm^{-1} and ~1332 cm^{-1}, was used for [B] determination. The assessed [B], overviewed in Table 4.1, ranges between $(2.5\text{–}4.4) \times 10^{21}$ cm^{-3} for the heteroepitaxial SC-BDD samples and proves their heavy boron doping level and metal-like character. For the poly-BDD electrode, [B] was calculated to be 1.8×10^{20} cm^{-3}, which correlates well with the value declared by the manufacturer (3×10^{20} cm^{-3} [33]).

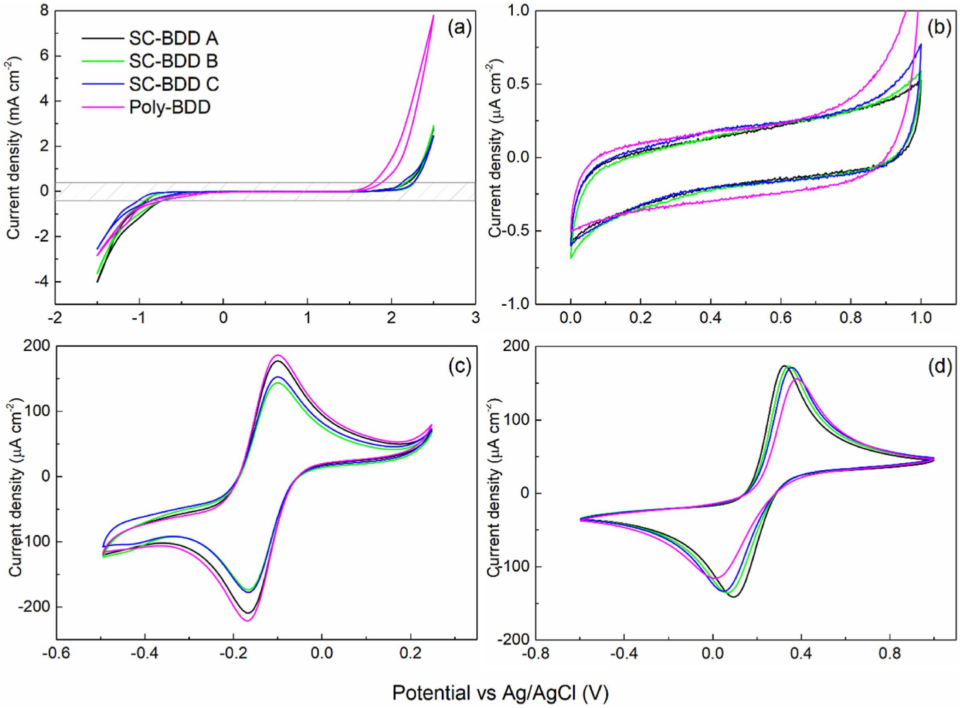

Figure 4.6: CVs recorded at a scan rate of 0.1 V s^{-1} on (━) SC-BDD A, (━) SC-BDD B, (━) SC-BDD C, and (━) poly-BDD in the following solutions: (a, b) 0.1 M KNO_3 in a range (a) from −1.5 V to +2.5 V, and (b) from 0 V to +1.0 V; (c) 1 mM $[Ru(NH_3)_6]^{3+/2+}$ in 0.1 M KNO_3, and (d) 1 mM $[Fe(CN)_6]^{3-/4-}$ in 0.1 M KNO_3.

The crystal plane orientations of the heteroepitaxially grown SC-BDD electrodes were studied using 2D XRD patterns, presented in Fig. 4.5. All SC-BDD samples show Bragg diffraction peaks corresponding to (400) diamond around $2\theta = 120°$ (peak separation due to CuKα_1 and CuKα_2), confirming their single crystal nature and (100) orientation. However, as Fig. 4.5(b) shows, only the spot from SC-BDD C is almost in the middle along χ, indicating its on-axis (100) orientation. On the other hand, the spots from SC-BDD A and SC-BDD B are shifted from the centre, which is ascribed to the fact that samples A and B were grown on 4° off-axis (100)-oriented quasi-substrates, and thus their surfaces are not exactly perpendicular to the (100) plane. The 2D image of poly-BDD shows rings, indicating individual crystals with various orientations, and thus confirming its polycrystalline character.

4.3.2. ELECTROCHEMICAL CHARACTERIZATION IN A SUPPORTING ELECTROLYTE

The width of the electrochemical potential window is a key property which determines the electrode's suitability and applicability for electrochemical sensing of a particular compound. Besides, both potential window and C_{dl} value provide valuable information about the surface condition of BDD electrodes, e.g., H- vs. O-termination [43] and sp^2 carbon presence [17]. For this reason, CV was performed in 0.1 M KNO_3 solution in the potential range from −1.5 to +2.5 V at a scan rate of 0.1 V s^{-1}, as shown in Fig. 4.6(a). Since nitrate (NO_3^-) reduction can only be achieved with a H-terminated BDD electrode [44] and all electrodes employed in this study were O-terminated, no interfering effects caused by the selected supporting electrolyte were recognized. The potential windows were assessed (reported in Table 4.1) between anodic and cathodic limiting potentials at which the current density exceeds a value of ±0.4 mA cm^{-2} indicating the onset of water decomposition [16, 17], leading to formation of oxygen and hydrogen gases in the anodic and cathodic region, respectively. In general, BDD-based materials in aqueous electrolyte solutions exhibit high overpotentials for oxygen and hydrogen evolution reactions, whose mechanisms are thoroughly described in Refs. [45, 46], which subsequently reflect in wide available potential ranges. This excellent property was also confirmed for all heteroepitaxial SC-BDD electrodes, which provided broad potential windows of ~ 3.3 V (see Table 4.1). Presumably, O-termination of the electrode surfaces contributed to this high value, as the expansion of solvent windows has been observed on O-terminated BDD electrodes [17, 34, 43], compared to H-terminated ones. As shown in Fig. 4.6(a), the width of the potential window of the poly-BDD electrode is reduced to 2.5 V, while the narrowing practically occurs only in the anodic region where oxygen develops. This behaviour is attributed to the heterogeneous character of the poly-BDD surface also containing sp^2 carbon impurities, whose presence was confirmed by Raman spectroscopy (see Fig. 4.4). The sp^2 sites possess increased catalytic activity facilitating the water electrolysis, thus causing the shift of the oxygen evolution reaction towards lower potential values [47].

Subsequently, CVs were recorded in the same medium (0.1 M KNO_3, at a scan rate of 0.1 V s^{-1}) but within shorter potential range from 0 V to +1.0 V where only background (non-faradaic) currents flow, as depicted in Fig. 4.6(b). Based on these measurements, C_{dl} values were estimated using Eq. (4.1) and are reported in Table 4.1. All studied electrodes provided low and comparable C_{dl} values ($< 5\ \mu$F cm^{-2}), which is in a good agreement with C_{dl} values obtained on O-terminated BDD electrodes in neutral media in previous studies [16, 46]. Besides, the C_{dl} of the BDD material indicates its quality: a high-quality BDD electrode typically provides a capacitance $< 10\ \mu$F cm^{-2} [17]. From observing Fig. 4.6(b) (and derived C_{dl} values), the newly fabricated heteroepitaxial SC-BDD electrodes can be considered of superior quality as compared to the high-quality poly-BDD. Also, lower C_{dl} values typically allow BDD electrodes to achieve lower detection limits toward selected analytes of interest. Therefore, combination of broad potential windows and low C_{dl} values implies promising potential and suitability of heteroepitaxial SC-BDD electrodes for electrochemical sensing.

To obtain information on the boron content present in the heteroepitaxially grown SC-BDD electrodes, the MS plots were recorded. The linear part of the MS plots, displayed in Fig. 4.2, was identified and its slope was used in the Mott-Schottky equation (Eq. (4.2)) to determine boron carrier concentration [B], which is tabulated for every electrode in Table 4.1. It should be noted that the Helmholtz capacitance is neglected in the applied Randles equivalent circuit because its correction does not affect the slope of the MS plot (and thus subsequent [B] estimation), and only causes a displacement of the flat band potential [24].

The MS analysis yielded similar [B] values of ~ 2×10^{21} cm^{-3} for all three SC-BDD samples confirming their heavy boron doping and high conductivity. For poly-BDD, one order of magnitude lower [B] of 2×10^{20} cm^{-3} was estimated; this value corresponds well with [B] of 3×10^{20} cm^{-3} declared by the manufacturer [33]. Importantly, [B] values assessed using MS analysis are highly comparable with those extracted from the recorded Raman spectra (see Table 4.1). In addition, several previous works confirmed that the MS analysis can be favourably used for heavily boron-doped diamond electrodes [24, 48] and gives reliable [B] values, which are similar to values obtained by Raman spectroscopy and neutron depth profiling [48].

4.3.3. ELECTROCHEMICAL CHARACTERIZATION WITH REDOX MARKERS

CV MEASUREMENTS

Electrochemical performance of the SC-BDD electrodes was further assessed, and compared to poly-BDD, using CV and two redox markers, $[Ru(NH_3)_6]^{3+/2+}$ and $[Fe(CN)_6]^{3-/4-}$ (both 1 mM in 0.1 M KNO_3); the recorded curves after iR compensation are presented in Fig. 4.6(c) and Fig. 4.6(d), respectively. All studied electrodes provided well-defined pairs of redox peaks for both markers. The most valuable parameter, i.e., the peak-to-peak separation (ΔE_p), serves as ET rate indicator and was determined from the measurements; the values are provided in Table 4.1. In general, $[Ru(NH_3)_6]^{3+/2+}$ is a representative of outer-sphere redox markers, which means that its redox reaction is controlled by simple diffusion and ET is not influenced by the electrode's surface characteristics such as surface termination, presence of sp^2 phase, and microstructure [49–52]. Importantly, $[Ru(NH_3)_6]^{3+/2+}$ due to its high sensitivity to the density of states [52] can be used as a probe to differentiate between 'metal-like' conductive (highly doped) and semi-conductive (lowly doped) BDD electrodes, as for the latter the ET kinetics of $[Ru(NH_3)_6]^{3+/2+}$ is significantly hindered [17]. On all SC-BDD electrodes, ΔE_p values for $[Ru(NH_3)_6]^{3+/2+}$ are similar and very close to 0.059 V (see Table 4.1), the value for a single-electron reversible system. This confirms a near-reversible behaviour and fast ET kinetics of this redox couple, and consequently high quality and high conductivity of the SC-BDD electrodes, which is in a good agreement with the Mott-Schottky analysis indicating heavy boron doping. As expected, variations in surface morphology between the individual SC-BDD samples and O-termination do not affect redox behaviour of $[Ru(NH_3)_6]^{3+/2+}$ due to its outer-sphere nature.

In contrast, the second utilised redox probe, $[Fe(CN)_6]^{3-/4-}$, exhibits inner-sphere character and its redox reaction, occurring through specific surface interactions, is strongly dependent on BDD surface properties, predominantly surface termination and boron doping level [46, 50–52]. Therefore, ET kinetics of $[Fe(CN)_6]^{3-/4-}$ is not significantly affected by sp^2-bonded carbon impurities [52, 53]. An increase in ΔE_p values (shown in Table 4.1) was observed on all SC-BDD and poly-BDD electrodes indicating slower ET kinetics of $[Fe(CN)_6]^{3-/4-}$ redox couple, compared to the outer-sphere probe, while the inhibition of ET can be ascribed to O-termination of the SC-BDD and poly-BDD electrodes [50, 51]. Our results correlate well with a prior study reporting that ET kinetics of $[Fe(CN)_6]^{3-/4-}$ is hindered even on highly doped but O-terminated BDD surfaces [23]. This behaviour can be attributed to the presence of oxygen-containing groups being able to block adsorption sites [49] and/or electrostatically interact with the anionic redox probe, as oxygen groups are often described as possessing partial negative charge ($C\delta^{+}$–$O\delta^{-}$) [50]. Such electrostatic interactions can also depend on the applied electrode potential, through its influence on the interfacial electric field and the structure of the electrical double layer. Furthermore, among all electrodes tested, the highest ΔE_p and thus the slowest kinetics along with a decrease in peak current density of $[Fe(CN)_6]^{3-/4-}$ (as shown in Fig. 4.6(d)) was observed on poly-BDD. Conversely, the fastest ET kinetics was recognized on the SC-BDD A electrode. Concerning only the SC-BDD electrodes, the rougher, on-axis sample C provided a higher ΔE_p value, compared to the smoother, 4° off-axis electrodes A and B.

In previous studies employing O-terminated (100), (110), and (111)-faceted monocrystalline diamond electrodes [14, 23], much larger ΔE_p values ranging between 0.24 V–1.83 V for $[Ru(NH_3)_6]^{3+/2+}$ and 0.45 V–2.7 V for $[Fe(CN)_6]^{3-/4-}$ were obtained (see Table 4.2), which reflect very, in some cases even extremely, sluggish ET kinetics. In comparison with the mentioned works [14, 23], herein reported heteroepitaxially grown SC-BDD electrodes with (100) orientation and O-termination demonstrated the best electrochemical performance. Such difference in electrochemical behaviour presumably arises from different dopant concentration and conductivity: the heteroepitaxially grown SC-BDD electrodes presented in this study possess high doping with [B] $\sim 2 \times 10^{21}$ cm^{-3} and thus high conductivity, while single crystal diamond electrodes used in Refs. [14, 23] were less doped by almost one order of magnitude (as can be seen in Table 4.2), which caused lower conductivity manifested by slower ET kinetics.

Table 4.2: Comparison of the peak-to-peak separation (ΔE_p) values for redox markers obtained on O-terminated SC-BDD electrodes of different orientation and boron concentration ([B]). Abbreviations: MS – Mott-Schottky analysis; SIMS – secondary-ion mass spectrometry.

Orientation	**[B] (cm^{-3})**	ΔE_p **(mV) $[Ru(NH_3)_6]^{3+/2+}$**	ΔE_p **(mV) $[Fe(CN)_6]^{3-/4-}$**	**Ref.**
(100)	$(2–3)\times10^{19}$ (MS)	no peaks	no peaks	[14]
(100)	4.2×10^{20} (SIMS)	1830	2700	[23]
(110)	1.3×10^{20} (MS)	240	555	[14]
(100)A	1.95×10^{21} (MS)	67	232	This work
(100)B	2.24×10^{21} (MS)	68	276	This work
(100)C	2.66×10^{21} (MS)	67	305	This work
(111)	$(5–7)\times10^{20}$ (MS)	240	450	[14]
(111)	3.8×10^{20} (SIMS)	870	1470	[23]

Finally, it needs to be emphasized that all heteroepitaxial SC-BDD electrodes provided comparable and highly satisfactory electrochemical performance, confirming their high quality as well as high conductivity. Apparently, the distinct variations in surface morphology presented, have only a minor effect on the behaviour of the SC-BDD electrodes.

SECM measurements

The electrochemical homogeneities of the heteroepitaxial SC-BDD and poly-BDD electrode surfaces were studied by SECM operating in a feedback mode (Fig. 4.7). SECM

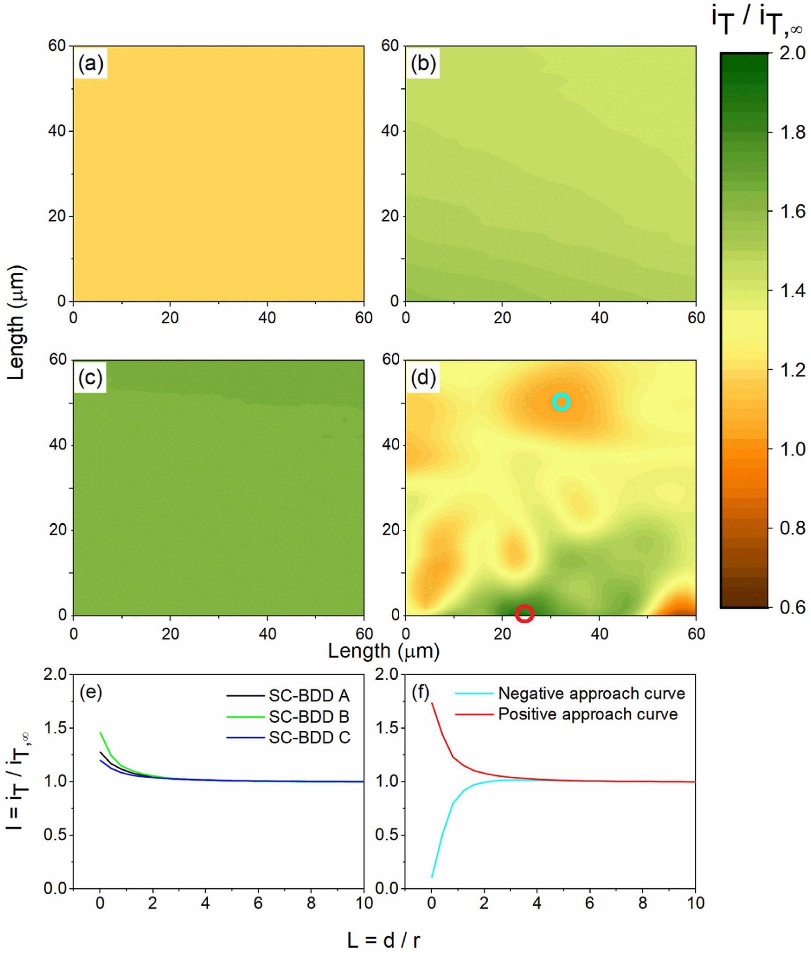

Figure 4.7: SECM images of (a) SC-BDD A, (b) SC-BDD B, (c) SC-BDD C, and (d) poly-BDD electrodes. All maps are scaled to a current window of 2.5 nA. The approach curves of (e) heteroepitaxial SC-BDD electrodes and (f) poly-BDD recorded at two different spots indicated by the cyan and red circles in (d).

maps of the samples were recorded by polarising the Pt probe tip at −0.4 V, which corresponds to the reduction potential of the selected mediator $[Ru(NH_3)_6]^{3+/2+}$. At the same time, the sample, i.e., a BDD electrode, was polarised at 0 V, which is the oxidation potential of the mediator in the case that the surface is active (conductive). The maps of the three heteroepitaxial SC-BDD samples showed similar behaviour. The current values measured at the probe are higher than the limiting current (in bulk solution), indicating that the surface electrodes are electrochemically active (conductive). In this case, with the proximity of the probe to the surface, the reduced mediator (Ru(III) → Ru(II)) at the tip can be oxidized back to Ru(III) at the substrate. The approach curve measurements also confirm the conductive nature of the SC-BDD surfaces. The curves were obtained by locating the probe at different random surface spots. The resulting curves showed a response consistent with positive feedback, in which the current increased when the probe approached the surface due to the regeneration of the redox mediator (Ru(III)). These can be seen in the selected approach curves shown in Fig. 4.7(e). In the case of the sample SC-BDD B, the map (Fig. 4.7(b)) showed a slight variation in current from top right to bottom left. This can be related to the tilt of the sample when placed in the electrochemical cell. This tilt causes a small change in the tip-substrate distance across the scanned area, resulting in a current variation. Nevertheless, the sample B clearly shows an electrochemically active response.

On the other hand, the poly-BDD electrode presented a different behaviour. The SECM map (Fig. 4.7(d)) showed a heterogeneous distribution of currents, with locations showing enhanced and suppressed feedback responses. The latter is associated with current values lower than the limiting current. Such suppressed currents do not necessarily indicate electrically insulating behaviour, but rather reflect hindered electron-transfer kinetics and limited mediator regeneration at the substrate. In this case, the signal is influenced by the proximity of the substrate and the limited availability of the redox mediator. These heterogeneities cannot be associated with the topology of the surface. From the AFM analysis, it was estimated that the roughness of the surface is in the nanometer range (see Table 4.1). For the SECM, the resolution is at the micrometer range, with a tip-substrate distance of $\sim 20\ \mu$m. Hence, nanometric topological variations of the surface are out of the detection range of the probe.

Interestingly, localised current variations observed in the SECM map match with the distinctive dimension and distribution of the diamond grains shown in Fig. 4.3(iv). The grains present different electrochemical nature in terms of local electron-transfer activity. This heterogeneity is likely attributed to the different boron incorporation efficiency of various crystal orientations [13, 15, 54, 55]. To further confirm the heterogeneous nature of those locations, approach curves were measured at two selected spots as indicated in the SECM map of Fig. 4.7(d) (cyan and red circles). Approach curves closer to positive and negative feedback limits, respectively, can be observed in the curves displayed in Fig. 4.7(f), confirming regions of enhanced and strongly suppressed electrochemical activity at those locations.

4.3.4. VOLTAMMETRIC BEHAVIOUR OF DOPAMINE ON HETEROEPITAXIAL SC-BDD ELECTRODES

To verify the applicability of fabricated SC-BDD electrodes for electrochemical sensing, CV experiments were performed with a commonly detected compound, dopamine (1 mM; in a 1 M phosphate buffered saline (PBS) of pH 7.4) of well-described redox behaviour [56]. Measured voltammetric curves, including the one recorded on poly-BDD for comparison, are displayed in Fig. 4.8 and the parameters gained from the experiments are provided in Table 4.1. CV curves recorded on all the electrodes display a quasi-reversible redox system as two peaks can be identified in the selected potential range from −0.2 V to +0.9 V. The anodic peak ($E_{\mathrm{pA,\,DA}}$) appearing at a potential higher than +0.6 V corresponds to the dopamine oxidation to dopamine-o-quinone, while the cathodic peak developed at ~ 0 V arises from the reduction of dopamine-o-quinone back to dopamine; both reactions involve the exchange of two electrons and two pro-

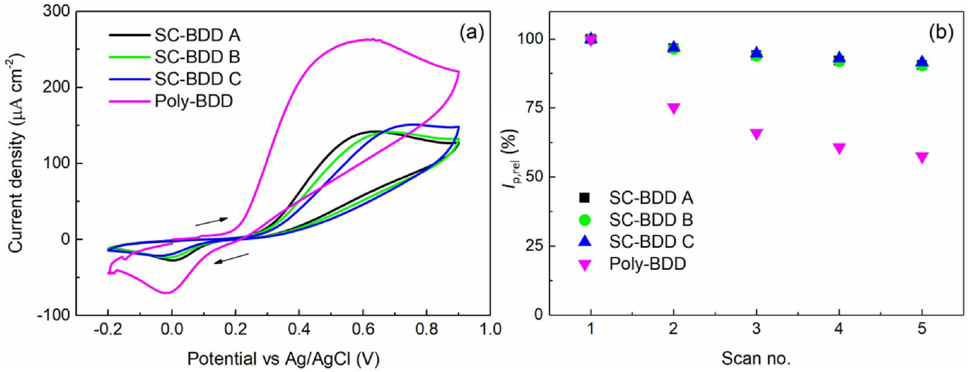

Figure 4.8: (a) CVs recorded in a solution of 1 mM dopamine in a pH 7.4 PBS (1 M) at a scan rate of 0.1 V s^{-1} on (—) SC-BDD A, (—) SC-BDD B, (—) SC-BDD C, and (—) poly-BDD. (b) Relative peak heights of 1 mM dopamine in a pH 7.4 PBS (1 M) assessed from five consecutive CV scans recorded on SC-BDD and poly-BDD electrodes.

tons in a selected pH 7.4 buffer [56]. Overall, comparable electrochemical responses of dopamine were recorded on the SC-BDD electrodes; however, slight variations can be identified (see Table 4.1). The highest $E_{\text{pA, DA}}$ was registered on the “on-axis” sample C with a rougher surface consisting of hillock-like features, which appear to have a hindering effect on the dopamine oxidation reaction. In contrast, smaller $E_{\text{pA, DA}}$ was recorded on the smoother “off-axis” samples A and B.

Dopamine, due to its inner-sphere ET [52, 57], is sensitive to the chemical composition of BDD electrode surfaces, i.e., termination (H- vs. O-) [43, 57–59] and sp^3/sp^2 ratio [57, 60, 61]. Herein obtained $E_{\text{pA, DA}}$ and large ΔE_p agree well with the values reported for dopamine on O-terminated BDD surfaces in previous studies carried out in the PBS media of pH 7.0–7.4 [58, 62, 63]. Generally, dopamine oxidation is hindered on oxidized diamond electrodes, manifested by a shift in $E_{\text{pA, DA}}$ to more positive values in comparison with H-terminated BDD [43, 58, 59]. As further shown in Fig. 4.8(a), the SC-BDD electrodes provide anodic peaks of similar current densities, while on poly-BDD the dopamine peak height is almost twice that intense. Such an increase in the voltammetric signal of dopamine can be attributed to the heterogeneous nature of the poly-BDD surface also containing grain boundaries where sp^2 carbon typically resides (the presence of sp^2 impurities is derived from the Raman spectrum in Fig. 4.4). The sp^2 sites may act as spots for dopamine adsorption [20, 57], facilitate its redox reaction and contribute to the increased currents.

Another significant difference between the SC-BDD and poly-BDD samples emerged when consecutive CV scans of dopamine were recorded, as is clearly visible in Fig. 4.8(b) and Fig. 4.9. A more pronounced decrease in both anodic and cathodic peak current densities occurred on poly-BDD; specifically, the oxidation peak current lowered by ~ 42% within five consecutive scans due to the surface fouling by oxidation product(s), which blocks electroactive sites on the electrode [56, 64]. In contrast, a much smaller decrease in peak heights of the dopamine/dopamine-o-quinone redox pair was recognized on the SC-BDD electrodes: the variation in anodic peak height ($I_{\text{pA, DA}}$) between the first and fifth scan was less than 14%. This clearly indicates enhanced resistance of

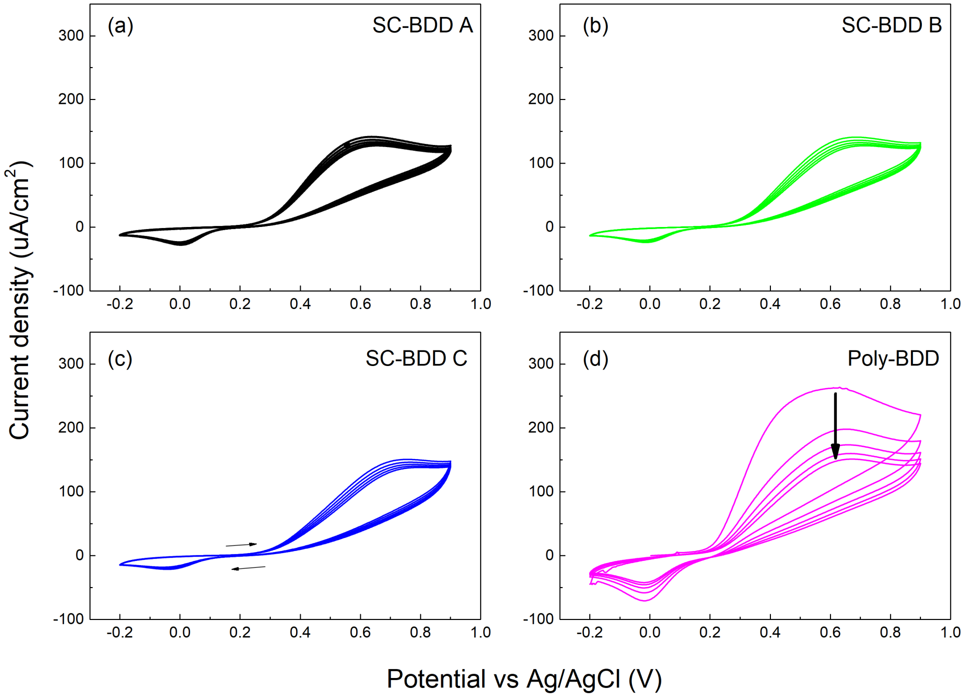

Figure 4.9: Five consecutive CV scans recorded at a scan rate of 0.1 V s^{-1} in 1 mM dopamine in a pH 7.4 PBS (1 M) on (—) SC-BDD A, (—) SC-BDD B, (—) SC-BDD C, and (—) poly-BDD.

heteroepitaxially grown SC-BDD samples towards electrode fouling.

Importantly, implementation of a simple stirring of the analysed dopamine solution (0.10 mM) between the individual CV scans (n = 10), acquired on freshly re-oxidized SC-BDD and poly-BDD electrodes, resulted in satisfactory repeatability, expressed by relative standard deviation (RSD) of the anodic peak heights of less than 2.6% for all four tested electrodes. Then, the same set of experiments was conducted two more times in 5-day intervals and RSD from all measurements (n = 30 in total) was evaluated to be 4.2% for SC-BDD A, 4.8% for SC-BDD B, 2.9% for SC-BDD C, and 4.0% for poly-BDD. Such RSD values reveal excellent stability of the recorded dopamine signals and indicate suitability of the SC-BDD electrodes for sensing applications.

Table 4.3: Analytical parameters of dopamine concentration dependences recorded by DPV in 10 mM PBS (pH 7.4) on BDD-based electrodes, including calculated LOD and LOQ values.

Electrode	**Linear range** (μ**mol L**$^{-1}$)	**Intercept** $\times 10^{-2}$ (μ**A cm**$^{-2}$)	**Slope** $\times 10^{-2}$ (μ**A** μ**M**$^{-1}$ **cm**$^{-2}$)	**R**	**LOD** (μ**mol L**$^{-1}$)	**LOQ** (μ**mol L**$^{-1}$)
SC-BDD A	0.25–100.0	-1.66 ± 0.41	12.25 ± 0.01	0.9998	0.10	0.33
Poly-BDD	0.50–75.0	-1.93 ± 0.35	5.47 ± 0.07	0.9995	0.19	0.65

Next, a more sensitive voltammetric technique, DPV, was employed to record concentration dependences of dopamine in 10 mM PBS of pH 7.4 on the SC-BDD A, and

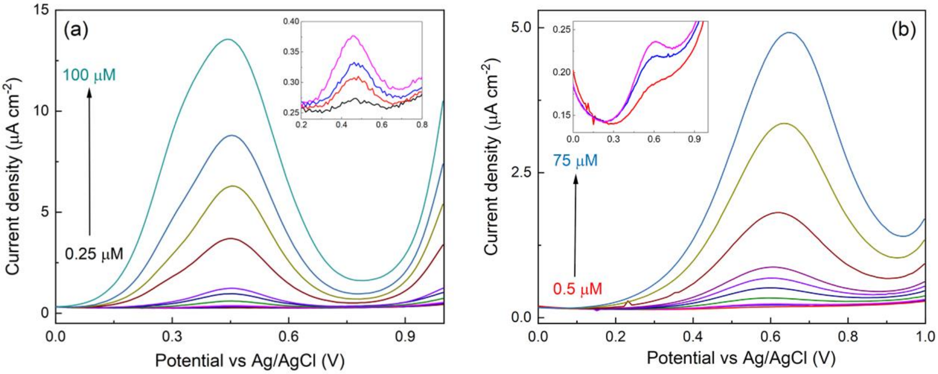

Figure 4.10: DP voltammograms of dopamine at various concentration levels in 10 mM PBS of pH 7.4 recorded on oxidized (a) heteroepitaxial SC-BDD A and (b) poly-BDD electrodes. Insets show details of voltammetric peaks recorded for the lowest dopamine concentrations (0.25 μM, 0.50 μM, 0.75 μM, 1.00 μM).

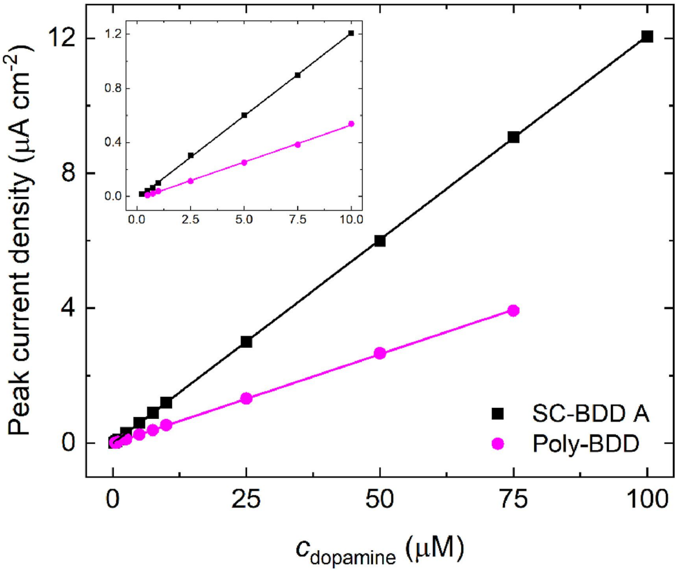

Figure 4.11: Concentration dependences of dopamine recorded by DPV on oxidized SC-BDD A and poly-BDD electrodes. Inset shows details of dependences for lower concentrations.

for comparison purposes, also on the poly-BDD sample; the linear DP voltammetric responses for both electrodes are depicted in Fig. 4.10. Sample A was selected as a representative of heteroepitaxial SC-BDD because it manifested better electrochemical characteristics in the preceding measurements (see Table 4.1). Concentration dependences are plotted in Fig. 4.11 and the obtained analytical parameters along with calculated LOD and LOQ are summarized in Table 4.3. Clearly, the heteroepitaxial SC-BDD A electrode outperformed conventionally used poly-BDD because it demonstrated wider

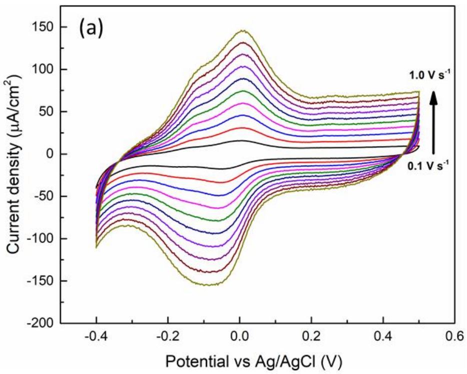

Figure 4.12: CVs recorded on GCE in 0.1 M $HClO_4$ at different scan rates after experiments with 1 mM AQDS and subsequent thorough rinsing with deionized water. (b) Comparison of CVs recorded in 0.1 M $HClO_4$ at a scan rate of 0.1 V s^{-1} on (—) SC-BDD A, (—) SC-BDD B, (—) SC-BDD C, and (—) poly-BDD, and (—) GCE after experiments with 1 mM AQDS and subsequent thorough rinsing with deionized water.

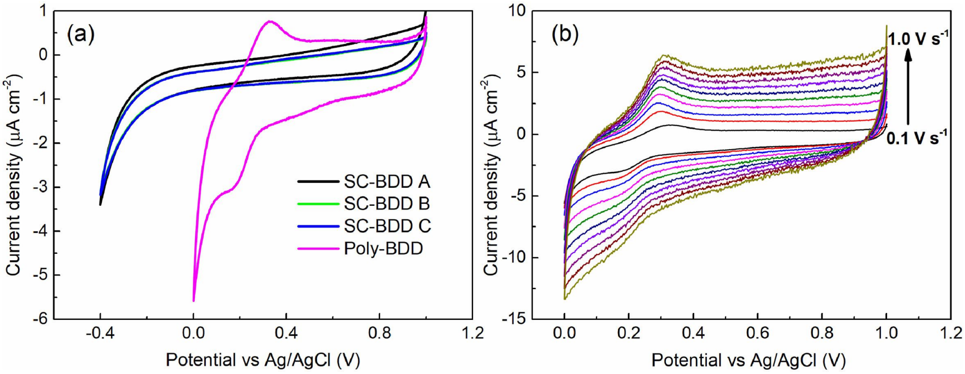

Figure 4.13: CVs recorded in 0.1 M $HClO_4$ after experiments with 1 mM AQDS and subsequent thorough rinsing with deionized water: (a) on (—) SC-BDD A, (—) SC-BDD B, (—) SC-BDD C, and (—) poly-BDD, and (b) on poly-BDD at different scan rates ranging from 0.1 to 1.0 V s^{-1} in increments of 0.1 V s^{-1}.

linear range, enhanced sensitivity and lower LOD and LOQ values. This comparison further supports the suitability and applicability of the newly developed heteroepitaxial SC-BDD electrodes for electroanalysis and sensor development.

4.3.5. Adsorption behaviour of AQDS

To further explore the anti-fouling property of heteroepitaxial SC-BDD electrodes, measurements were performed with AQDS, which can serve as an “adsorption marker”. AQDS is well-known for its high adsorption ability, predominantly towards metallic and sp^2 carbon electrodes [65, 66]; for the latter it was verified also in this study during experiments with AQDS on glassy carbon electrode (GCE; see Fig. 4.12).

In CVs of the SC-BDD electrodes (see Fig. 4.13(a)), only background currents were recorded in the potential range from −0.4 V to +1.0 V. Thus, no peaks were registered. On the poly-BDD, however, a couple of small and broad peaks can be recognized at potentials of +0.15 V and +0.25 V, which are ascribed to the quasi-reversible redox reaction of adsorbed AQDS [65]. Besides, a scan rate study was performed, during which the current densities of both peaks increased linearly with an increase in the scan rate, as can be seen in Fig. 4.13(b). This confirms that the AQDS reaction on poly-BDD is adsorption-controlled. CVs recorded on GCE, shown in Fig. 4.12, revealed much more intense symmetrical peaks with ΔE_p approaching 0 V, which correspond to the redox reaction of AQDS and reveal characteristic features of a surface-confined redox analyte. Similarly to the poly-BDD, the scan rate study proved that the AQDS reaction on GCE surface is controlled by adsorption. This correlates very well with the previously published works reporting the same observation for AQDS reaction on GCE [66].

In a previous study [66], the electrode surface chemistry was identified as the main factor responsible for AQDS adsorption. Polar surfaces containing oxygen functionalities are significantly more prone to adsorption through strong dipole-dipole and ion-dipole interactions, which can be formed between AQDS molecules and the oxidized surfaces. Nevertheless, all four electrodes used in this study and subjected to experiments with AQDS were oxidized, and thus polar oxygen-containing groups were introduced on their surfaces. Interestingly, the heteroepitaxial SC-BDD electrodes in their O-terminated state showed resistance towards AQDS adsorption despite their polar and hydrophilic character. This indicates that another factor, presumably the complex heterogeneous nature of the poly-BDD surface with grain boundaries, sp^2 carbon and growth defects, weakens the diamond electrode ability to resist adsorption. Moreover, a similar observation was made in Ref. [22] where a (111)-oriented SC-BDD electrode showed a lower tendency for adsorption than mechanically polished polycrystalline BDD; the absence of defects and sp^2 carbon impurities on the single-crystal diamond surface was identified as the main factor contributing to the resistance towards adsorption.

All in all, heteroepitaxial SC-BDD represents a very attractive electrode material with suitable electrochemical performance and excellent anti-fouling characteristics resulting in improved response stability. Consequently, SC-BDD certainly has the potential and ability to replace and even outperform conventional poly-BDD, particularly in applications where low susceptibility towards (bio)fouling is extremely important, e.g., for *in-vitro* and *in-vivo* sensing [64].

4.4. CONCLUSION

In the present study, a highly promising concept of heteroepitaxial growth for the preparation of large-area, heavily doped (100)-faceted SC-BDD electrodes has been successfully demonstrated. Three fabricated SC-BDD samples were subjected to detailed surface analysis and electrochemical characterization, and their properties were compared to the conventional poly-BDD.

2D XRD images confirmed the single crystal nature and the orientation of SC-BDD samples, while SEM and AFM micrographs visualized variations in the surface morphology. Absence of sp^2 carbon impurities along with heavy doping ($[B] > 10^{21}$ cm^{-3}) of the heteroepitaxial SC-BDD electrodes was demonstrated by Raman spectroscopy and

MS analysis, respectively. Highly conductive, 'metal-like' nature of the SC-BDD electrodes was further confirmed by CV experiments with $[Ru(NH_3)_6]^{3+/2+}$ probe manifesting near-reversible redox response and almost ideal ΔE_p (0.067 V) approaching 0.059 V. In addition to the fast ET kinetics, wide potential windows (~3.3 V) and low C_{dl} values (<4 μF cm^{-2}) confirmed superior quality, compared to poly-BDD, and excellent electrochemical characteristics of the newly developed SC-BDD electrodes. Only CV experiments with surface-sensitive $[Fe(CN)_6]^{3-/4-}$ and dopamine/dopamine-o-quinone redox systems demonstrated minor impact of the morphological features, dislocation density, and small off-cut angle on the electrochemical behaviour of SC-BDD. Nevertheless, small variations could still be identified: Interestingly, the rougher, "on-axis" sample C provided higher ΔE_p values, indicating slower ET kinetics, for both tested inner-sphere markers, while smaller ΔE_p were recorded on the smoother 4° "off-axis" samples A and B. As a result, the heteroepitaxial SC-BDD A sample was further subjected to DPV recording of dopamine concentration dependence and exhibited more satisfactory analytical parameters (wider linear range, enhanced sensitivity, and lower LOD and LOQ values) than conventional poly-BDD electrode. In addition, the anti-fouling property of all SC-BDD electrodes was clearly demonstrated during experiments with dopamine and AQDS probe.

As a result, the overall electrochemical performance of the heteroepitaxial SC-BDD samples is relatively consistent across the different samples tested. This electrode material seems to be very attractive for electrochemical sensing, particularly in applications requiring strong resistance towards fouling and adsorption effects, manifesting by stable and reliable electrochemical responses; among such applications belong, e.g., continuous monitoring of biomarkers and pharmaceuticals, *in-vitro* and *in-vivo* sensing. Moreover, heteroepitaxial SC-BDD certainly demonstrated a potential to outperform and replace conventional poly-BDD, suffering from its inherent heterogeneous and defective nature with sp^2 carbon impurities residing in the grain boundaries and often being responsible for deteriorated electrochemical performance, which can manifest by, e.g., increased susceptibility towards adsorption and fouling effects.

Finally, heteroepitaxy-based approach enables the synthesis of high surface area SC-BDD electrodes, which could lead to much broader use of SC-BDD not only in electroanalysis, but also in other electrochemical fields, e.g., waste-water treatment via advanced oxidation processes, electrosynthesis, and electrocatalysis, for which scaling up is crucial. All in all, the heteroepitaxial SC-BDD offers possibilities that neither homoepitaxial single-crystal nor polycrystalline BDD electrodes have, i.e., scalability (including large area) combined with controlled and well-defined surface orientation.

BIBLIOGRAPHY

[1] N. J. Yang, S. Y. Yu, J. V. Macpherson, Y. Einaga, H. Y. Zhao, G. H. Zhao, G. M. Swain, and X. Jiang, "Conductive diamond: synthesis, properties, and electrochemical applications", Chemical Society Reviews **48**, 157–204 (2019).

[2] S. Baluchova, A. Danhel, H. Dejmkova, V. Ostatna, M. Fojta, and K. Schwarzova-Peckova, "Recent progress in the applications of boron doped diamond electrodes

in electroanalysis of organic compounds and biomolecules - a review", Analytica Chimica Acta **1077**, 30–66 (2019).

[3]M. Yence, A. Cetinkaya, G. Ozcelikay, S. I. Kaya, and S. A. Ozkan, "Boron-doped diamond electrodes: recent developments and advances in view of electrochemical drug sensors", Crit. Rev. Anal. Chem. **2021**, 17.

[4]Y. P. He, H. B. Lin, Z. C. Guo, W. L. Zhang, H. D. Li, and W. M. Huang, "Recent developments and advances in boron-doped diamond electrodes for electrochemical oxidation of organic pollutants", Separ. Purif. Technol. **212**, 802–821 (2019).

[5]O. M. Cornejo, M. F. Murrieta, L. F. Castaneda, and J. L. Nava, "Characterization of the reaction environment in flow reactors fitted with BDD electrodes for use in electrochemical advanced oxidation processes: a critical review", Electrochim. Acta **331**, 14 (2020).

[6]D. S. Babu, J. M. C. Mol, and J. G. Buijnsters, "Experimental insights into anodic oxidation of hexafluoropropylene oxide dimer acid (GenX) on boron-doped diamond anodes", Chemosphere **288**, 10 (2022).

[7]R. C. P. Oliveira, J. G. Buijnsters, M. M. Mateus, J. C. M. Bordado, and D. M. F. Santos, "On the electrooxidation of kraft black liquor on boron-doped diamond", J. Electroanal. Chem. **909**, 116151 (2022).

[8]S. Lips and S. R. Waldvogel, "Use of boron-doped diamond electrodes in electroorganic synthesis", Chemelectrochem **6**, 1649–1660 (2019).

[9]C. Y. Guo, J. G. Zheng, H. W. Deng, P. H. Shi, and G. H. Zhao, "Photoelectrocatalytic interface of boron-doped diamond: modification, functionalization and environmental applications", Carbon **175**, 454–466 (2021).

[10]S. Y. Yu, N. J. Yang, S. T. Liu, and X. Jiang, "Diamond supercapacitors: progress and perspectives", Curr. Opin. Solid State Mater. Sci. **25**, 13 (2021).

[11]D. J. Garrett, W. Tong, D. A. Simpson, and H. Meffin, "Diamond for neural interfacing: a review", Carbon **102**, 437–454 (2016).

[12]P. A. Nistor and P. W. May, "Diamond thin films: giving biomedical applications a new shine", J. R. Soc. Interface **14**, 15 (2017).

[13]G. Janssen, W. J. P. van Enckevort, W. Vollenberg, and L. J. Giling, "Characterization of single-crystal diamond grown by chemical vapour deposition processes", Diam. Relat. Mater. **1**, 789–800 (1992).

[14]Y. V. Pleskov, Y. E. Evstefeeva, M. D. Krotova, V. P. Varnin, and I. G. Teremetskaya, "Synthetic semiconductor diamond electrodes: electrochemical behaviour of homoepitaxial boron-doped films orientated as (111), (110), and (100) faces", J. Electroanal. Chem. **595**, 168–174 (2006).

[15]N. R. Wilson, S. L. Clewes, M. E. Newton, P. R. Unwin, and J. V. Macpherson, "Impact of grain-dependent boron uptake on the electrochemical and electrical properties of polycrystalline boron doped diamond electrodes", J. Phys. Chem. B **110**, 5639–5646 (2006).

[16] L. A. Hutton, J. G. Iacobini, E. Bitziou, R. B. Channon, M. E. Newton, and J. V. Macpherson, “Examination of the factors affecting the electrochemical performance of oxygen-terminated polycrystalline boron-doped diamond electrodes”, Analytical Chemistry **85**, 7230–7240 (2013).

[17] J. V. Macpherson, “A practical guide to using boron doped diamond in electrochemical research”, Phys. Chem. Chem. Phys. **17**, 2935–2949 (2015).

[18] J. Ryl, A. Zielinski, R. Bogdanowicz, and K. Darowicki, “Heterogeneous distribution of surface electrochemical activity in polycrystalline highly boron-doped diamond electrodes under deep anodic polarization”, Electrochem. Commun. **83**, 41–45 (2017).

[19] T. Watanabe, S. Yoshioka, T. Yamamoto, H. Sepehri-Amin, T. Ohkubo, S. Matsumura, and Y. Einaga, “The local structure in heavily boron-doped diamond and the effect this has on its electrochemical properties”, Carbon **137**, 333–342 (2018).

[20] S. Garcia-Segura, E. Vieira dos Santos, and C. A. Martínez-Huitle, “Role of sp^3/sp^2 ratio on the electrocatalytic properties of boron-doped diamond electrodes: a mini review”, Electrochem. Commun. **59**, 52–55 (2015).

[21] R. Ramesham, “Cyclic voltammetric response of boron-doped homoepitaxially grown single crystal and polycrystalline CVD diamond”, Sens. Actuator B-Chem. **50**, 131–139 (1998).

[22] T. Kondo, Y. Einaga, B. V. Sarada, T. N. Rao, D. A. Tryk, and A. Fujishima, “Homoepitaxial single-crystal boron-doped diamond electrodes for electroanalysis”, J. Electrochem. Soc. **149**, E179–E184 (2002).

[23] T. A. Ivandini, T. Watanabe, T. Matsui, Y. Ootani, S. Iizuka, R. Toyoshima, H. Kodama, H. Kondoh, Y. Tateyama, and Y. Einaga, “Influence of surface orientation on electrochemical properties of boron-doped diamond”, J. Phys. Chem. C **123**, 5336–5344 (2019).

[24] L. Kavan, Z. V. Zivcova, V. Petrak, O. Frank, P. Janda, H. Tarabkova, M. Nesladek, and V. Mortet, “Boron-doped diamond electrodes: electrochemical, atomic force microscopy and raman study towards corrosion-modifications at nanoscale”, Electrochim. Acta **179**, 626–636 (2015).

[25] A. Taylor, S. Baluchová, L. Fekete, L. Klimša, J. Kopeček, D. Šimek, M. Vondráček, L. Míka, J. Fischer, K. Schwarzová-Pecková, and V. Mortet, “Growth and comparison of high-quality MW PECVD grown B doped diamond layers on 118, 115 and 113 single crystal diamond substrates”, Diam. Relat. Mater. **123**, 108815 (2022).

[26] A. Tallaire, A. Valentin, V. Mille, L. William, M. A. Pinault-Thaury, F. Jomard, J. Barjon, and J. Achard, “Growth of thick and heavily boron-doped (113)-oriented CVD diamond films”, Diam. Relat. Mater. **66**, 61–66 (2016).

[27] J.-C. Arnault, S. Saada, and V. Ralchenko, “Chemical vapor deposition single-crystal diamond: a review”, Phys. Status Solidi RRL **16**, 2100354 (2022).

[28] M. Schreck, S. Gsell, R. Brescia, and M. Fischer, “Ion bombardment induced buried lateral growth: the key mechanism for the synthesis of single crystal diamond wafers”, Sci. Rep. **7**, 44462 (2017).

[29] A. F. Sartori, M. Fischer, S. Gsell, and M. Schreck, “In situ boron doping during heteroepitaxial growth of diamond on ir/ysz/si”, Phys. Status Solidi Appl. Mater. Sci. **209**, 1643–1650 (2012).

[30] A. F. Sartori, “Heteroepitaxial boron-doped diamond: from synthesis to application”, PhD thesis (Universität Augsburg, Augsburg, Germany, 2016), p. 235.

[31] M. Mayr, M. Fischer, O. Klein, S. Gsell, and M. Schreck, “Interaction between surface structures and threading dislocations during epitaxial diamond growth”, Phys. Status Solidi **212**, 2480–2486 (2015).

[32] C. Stehl, M. Fischer, S. Gsell, E. Berdermann, M. Rahman, M. Traeger, O. Klein, and M. Schreck, “Efficiency of dislocation density reduction during heteroepitaxial growth of diamond for detector applications”, Appl. Phys. Lett. **103**, 151905 (2013).

[33] Element Six, *Element six diafilm™ ep datasheet*, `https://e6cvd.com/media/catalog/category/Element_Six_Diafilm_EP_datasheet_Final.pdf`, Accessed: 2025-02-21, n.d.

[34] F. B. Liu, J. D. Wang, B. Liu, X. M. Li, and D. R. Chen, “Effect of electronic structures on electrochemical behaviors of surface-terminated boron-doped diamond film electrodes”, Diam. Relat. Mater. **16**, 454–460 (2007).

[35] S. Ghodbane, D. Ballutaud, F. Omnès, and C. Agnès, “Comparison of the XPS spectra from homoepitaxial 111, 100 and polycrystalline boron-doped diamond films”, Diam. Relat. Mater. **19**, 630–636 (2010).

[36] A. F. Azevedo, M. R. Baldan, and N. G. Ferreira, “Doping level influence on chemical surface of diamond electrodes”, J. Phys. Chem. Solid. **74**, 599–604 (2013).

[37] V. Mortet, I. Gregora, A. Taylor, N. Lambert, P. Ashcheulov, Z. Gedeonova, and P. Hubik, “New perspectives for heavily boron-doped diamond Raman spectrum analysis”, Carbon **168**, 319–327 (2020).

[38] V. A. Sidorov and E. A. Ekimov, “Superconductivity in diamond”, Diam. Relat. Mater. **19**, 351–357 (2010).

[39] A. Merlen, J. G. Buijnsters, and C. Pardanaud, “A guide to and review of the use of multiwavelength Raman spectroscopy for characterizing defective aromatic carbon solids: from graphene to amorphous carbons”, Coatings **7**, 153 (2017).

[40] A. F. Sartori, S. Orlando, A. Bellucci, D. M. Trucchi, S. Abrahami, T. Boehme, T. Hantschel, W. Vandervorst, and J. G. Buijnsters, “Laser-induced periodic surface structures (LIPSS) on heavily boron-doped diamond for electrode applications”, ACS Appl. Mater. Interfaces **10**, 43236–43251 (2018).

[41] S. J. Cobb, F. H. J. Laidlaw, G. West, G. Wood, M. E. Newton, R. Beanland, and J. V. Macpherson, “Assessment of acid and thermal oxidation treatments for removing sp^2 bonded carbon from the surface of boron doped diamond”, Carbon **167**, 1–10 (2020).

[42] Determination of boron concentration in diamond from Raman spectroscopy, Online Raman analysis tool available at https://ramantool.pythonanywhere.com/ (accessed 21-02-2025).

[43] M. Brycht, S. Baluchová, A. Taylor, V. Mortet, S. Sedláková, L. Klimša, J. Kopeček, and K. Schwarzová-Pecková, "Comparison of electrochemical performance of various boron-doped diamond electrodes: dopamine sensing in biomimicking media used for cell cultivation", Bioelectrochemistry **137**, 107646 (2021).

[44] P. Kuang, K. Natsui, C. Feng, and Y. Einaga, "Electrochemical reduction of nitrate on boron-doped diamond electrodes: effects of surface termination and boron-doping level", Chemosphere **251**, 126364 (2020).

[45] H. B. Suffredini, S. A. S. Machado, and L. A. Avaca, "The water decomposition reactions on boron-doped diamond electrodes", J. Braz. Chem. Soc. **15**, 16–21 (2004).

[46] K. Schwarzová-Pecková, J. Vosáhlová, J. Barek, I. Šloufová, E. Pavlova, V. Petrák, and J. Zavázalová, "Influence of boron content on the morphological, spectral, and electroanalytical characteristics of anodically oxidized boron-doped diamond electrodes", Electrochim. Acta **243**, 170–182 (2017).

[47] I. Duo, A. Fujishima, and C. H. Comninellis, "Electron transfer kinetics on composite diamond (sp^3)-graphite (sp^2) electrodes", Electrochem. Commun. **5**, 695–700 (2003).

[48] Z. Živcová, V. Petrák, O. Frank, and L. Kavan, "Electrochemical impedance spectroscopy of polycrystalline boron doped diamond layers with hydrogen and oxygen terminated surface", Diam. Relat. Mater. **55**, 70–76 (2015).

[49] M. C. Granger and G. M. Swain, "The influence of surface interactions on the reversibility of ferri/ferrocyanide at boron-doped diamond thin-film electrodes", J. Electrochem. Soc. **146**, 4551–4558 (1999).

[50] I. Yagi, H. Notsu, T. Kondo, D. A. Tryk, and A. Fujishima, "Electrochemical selectivity for redox systems at oxygen-terminated diamond electrodes", J. Electroanal. Chem. **473**, 173–178 (1999).

[51] M. C. Granger, M. Witek, J. Xu, J. Wang, M. Hupert, A. Hanks, M. D. Koppang, J. E. Butler, G. Lucazeau, M. Mermoux, J. W. Strojek, and G. M. Swain, "Standard electrochemical behavior of high-quality, boron-doped polycrystalline diamond thin-film electrodes", Anal. Chem. **72**, 3793–3804 (2000).

[52] J. A. Bennett, J. Wang, Y. Show, and G. M. Swain, "Effect of sp2-bonded nondiamond carbon impurity on the response of boron-doped polycrystalline diamond thin-film electrodes", J. Electrochem. Soc. **151**, E306 (2004).

[53] Y. Einaga, J. S. Foord, and G. M. Swain, "Diamond electrodes: diversity and maturity", MRS Bull. **39**, 525–532 (2014).

[54] T. Ando, K. Asai, J. Macpherson, Y. Einaga, T. Fukuma, and Y. Takahashi, "Nanoscale reactivity mapping of a single-crystal boron-doped diamond particle", Anal. Chem. **93**, 5831–5838 (2021).

[55] Z. Liu, S. Baluchová, Z. Li, Y. Gonzalez-Garcia, C. E. Hall, and J. G. Buijnsters, "Unravelling microstructure-electroactivity relationships in free-standing polycrystalline boron-doped diamond: a mapping study", Acta Mater. **266**, 119671 (2024).

[56] A. N. Patel, S.-Y. Tan, T. S. Miller, J. V. Macpherson, and P. R. Unwin, "Comparison and reappraisal of carbon electrodes for the voltammetric detection of dopamine", Anal. Chem. **85**, 11755–11764 (2013).

[57] T. Watanabe, Y. Honda, K. Kanda, and Y. Einaga, “Tailored design of boron-doped diamond electrodes for various electrochemical applications with boron-doping level and sp^2-bonded carbon impurities”, Phys. Status Solidi **211**, 2709–2717 (2014).

[58] R. Trouillon, Y. Einaga, and M. A. M. Gijs, “Cathodic pretreatment improves the resistance of boron-doped diamond electrodes to dopamine fouling”, Electrochem. Commun. **47**, 92–95 (2014).

[59] L. Y. Jiang, G. W. Nelson, J. Abda, and J. S. Foord, “Novel modifications to carbon-based electrodes to improve the electrochemical detection of dopamine”, ACS Appl. Mater. Interfaces **8**, 28338–28348 (2016).

[60] P. S. Siew, K. P. Loh, W. C. Poh, and H. Zhang, “Biosensing properties of nanocrystalline diamond film grown on polycrystalline diamond electrodes”, Diam. Relat. Mater. **14**, 426–431 (2005).

[61] S. Baluchová, A. Taylor, V. Mortet, S. Sedláková, L. Klimša, J. Kopeček, O. Hák, and K. Schwarzová-Pecková, “Porous boron doped diamond for dopamine sensing: effect of boron doping level on morphology and electrochemical performance”, Electrochim. Acta **327**, 135025 (2019).

[62] M. Wei, Z. Y. Xie, L. G. Sun, and Z. Z. Gu, “Electrochemical properties of a boron-doped diamond electrode modified with gold/polyelectrolyte hollow spheres”, Electroanalysis **21**, 138–143 (2009).

[63] M. Wei, C. Terashima, M. Lv, A. Fujishima, and Z. Z. Gu, “Boron-doped diamond nanograss array for electrochemical sensors”, Chem. Commun., 3624–3626 (2009).

[64] Z. Deng, R. Zhu, L. Ma, K. Zhou, Z. Yu, and Q. Wei, “Diamond for antifouling applications: a review”, Carbon **196**, 923–939 (2022).

[65] I. Shpilevaya and J. S. Foord, “Electrochemistry of methyl viologen and anthraquinonedisulfonate at diamond and diamond powder electrodes: the influence of surface chemistry”, Electroanalysis **26**, 2088–2099 (2014).

[66] J. Xu, Q. Chen, and G. M. Swain, “Anthraquinonedisulfonate electrochemistry: a comparison of glassy carbon, hydrogenated glassy carbon, highly oriented pyrolytic graphite, and diamond electrodes”, Anal. Chem. **70**, 3146–3154 (1998).

5

5

INKJET PRINTING-MANUFACTURED BORON-DOPED DIAMOND CHIP ELECTRODES FOR ELECTROCHEMICAL SENSING PURPOSES

This work introduces a simple, cost-effective bottom-up method for fabricating patterned boron-doped diamond (BDD) three-electrode sensor chips using inkjet printing. Diamond nanoparticles were deposited on silicon substrates via a commercial research inkjet printer with piezo-driven printheads. After drying, the substrate underwent chemical vapor deposition to grow a uniform thin-film BDD layer serving as working and counter electrodes, while silver inkjet printing completed the reference electrode. The sensor successfully detected various organic compounds, including glucose, dopamine, and tyrosine, outperforming commercial screen-printed BDD electrodes. This approach enables rapid prototyping of small-scale BDD electrode designs with enhanced sensor performance and reusability.

The contents of this chapter have been published in:

- Z. Liu, S. Baluchová, B. Brocken, E. Ahmed, P. Pobedinskas, K. Haenen, and J. G. Buijnsters, "Inkjet printing-manufactured boron-doped diamond chip electrodes for electrochemical sensing purposes," *ACS Applied Materials & Interfaces* **15**(33), 39915–39925 (2023). DOI:10.1021/acsami.3c04824

5.1. INTRODUCTION

Diamond, owing to its extreme mechanical hardness, chemical inertness, exceptional biocompatibility, wide band gap (5.5 eV), high electrical resistivity, and thermal conductivity [1, 2], is a highly attractive and multifunctional material. Diamond's still-increasing popularity is demonstrated by its widespread application fields, including synthetic gemstones, mechanical tools, and integration within thermal, optical, electronic, biomedical, and quantum devices [2–4]. Importantly, the electrical properties of diamond can be modified, therefore one of the nature's best insulators can be turned into (semi-)conductive material when doped with boron, making it valuable for electrochemistry and (bio)sensor development [1, 5, 6]. Conductive boron-doped diamond (BDD) preserves the features of intrinsic diamond and additionally possesses a wide working potential window, low background and capacitive currents, low noise, and resistance toward corrosion and passivation [1, 5], which results in a powerful electrode material. These properties ensure highly favorable sensing performance of BDD, e.g., in clinical [7], environmental [8], and food [9] analysis, however, the extreme mechanical hardness makes processing and structuring of (doped) diamond a challenging task.

Fabrication of patterned BDD structures in a straightforward and inexpensive way is required for a variety of practical applications including the development of BDD-based electrochemical sensors. In general, the patterning can be carried out by either post-growth processing (top-down approach) or pre-growth selective seeding (bottom-up approach), however, the former often includes expensive, resource-demanding, and time-consuming lithographic [10], etching [11, 12], or laser micromachining [13] facilities placed in cleanrooms. The combination of photolithography and reactive ion etching was used by Sugitani et al. to fabricate the BDD microchip for single-drop analysis [12]. In contrast, pre-growth nanodiamond seeding covers more straightforward and cost-effective methodologies, including template-assisted [14, 15] and various printing-based approaches [16–24]. Direct printing dominates over templated methods as a need for a template, its prior preparation, and/or subsequent removal is excluded. In general, a nucleation layer of diamond nanoparticles can be selectively seeded on a supporting substrate using printing-based techniques and then inserted into a chemical vapor deposition (CVD) chamber to grow the desired diamond structures. In particular, Zhuang et al. [16] and Vandenryt et al. [17] used poly(dimethylsiloxane) as a stamp for microcontact printing to create patterned, nanodiamond-seeded areas on a silicon substrate, while a microprinting technique, developed by Taylor et al., utilized a computer-driven micropipette filled with a mixture composed of nanodiamond particles, water, and glycerol for controlled seeding and diamond structuring [18].

Various nanodiamond ink formulations have also been utilized in seeding approaches based on inkjet printing [20–24] where ink microdroplets are ejected and positioned in a contactless manner on a selected substrate through a micrometric nozzle. The pioneering efforts concerning inkjet printing of diamond suspensions were made predominantly by Fox et al. [20] and Chen et al. [21, 22] who verified the proof-of-concept and demonstrated diamond patterning in the form of lines. Later, inkjet-printed nanocrystalline diamond resonators [23] and diamond gas sensors for NH_3 and NO_2 detection [24] were successfully fabricated.

Inkjet printing becomes increasingly popular in the area of development of electrochemical sensors as demonstrated by several recent reviews [25–27]. However, to date, inkjet printing of nanodiamonds has not yet been exploited in the fabrication of BDD structures and sensors. Notably, inkjet printing is a completely digital technique, which allows for an unprecedented freedom of precise electrode print designs and their alterations with a negligible cost impact. This is in contrast to the dominant, well-established screen-printing technique demanding stencils to achieve desired patterning. Concerning BDD-based electrodes, the screen printing of ink consisting of BDD powder mixed with an insulating polyester resin binder was successfully pioneered by Kondo and coworkers [28–32].

In this work, we describe for the first time a simplified, bottom-up fabrication approach for a BDD-based sensor chip relaying on selective-area seeding via utilization of direct inkjet printing of nanodiamond particles. The whole seeding process, accomplished by a commercial research inkjet printer, was systematically optimized and thorough attention was paid to (i) the composition of in-house developed diamond ink, (ii) pre-treatment of the substrate surface, and (iii) printing parameters. Subsequently, the inkjet-seeded substrate was subjected to a CVD growth step to obtain a miniaturized thin-film BDD working electrode (WE) and counter electrode (CE). Following, silver ink was inkjet-printed onto the substrate to complete the three-electrode sensor chip with a reliable reference electrode (RE). Finally, the electrochemical performance of the newly developed, chip-based BDD electrodes towards redox markers and structurally different organic molecules, including glucose, ascorbic acid, uric acid, dopamine, and tyrosine, was examined and subsequently compared to the performance of commercially available “screen-printed” BDD electrodes.

5.2. EXPERIMENTAL

5.2.1. INK-JET PRINTING OF NANODIAMOND SEED PATTERNS

The PIXDRO LP-50 inkjet printer and DMC-11610 cartridges were employed for the selective printing of diamond nanoparticles. This printer employs piezo-driven drop-on-demand print-heads allowing control over the printing process with high resolution. The DMC print-head was equipped with 16 nozzles that can be individually controlled. All prints in this work were performed with only one active nozzle. The diameter of the nozzle is approximately 21 μm, which is much larger than the used nanodiamond particles (4.4 ± 0.7 nm, as declared by the manufacturer).

Nanodiamond ink was prepared by diluting 5.0% (wt/vol) nanodiamond colloid (NanoCarbon Research Institute, Japan) with deionized water and glycerol with a volume ratio of 1:1, reaching the final nanodiamond concentration of 0.4% (wt/vol). Diamond nanoparticles were well dispersed with a desirable viscosity (6 mPa·s as measured with Anton Paar rheometer MCR302) and remained stable over a long period of time (more than 6 months). While not in use, the cartridge was stored in the fridge at 5 °C.

Pristine (100) silicon or silicon/silicon dioxide (300 nm thermal SiO_2 dry/wet/dry layer) wafers with a 4 in. diameter, thickness of 525 ± 25 μm, and resistivity of 10^3–10^5 Ω cm were purchased from MicroChemicals (Germany). Substrates were subjected to oxy-

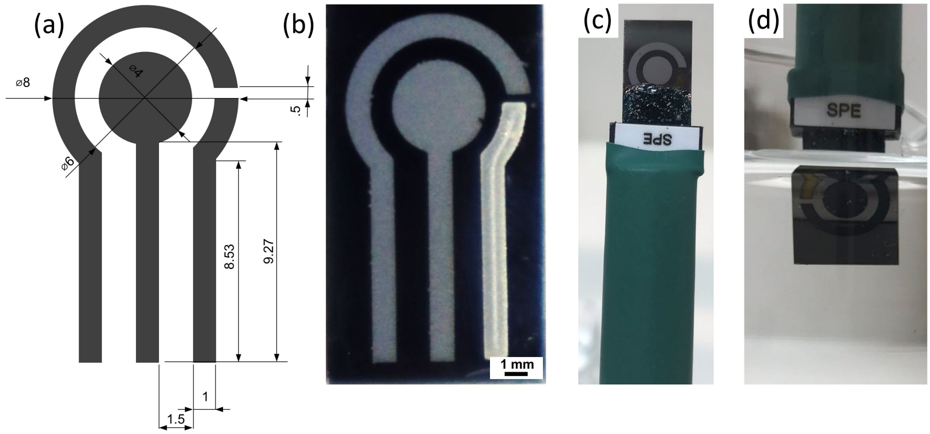

Figure 5.1: (a) The used print design (dimensions in mm) for the fabrication of the inkjet-printed BDD chip. (b) Optical image of the complete chip with the BDD grown layers functioning as a working (middle) and counter (left) electrode and with a silver-printed reference electrode (right). (c) Inkjet-printed BDD chip with dielectric layer inserted into the measuring cable. (d) Visualization of the electrochemical measurement with the newly fabricated chip immersed into analyzed solution.

gen plasma treatment to increase the hydrophilicity of their surfaces (2 min at 20 W using a Diener Femto plasma setup) and subsequently exposed to air. To examine the hydrophilicity and wettability of the substrate surface, contact angle measurements were performed using a Theta lite optical tension meter (Biolin Scientific) with an ink drop volume of 3 μL. Upon contact of the ink droplet with the substrate surface, a digital camera recorded the contact angle during the first 10 s at a 17 Hz frequency.

The print design for the inkjet-printed chip developed in this work, depicted in Fig. 5.1(a), was inspired by commercially available screen-printed electrodes (produced by, e.g., Metrohm DropSens). The piezo-actuated nozzle was driven under a voltage of −38 V with a 1 kHz printing frequency, and the ink pressure was −10 mbar. The substrate was fixed on a stage by a vacuum chuck, and the printhead, whose temperature was maintained at 29 °C, was placed 1 mm above it. The printhead printed along the X-axis with a typical resolution of 750 drops per inch (DPI) with a droplet diameter of 26 μm and a volume of 9 pL. Printing time for one set of patterns for the WE and CE was 2.5 min. After printing, the wafer with printed, nanodiamond ink-containing patterns was placed in a Binder VD23 vacuum oven to evaporate the solvents at 65 °C for 30 min.

5.2.2. THREE-ELECTRODE BDD CHIP FINALIZATION

The selective growth of miniaturized, thin-film BDD electrodes was carried out in an ASTeX 6500 series microwave plasma enhanced CVD reactor (MW-PE-CVD) using a CH_4/H_2/trimethyl boron (TMB) plasma, with corresponding gas flows of 5/395/100 sccm, which resulted in a 1% CH_4 concentration and a B/C ratio of 20 000 ppm (TMB gas was diluted to 1000 ppm in H_2). The following deposition conditions were set: a microwave power of 3500 W, working pressure of 30 Torr (~40 mbar), deposition temperature of >500 °C (monitored by a hand-held single wavelength pyrometer in the peak measuring mode with the emissivity set to 0.6), and growth time of 14 h. The grown BDD layers functioned as both the WE and CE.

Commercial Metalon silver ink (JS-B25P, NovaCentrix) of 25 wt% silver nanoparticles (~75 nm) was used to print the RE to finalize the three-electrode chip. The piezo-actuated nozzle was driven under a voltage of 26 V with a 1 kHz printing frequency; other conditions were identical to those used for nanodiamond ink printing. In order to ensure sufficient conductivity, the silver RE consisted of five repeatedly printed layers, while each layer took 1 min to print. After baking on a hot plate for 5 min at 100 °C, the inkjet-printed BDD chip (depicted in Fig. 5.1(b)) was prepared for further analysis and sensing. The whole three-electrode fabrication process is visualized in Fig. 5.2. Notably, the complete procedure can be principally conducted within 1 working day. Printing of nanodiamond ink and the RE takes only a few minutes, while the most “time-consuming” process is the BDD layer growth; however, the duration of this step is also dependent on the desired thickness of the deposited thin film and CVD reactor specifications.

5.2.3. SURFACE CHARACTERIZATION OF BDD CHIP

The optical images were taken by a Keyence VHX-600 digital microscope. The nucleation density after inkjet printing of diamond nanoparticles, the surface morphology of the subsequently grown BDD layer as well as the morphology of the BDD working electrode in the commercial screen-printed chip (used as benchmark electrochemical sensor) were examined using a scanning electron microscope JEOL JSM6500F in a secondary electron imaging mode operated at 15 keV. Surface roughness and thickness of the grown BDD layer on the inkjet-printed chip were assessed based on AFM measurements performed with a Nanite AFM in tapping mode with silicon tips over a scanned area of $50 \times 50\ \mu m^2$. Raman spectra were recorded with a Horiba LabRAM HR set-up equipped with an argon-ion laser operating at 514 nm wavelength.

5.2.4. ELECTROCHEMICAL MEASUREMENTS WITH BDD CHIP

All electrochemical measurements were performed at laboratory temperature (23 ± 1 °C) using an Autolab PGSTAT128N equipped with the FRA module and controlled by Nova 2.1 software (Metrohm, The Netherlands). The inkjet-printed BDD chips or the commercially obtained ones (BDD10 with ceramic substrate from Metrohm DropSens) were connected to the potentiostat with a cable connector (Ref. CAC, Metrohm DropSens, The Netherlands). Prior to measurements, a layer of a lab-made insulating and acid-resistant lacquer was applied on the inkjet-printed BDD chip (see Fig. 5.1(c)) to define the exposed geometric area of the WE (A_{geom} of 14 mm^2). Subsequently, after drying, the chip was immersed in the measuring solution as depicted in Fig. 5.1(d). DropSens electrode chips consisted of CVD-grown BDD working electrodes (A_{geom} of 9.6 mm^2) and screen-printed carbon and silver electrodes, which functioned as CE and RE, respectively. Both inkjet-printed and commercially obtained chips were used in their as-prepared (as-obtained) state, thus no intentional pre-treatment was applied prior to the measurements reported in this chapter. All reported potential values are referred to the

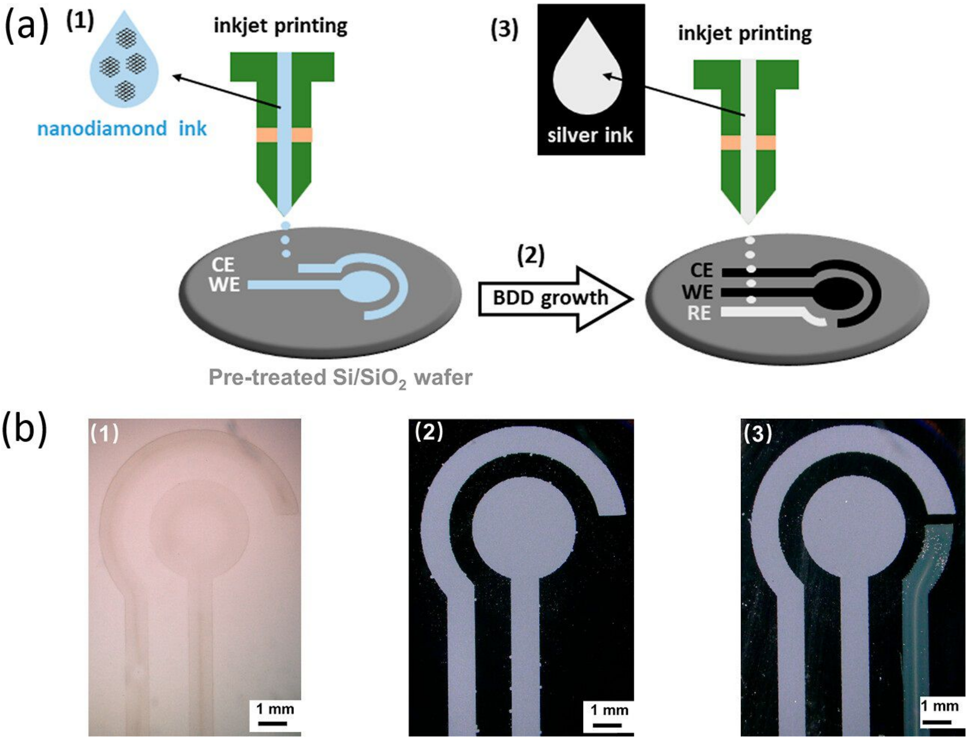

Figure 5.2: (a)Schematically illustrated fabrication steps for the inkjet-printed BDD-based three-electrode sensor chip: (1) Pretreated Si or Si/SiO_2 wafer was used as a substrate for inkjet printing of nanodiamond ink according to a digital design to create patterns for the WE and CE. (2) After drying, the wafer with selectively seeded areas was placed into a MW-PE-CVD chamber to conduct the growth of a homogeneous BDD layer. (3) Lastly, the chip was completed with the inkjet-printed silver RE. (b) Optical images showing the result of each fabrication step (1)-(3) included in the schematic.

silver (Ag) electrode and current densities are related to A_{geom} of the BDD working electrodes.

CV curves were recorded from lower to higher potential values and backward, typically using a scan rate v of 0.10 V s^{-1}, if not stated otherwise, for the following solutions: supporting electrolytes (0.5 M KNO_3, 0.1 M H_2SO_4, 0.1 M NaOH, 10 mM phosphate buffered saline of pH 7.4), redox markers $[Ru(NH_3)_6]^{3+/2+}$ and $[Fe(CN)_6]^{3-/4-}$ (both 1 mM in 0.5 M KNO_3), organic analytes dopamine, tyrosine (both 100 μM in 10 mM phosphate buffered saline of pH 7.4), glucose, uric acid (both 1 mM in 0.1 M NaOH), and ascorbic acid (1 mM in 0.1 M H_2SO_4). Moreover, CVs obtained in a 0.5 M KNO_3 solution in the potential range from 0 V to +0.5 V were used to estimate double-layer capacitance (C_{dl}) values using the following equation (Eq. 5.1):

$$C_{\mathrm{dl}} = \frac{\Delta I_{\mathrm{AV}}}{A_{\mathrm{geom}}\, v} \tag{5.1}$$

where ΔI_{AV} stands for the average background current difference (in A) between the forward and backward scan at a potential of +0.25 V, A_{geom} is the geometric surface area of the BDD working electrode (0.14 cm^2), and v is the scan rate (0.10 V s^{-1}). The effective surface area (A_{eff}) of BDD working electrodes of inkjet-printed and commercial chips was evaluated from CVs recorded in 1 mM $[\text{Ru}(\text{NH}_3)_6]^{3+/2+}$ in 0.5 M KNO_3 at different scan rates v ranging from 0.01 to 0.25 V s^{-1}, using the Randles-Sevcik equation for a reversible redox process (Eq. 5.2):

$$I_p = (2.69 \times 10^5)\, n^{3/2} D^{1/2} A_{\text{eff}} v^{1/2} c^0 \tag{5.2}$$

where I_p is the peak current (in A), n is the number of transported electrons (i.e., 1), D is the diffusion coefficient of the redox marker (7.3×10^{-6} cm^2 s^{-1}), and c^0 is its concentration (1 μmol cm^{-3}).

Impedance spectra were recorded for 1 mM $[\text{Fe}(\text{CN})_6]^{3-/4-}$ in 0.5 M KNO_3 using the formal potential of the redox probe (+0.175 V). An AC signal with a 10 mV amplitude and a 10^5 Hz–0.1 Hz frequency range was employed in the measurements. Then, the acquired EIS spectra were fitted with the Randles equivalent circuit to obtain constant phase element (CPE) and charge transfer resistance (R_{CT}) values.

5.2.5. CHEMICALS

All analytical grade chemicals were obtained from Merck and used as-received: dopamine hydrochloride (≥98 %), L-ascorbic acid (≥99 %), uric acid (≥99 %), L-tyrosine (≥98 %), D-glucose (≥99.5 %), hexaammineruthenium(III) chloride (≥98 %), potassium hexacyanoferrate(II) trihydrate (≥98.5 %), potassium nitrate (≥99.0 %), sulfuric acid (95–98 %), phosphate buffered saline (tablets, 10 mM, pH 7.4), sodium hydroxide (≥97 %, pellets), glycerol (≥99 %), triethylene glycol monoethyl ether (≥95 %). Ultra-filtrated deionized water with a resistivity of 18.0 MΩ cm (LWTN Genie A system, Laboratorium Water Technologie Nederland) was used to prepare all aqueous solutions.

5.3. RESULTS AND DISCUSSION

5.3.1. DIAMOND INK FORMULATION

In general, the properties of the inkjet ink determine important aspects affecting the droplet formation during the printing process, such as consistent jetting, uniform jetting velocity and trajectory, and the presence or absence of satellite droplets. For this reason, highly specific rheological features of the inkjet printing inks, e.g., viscosity and surface tension in a range of 1–30 mPa s and 25–40 mN m^{-1}, respectively, are required [25, 33]. Accordingly, two types of inks differing in composition were initially prepared, the first based on a mixture of glycerol and deionized water (in a ratio of 1:1) with 0.4 % (w/v) diamond nanoparticles and the second containing a single liquid, triethylene glycol monoethyl ether, with 0.2 % (w/v) diamond nanoparticles. Both inks met all requirements for printing (the measured viscosity was 6 and 8 mPa s, respectively). To attain a homogeneous growth of the diamond films, high-density and uniform seeding is essential [34], which is realized through well-dispersed suspensions. Hence, the ink stability and nanoparticle dispersion were among the first factors investigated. Importantly, no indication of instability through agglomeration and sedimentation of nanoparticles in the glycerol-containing ink was detected. In contrast, diamond nanoparticles in triethylene glycol monoethyl ether started to precipitate after a short time, which eventually led to the phase separation. Therefore, water/glycerol diamond ink was selected as optimal and used in all subsequent experiments. In addition, glycerol decreases the evaporation rate of water, thus prevents fast ink evaporation and the so-called "coffee-stain" effect, i.e., irregular distribution of nanoparticles oriented toward the edges of printed patterns [18].

5.3.2. SUBSTRATE PRE-TREATMENT

Direct printing of optimized water/glycerol ink on a pristine Si-based substrate resulted in the formation of individual, circular-shaped droplets with a diameter of ~47 μm and a high contact angle of ~55°, as depicted in Fig. 5.3(ai) and 5.3(bi), respectively. When 1000 DPI was tested for printing the patterns on a pristine substrate, the individual droplets overlapped and merged into larger drops, which is visualized in Fig. 5.3(ci). Apparently, the pristine Si-based substrate does not have sufficient surface energy to be fully wetted by the inkjet liquid. On one hand, higher contact angle possibly increases the printing resolution, but on the other hand, reduced wetting limits the spreading of the liquid film and prevents the formation of continuous ink layers, which are desired. Therefore, the substrate was subjected to a 2 min long oxygen plasma treatment to increase its hydrophilicity and wettability. This resulted in complete wetting of the substrate's surface manifested by "droplet spilling" and a decrease in the contact angle below 4°, as shown in Fig. 5.3(aii) and 5.3(bii). In addition, the "over-wetting" of the substrate caused feathering at the droplet as well as pattern edge boundaries, which, as visualized in Fig. 5.3(cii), considerably reduced the resolution. Then, the oxygen plasma-treated substrates were simply left in air for a few hours. Such air exposure partially suppressed the hydrophilic nature of the substrate, which manifested by printing a spherical droplet of a larger diameter of ~63 μm [Fig. 5.3(aiii)] with a contact angle of ~23° [Fig. 5.3(biii)]. These droplet parameters were proven to be optimal for the formation of uniform prints with clear and sharp edges using 750 DPI, as demonstrated in Fig. 5.3(ciii).

5.3.3. PRINTING PARAMETERS AND POST-PRINTING PROCESSING

The diamond ink printing was done in a single run; i.e., multiple passes through the same areas were omitted. The printhead temperature was maintained at 29 °C, which slightly decreased the viscosity of the diamond ink and ensured a more consistent print. Using optimized ink formulation and substrate treatment, a DPI value of 750 satisfactorily minimized the spacing between the individual droplets and enabled their overlapping, which subsequently resulted in formation of thin continuous lines of the designed patterns. After inkjet printing of the diamond ink, the drying step was performed to achieve only nanodiamond-containing seeding areas in desired patterns. The boiling point of glycerol at atmospheric pressure is 290 °C, however, such high temperature could chemically modify (oxidize) the diamond nanoparticles and alter their properties [18]. Therefore, the solvents, water and glycerol, were carefully evaporated in a vacuum oven, which enabled the complete drying of the printed patterns at 65 °C. An optical image of the chip after drying is shown in image (b1) in Fig. 5.2. The latter il-

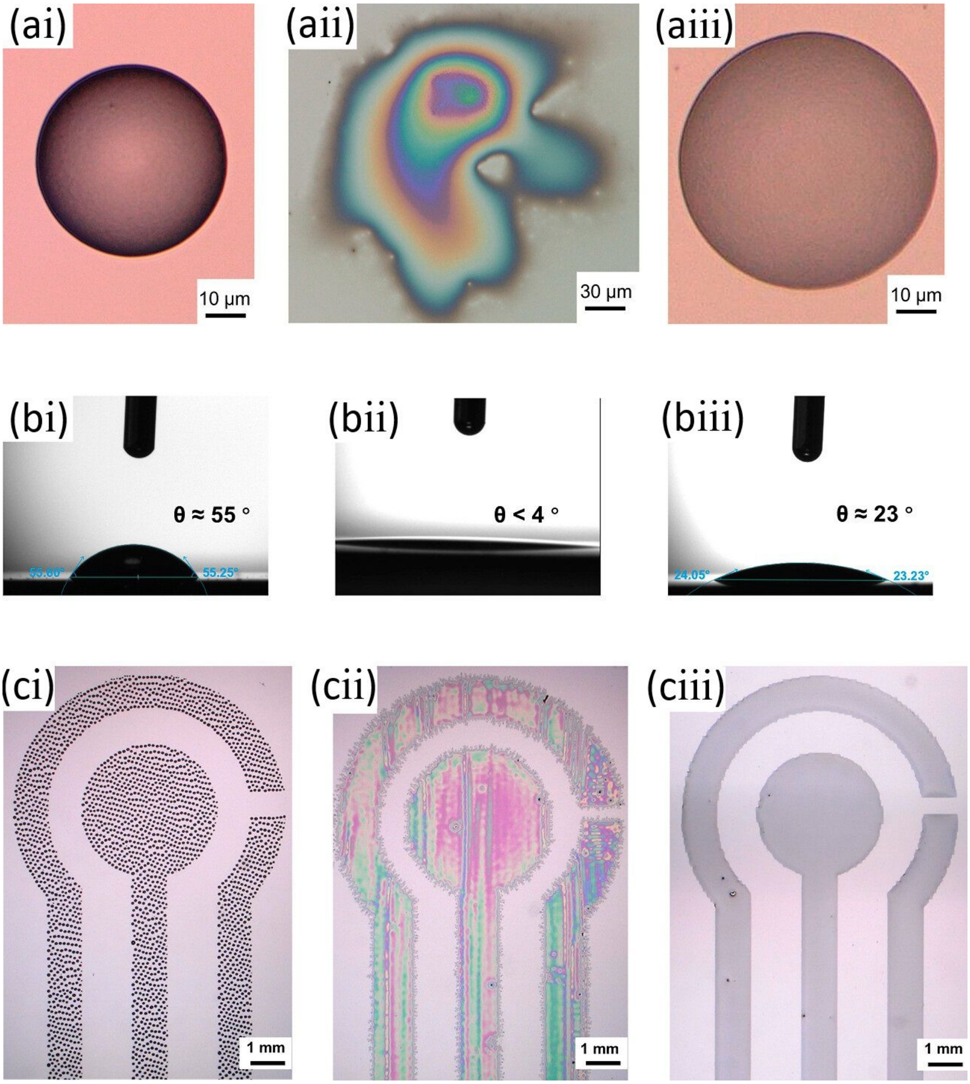

Figure 5.3: (a) Optical images of the single diamond ink droplets, (b) visualization of the contact angle measurements, and (c) optical images of printed electrode designs on various Si-based substrates: (i) pristine form, (ii) after oxygen plasma treatment, and (iii) after oxygen plasma treatment, followed by exposure to air. To print the patterns shown in (c), DPI values of (i) 1000, (ii) 300, and (iii) 750 were used.

lustrates a fairly uniform seeding with particles homogeneously distributed all over the surface with an estimated density of 1×10^{11} nanoparticles per cm^2. Such high nucleation density results from the favorable interplay between the particle content in the diamond ink, surface treatment, drying step, and DPI value. Then, the growth of the patterned BDD layer (WE and CE) was carried out in a MW-PE-CVD reactor, and the sensing chip was completed with an inkjet-printed silver RE; the results of these two fabrication steps are illustrated by optical images (b2) and (b3) in Fig. 5.2. These also visually confirm the successful bottom-up patterning of the electrode chip which was achieved via carefully optimized inkjet printing processes and thus without the use of reactive, environmentally hazardous chemicals and costly lithographic and/or laser facilities typically required in top-down approaches. Besides simplicity and cost-effectiveness, herein reported patterning strategy benefits from its additive and fully digital nature, where print modifications can be easily integrated via a computer-aided design software. As a consequence, inkjet printing offers remarkable freedom of precise electrode print designs varying in shapes and dimensions.

5.3.4. MORPHOLOGICAL CHARACTERIZATION

The chips with grown BDD layers were first subjected to morphological characterization. The optical image of the chip, depicted in Fig. 5.4(a), clearly shows well-defined and sharp edges of the BDD films following the original seeding patterns. In particular, four regions on the WE and CE, labeled 1–4, were selected for more detailed SEM analysis. Acquired SEM images [see Fig. 5.4(ci–iv)] show fully closed, pinhole-free and uniform BDD films with clearly defined polycrystalline structure. Neither delamination nor film fracture was observed, indicating good adhesion of the BDD layer to the substrate. Furthermore, the “open” character of the grains and the presence of voids can be recognized. The less developed interconnectivity between the grains can be presumably ascribed to the relatively low deposition rate resulting in thin films of limited thickness of $1.1 \pm 0.2\ \mu$m, assessed by AFM. However, the presence of voids and gaps between the grains leads to an exposed BDD surface with a roughness (Sa) of ~80 nm and with possibly increased electroactive area, which can be beneficial for electrochemical (sensing) applications. Besides, all four investigated spots show virtually the same film microstructure and a mixture of grain shapes (square and triangular facets). Nevertheless, a small difference can be identified between the various spots when the grain size is considered: in positions 1, 2, and 4, the apparent grain size is similar and ranges between 150 and 500 nm, while the grain size at position 3, i.e., at the edge of the pattern, is slightly larger (~550–600 nm) due to the unhindered three-dimensional crystal growth [Fig. 5.4(ciii)]. On the other hand, SEM micrographs of the BDD WE of the DropSens chip (displayed in Fig. 5.5(c)) also demonstrated a closed, pinhole-free polycrystalline diamond layer, however, with more uneven and irregular surface morphology and with harder-to-define submicron-sized facets. The thickness of that BDD layer, evaluated from the cross-section, is approximately 1–2 μm.

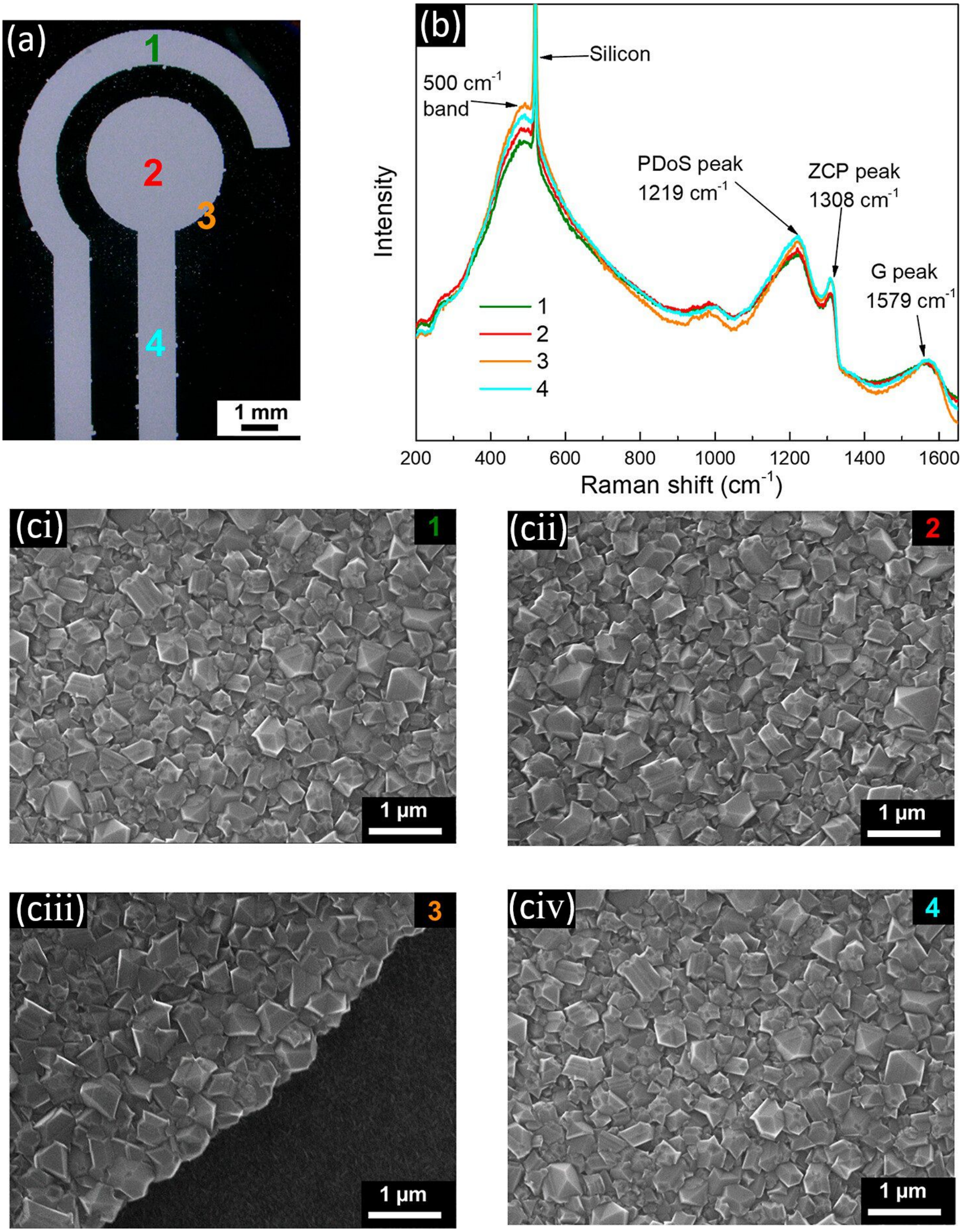

Figure 5.4: (a) Optical image of the BDD patterns on the chip. The numbers 1 to 4 indicate regions subjected to Raman and SEM analyses. (b) Raman spectra recorded at four different spots, as indicated in (a). [c(i-iv)] SEM images obtained from the same four regions labeled 1 to 4 in (a).

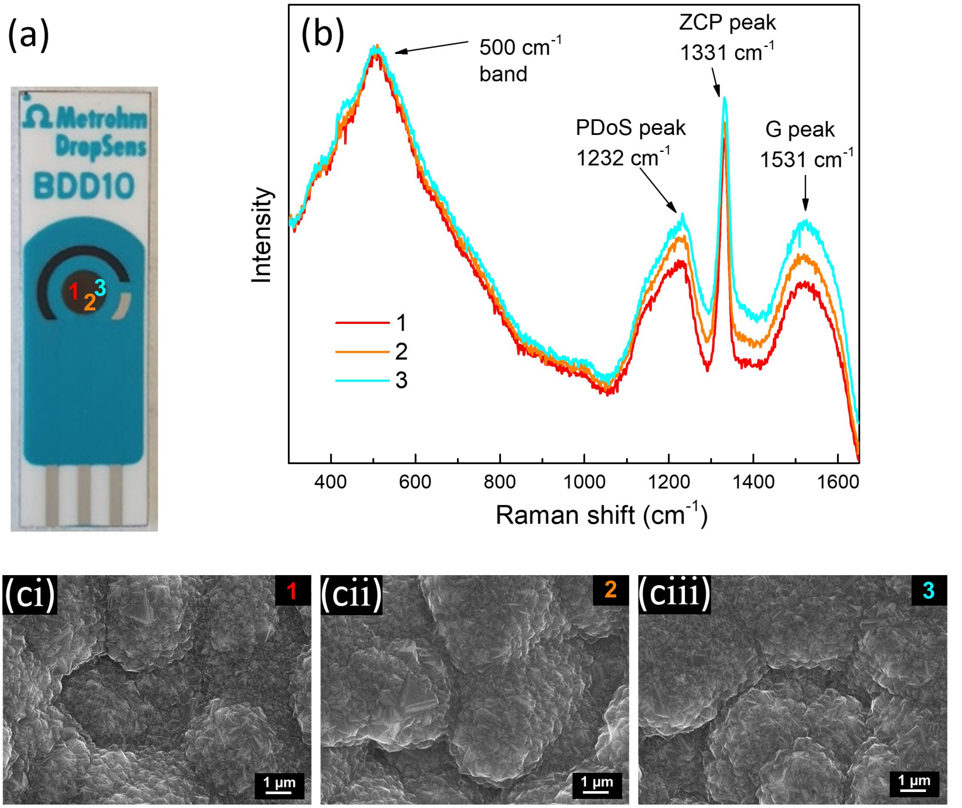

Figure 5.5: (a) Photo of the commercially available BDD sensing chip with numbers 1–3 indicating the spots where characterization was carried out. (b) Raman spectra recorded on the BDD working electrode at three different spots (specified in (a)). (c) SEM micrographs obtained for the same three locations within the BDD working electrode.

5.3.5. RAMAN ANALYSIS

The composition of the BDD layer and the estimation of boron content were carried out using Raman spectroscopy. Raman spectra of inkjet-printed BDD were recorded at the same four spots already observed by SEM and are shown in Fig. 5.4(b). Almost identical spectra revealing characteristics of highly B-doped diamond material were acquired from the selected regions, which further confirm very good homogeneity of the BDD film. The diamond's zone center phonon line is developed at 1308 cm^{-1} (sp^3-hybridized carbon), while the G-band located at 1579 cm^{-1} indicates the graphitic phase (sp^2-hybridized carbon) typically present in the grain boundaries. Next, the peak at 1219 cm^{-1} is attributed to a maximum of the phonon density of states and the 500 cm^{-1} intense broad band results from a combination of electronic Raman scattering and a Fano-shaped band [35]; both features are associated with the significant incorporation

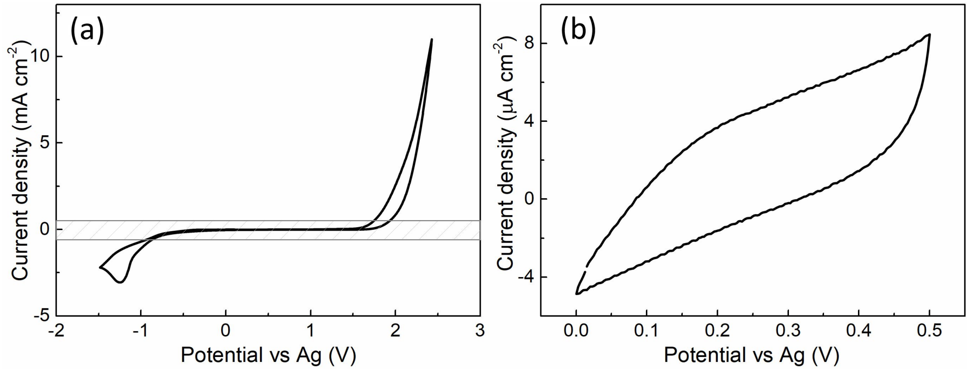

Figure 5.6: CVs recorded in 0.5 M KNO_3, at a scan rate of 0.10 V s^{-1}, in a potential range (a) from −1.5 V to +2.5 V, while the dashed line demonstrates the potential window, and (b) from 0 V to +0.5 V, used for the assessment of the C_{dl} value of the inkjet-printed BDD working electrode.

of boron atoms into the diamond lattice. The sharp peak centered at 520.7 cm^{-1} originates from the silicon substrate. The boron concentration in the grown BDD layers was estimated to be around 2×10^{21} cm^{-3}, using a freely available Raman tool [36–38], and confirmed the metal-like character of the deposited thin film. Raman spectra acquired on the commercial BDD electrode are displayed in Fig. 5.5(b) and show a similar pattern with all features as described for the inkjet-printed BDD. However, the more pronounced diamond's zone center phonon line positioned at 1331 cm^{-1} (close to the value of 1333 cm^{-1} for an intrinsic diamond) signalizes lower boron doping, which was further supported by assessment of [B] to be 1×10^{21} cm^{-3}, i.e., twice lower than in the case of the inkjet-printed BDD.

5.3.6. ELECTROCHEMICAL CHARACTERIZATION IN A SUPPORTING ELECTROLYTE

The inkjet-printed BDD chips (three in total) were used for electrochemical measurements in their as-prepared state, first for cyclic voltammetry (CV) in a supporting electrolyte of 0.5 M KNO_3 to assess (i) the width of the potential window, which is an essential feature determining the suitability for electrochemical sensing applications and (ii) the double-layer capacitance (C_{dl}). The working potential range of the inkjet-printed BDD chips was evaluated to be in average 2.5 V (see Fig. 5.6(a)), considering the anodic and cathodic potential limits as those potential values at which a current density of ±0.4 mA cm^{-2} passes the electrodes [39]. Subsequently, cyclic voltammograms were obtained in the same solution of 0.5 M KNO_3 but in a smaller potential range from 0 V to +0.5 V, where only background (i.e. non-Faradaic) current flowed through the electrode, as shown in Fig. 5.6(b). Based on these measurements and using Eq. 5.1, an average C_{dl} value of the inkjet-printed BDD layer of 27 μF cm^{-2} was calculated. The obtained values are in good agreement with the values acquired previously on highly doped ([B] > 10^{21} cm^{-3}), as-deposited and thus predominantly H-terminated BDD thin films in neutral pH media for which potential window and C_{dl} values ranged between 2.35 V and

2.60 V and between 38 μF cm^{-2} and 92 μF cm^{-2}, respectively [40–42]. The narrower potential window and higher C_{dl}, and hence deviation from "typical" features of BDD, a ~3.5 V wide working range and a $C_{dl} < 10$ μF cm^{-2} [1, 43], can be ascribed to several factors: (i) the high doping level, (ii) presence of sp^2 phase, as indicated by Raman spectra (Fig. 5.4(b)), and (iii) prevailing H-termination; all were demonstrated to contribute to a narrower potential window and increased capacitance of the BDD electrodes [40, 42, 44].

5.3.7. ELECTROCHEMICAL CHARACTERIZATION USING REDOX MARKERS

Two redox markers $[Ru(NH_3)_6]^{3+/2+}$ and $[Fe(CN)_6]^{3-/4-}$ (both 1 mM in 0.5 M KNO_3) were employed to obtain information on heterogeneous electron transfer (HET) kinetics at the as-prepared inkjet-printed BDD chips, manifested by peak-to-peak separation (ΔE_p) values extracted from cyclic voltammograms displaying well-defined pairs of the redox peak; see Fig. 5.7. The HET of $[Ru(NH_3)_6]^{3+/2+}$ occurs via an outer-sphere mechanism, hence this redox probe is insensitive to the electrode surface properties [45, 46] and the HET kinetics depends only on the density of states, i.e., content of boron dopant [46]. As a result, $[Ru(NH_3)_6]^{3+/2+}$ serves as a reliable indicator of "semiconductor" and "metal-like" conductive BDD electrodes, as at the former its HET kinetics is substantially inhibited [1]. Importantly, ΔE_p for $[Ru(NH_3)_6]^{3+/2+}$ of 0.076 V approaches 0.059 V, a value for a fully reversible one-electron redox system, which clearly indicates near-reversible behavior of this redox probe, fast HET kinetics, and confirms sufficiently high boron doping level and conductivity, in accordance with Raman spectra and estimated [B].

In contrast, $[Fe(CN)_6]^{3-/4-}$ is considered an inner-sphere redox marker, which is sensitive to electrode surface characteristics, predominantly to surface termination [44–46]. Presumably due to this sensitivity, only quasi-reversible behavior was observed with a ΔE_p of 0.145 V (recorded at v of 0.10 V s^{-1}), suggesting hindered HET kinetics compared to $[Ru(NH_3)_6]^{3+/2+}$. The increased ΔE_p value may be ascribed to the presence of oxygen functionalities, resulting from practically unavoidable partial oxidation of the electrode surface in air and/or by OH^- and HCO_3^- species naturally present in a thin layer of condensed water on the solids exposed to air [41, 47].

Finally, the scan rate study was performed, with v ranging from 0.01 V s^{-1} to 0.25 V s^{-1}, with both redox markers, as shown in Fig. 5.7. Evaluation of the peak current density as function of the square root of v (see the insets in Fig. 5.7) proved this dependence to be linear, which confirmed diffusion-controlled redox reactions for both redox systems. Besides, ΔE_p for $[Ru(NH_3)_6]^{3+/2+}$ remained stable within the whole tested scan rate range and confirmed near-reversible character, while in the case of $[Fe(CN)_6]^{3-/4-}$, ΔE_p increased with an increase of the scan rate, which again indicates quasi-reversible behavior. Moreover, the slope of peak current vs $v^{1/2}$ dependence obtained for $[Ru(NH_3)_6]^{3+/2+}$ was applied to Eq. 5.2 for calculating the effective surface area (A_{eff}). The assessed A_{eff} value represents 13.3 mm^2 and is very close to an A_{geom} of 14 mm^2. The same scan rate study was also performed with a commercial chip (not shown) for which an A_{eff} of 5.3 mm^2 was derived while A_{geom} is 9.6 mm^2.

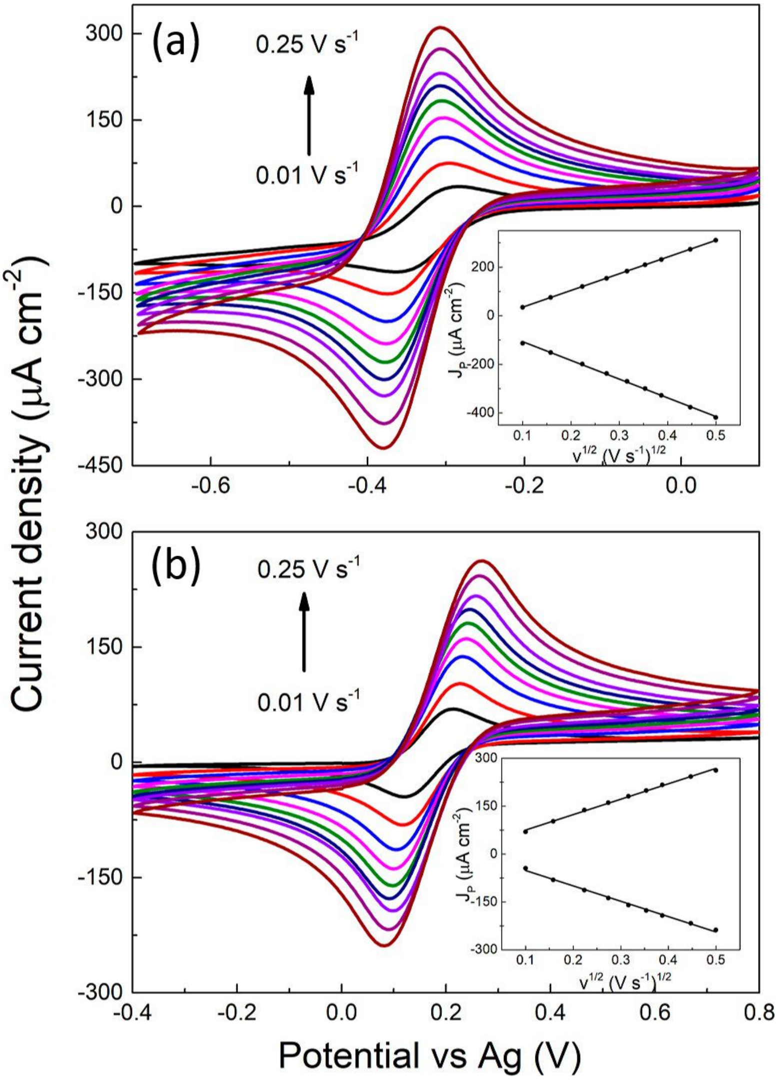

Figure 5.7: Cyclic voltammograms recorded in (a) $[Ru(NH_3)_6]^{3+/2+}$ and (b) $[Fe(CN)_6]^{3-/4-}$ (both 1 mM in 0.5 M KNO_3) on an inkjet-printed BDD sensing chip at different scan rates. Insets show the linear dependence of the peak current densities on the square root of the scan rate.

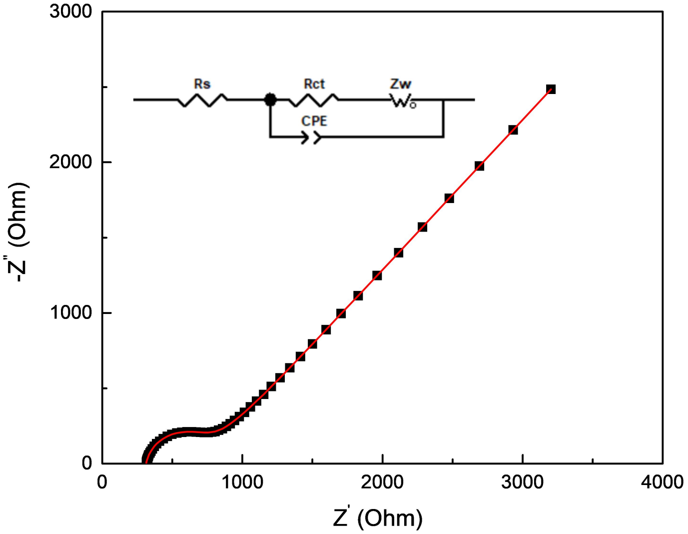

Figure 5.8: Nyquist plot (black squares) recorded in 1 mM $[Fe(CN)_6]^{3-/4-}$ in 0.5 M KNO_3 on the inkjet-printed BDD chip under the formal potential of the redox probe and fitted (red line) with the equivalent Randles circuit (depicted as inset).

5.3.8. ELECTROCHEMICAL IMPEDANCE SPECTROSCOPIC MEASUREMENTS

Impedance spectra were recorded on the inkjet-printed BDD chip in a $[Fe(CN)_6]^{3-/4-}$ solution (1 mM in 0.5 M KNO_3) using the formal potential of the redox probe (see Fig. 5.8). The acquired Nyquist plots were well-fitted with the Randles equivalent circuit, and the following values were extracted: a charge-transfer resistance (R_{CT}) of 61 Ω cm^2 and a constant phase element of 25 μF cm^{-2} s^{n-1} (value n being 0.870). These values are again slightly higher than previously reported for highly doped, either as-deposited or cathodically pretreated (i.e., H-terminated [48, 49]) BDD electrodes, which is an indication of a small contribution of oxygen groups formed because of exposure to the ambient atmosphere. However, the obtained R_{CT} value is still considerably smaller than the ones reported for $[Fe(CN)_6]^{3-/4-}$ on intentionally and severely oxidized (O-terminated) BDD electrodes (in the range of kΩ cm^2) [48].

5.3.9. CYCLIC VOLTAMMETRY OF ORGANIC ANALYTES

Finally, to demonstrate the suitability of the inkjet-printed BDD chips for electrochemical applications, particularly sensing, the newly fabricated chips were subjected to CV measurements in the presence of five organic compounds varying in chemical structure and thus presence of electroactive group, redox mechanism, and oxidation potentials. Specifically, commonly detected compounds of high (bio)importance were selected: dopamine with a catechol moiety, ascorbic acid containing a furan-based lactone, phenol-derived tyrosine (depicted in Fig. 5.9), glucose consisting of a pyran ring with hydroxyl groups, and uric acid with a purine moiety (depicted in Fig. 5.10). The electrochemical performance of the chips developed herein was compared with that of the

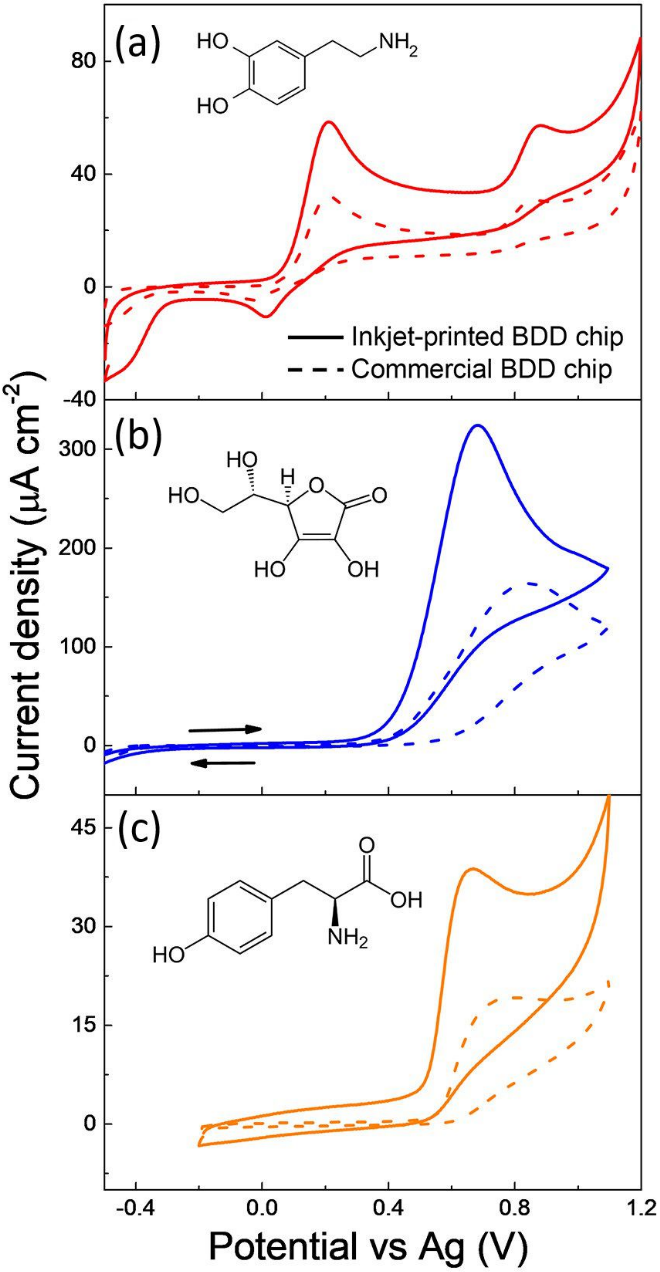

Figure 5.9: Cyclic voltammograms recorded on (full line) inkjet-printed BDD and (dashed line) commercially obtained BDD chips in a solution of (a) 100 μM dopamine in 10 mM phosphate buffered saline at pH = 7.4, (b) 1 mM ascorbic acid in 0.1 M H_2SO_4, and (c) 100 μM tyrosine in 10 mM phosphate buffered saline at pH = 7.4. The chemical structures of the compounds are also displayed.

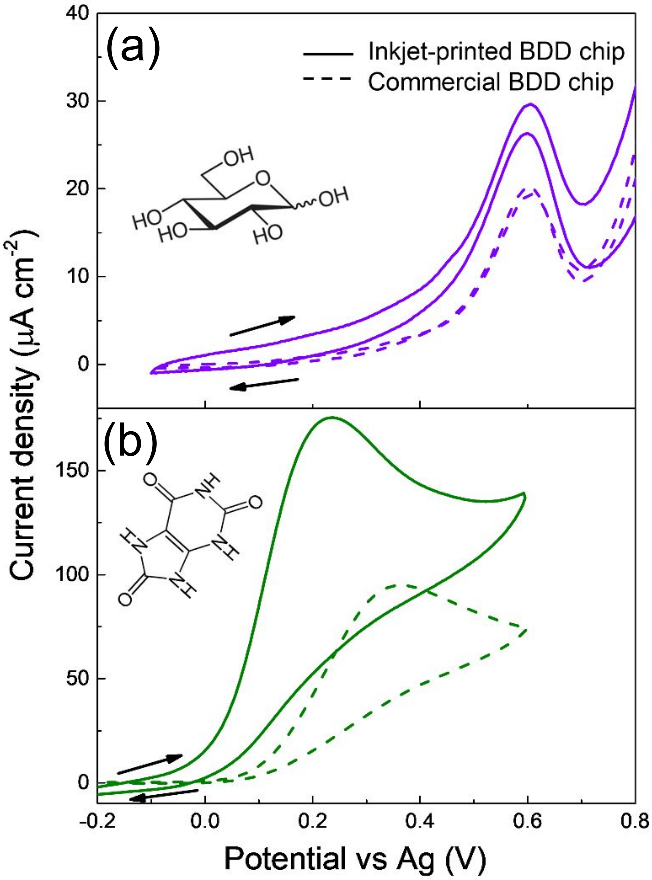

Figure 5.10: CVs recorded on (full line) inkjet-printed BDD and (dashed line) commercially obtained BDD chips in a solution of (a) 1 mM glucose in 0.1 M NaOH and (a) 1 mM uric acid in 0.1 M NaOH. The arrows indicate the CV scan direction. The chemical structures of the tested compounds are also displayed.

commercially obtained BDD sensing chip (from Metrohm DropSens). As clearly demonstrated by Figs. 5.9 and 5.10, CV responses of all analytes were successfully recorded on our inkjet-printed BDD chips and provided 20–49% higher current densities for the tested compounds as well as higher background currents in contrast to commercially obtained chips (responses visualized by dashed lines in Fig. 5.9).

Recorded differences in electrochemical behavior can be presumably related to the larger effective surface area of the inkjet-printed BDD layer resulting from the higher doping and more "open structure" containing voids and gaps between the grains, as demonstrated by Raman and SEM analyses. Specifically, the most significant increases of 49% and 41% in recorded peak current densities were recognized for ascorbic and uric acid in acidic media, respectively; in the case of dopamine, tyrosine (in a neutral saline), and glucose (in a sodium hydroxide solution), the increases represented 28%, 36%, and 20%, respectively. Furthermore, the acquired oxidation potentials on in-house developed BDD chips were either almost identical (dopamine, tyrosine, and glucose) or slightly lower by 80 mV and 90 mV (ascorbic and uric acid, respectively) in comparison with the commercial chip.

Dopamine and ascorbic acid have also been used as redox markers since their redox reactions proceed through an inner-sphere mechanism, and they are thus sensitive to the electrode surface chemistry [40, 45, 46]. Cyclic voltammograms of dopamine, in Fig. 5.9(a), clearly display, in a potential range from −0.20 to +0.60 V, a quasi-reversible dopamine/dopamine-o-quinone redox pair with ΔE_p of 0.19 V on the inkjet-printed chip and ΔE_p of 0.23 V on the commercial chip. This demonstrates facilitated dopamine HET kinetics on the former sensing device. Similar ΔE_p values for this redox system on as-grown (untreated) BDD electrodes can be found in the literature [40, 42]. Besides, dopamine-o-quinone may undergo a spontaneous ring closure resulting in the formation of leucodopaminechrome, which may be further oxidized into dopaminechrome [50]; described oxidation reaction is manifested by the second anodic peak appearing in cyclic voltammograms at +0.80 V (see Fig. 5.9(a)). Furthermore, sp^2 carbon impurities present on the BDD surface may act as adsorption sites for dopamine molecules; however, no fouling effects were recognized on the inkjet-printed BDD chips, which could be ascribed to dopamine adsorption. In contrast, oxidation of ascorbic acid is of an irreversible nature as no cathodic peak was discerned in the recorded CVs, depicted in Fig. 5.9(b). Hence, the anodic peak potential, $E_\text{p,AA}$, reflects the HET kinetics of this compound. Ascorbic acid is considered to be sensitive to the surface termination, and for H-terminated BDD electrodes, $E_\text{p,AA}$ of $+0.80 \pm 0.01$ V (vs Ag/AgCl) has been previously reported [45, 51], and similar $E_\text{p,AA}$ values of +0.71 V (vs Ag) and +0.80 V (vs Ag) were recognized on the inkjet-printed and commercial BDD chips, respectively.

Notably, the glucose signal at a potential of +0.6 V was clearly discerned on both inkjet-printed and commercial BDD chips and is displayed in Fig. 5.10(a). This further supports the presence of surface sp^2 carbon phase, also evidenced by Raman spectroscopy (see Figs. 5.4(b) and 5.5(b)), which is a crucial element enabling and catalyzing the glucose oxidation on a BDD electrode, as verified in Ref. [52].

Chip-to-chip signal reproducibility was assessed on three inkjet-printed BDD electrode chips prepared in one batch under the same experimental conditions. Notably, high reproducibility and thus small sample-to-sample variations were recognized as convincingly demonstrated in Fig. 5.11. The relative standard deviation values of the peak current densities were less than 1% for dopamine (first anodic peak), ascorbic acid, and uric acid, and ca. 2% for tyrosine and glucose. Besides, minimal variations in peak potentials were documented for dopamine and uric acid, while a potential difference in a range from 50 to 80 mV was noticed for ascorbic acid, tyrosine, and glucose (see Fig. 5.11); importantly, relative standard deviation values of the peak potentials recorded for all five analytes are ≤5%. This signifies that the carefully optimized inkjet printing-based manufacturing approach leads to the fabrication of BDD electrode chips of highly comparable and reproducible electrochemical behavior.

All in all, it can be concluded that the novel BDD-based sensing chips fabricated via the inkjet printing route do not suffer any apparent drawbacks that would limit their application for sensing, and their electrochemical performance is comparable with BDD

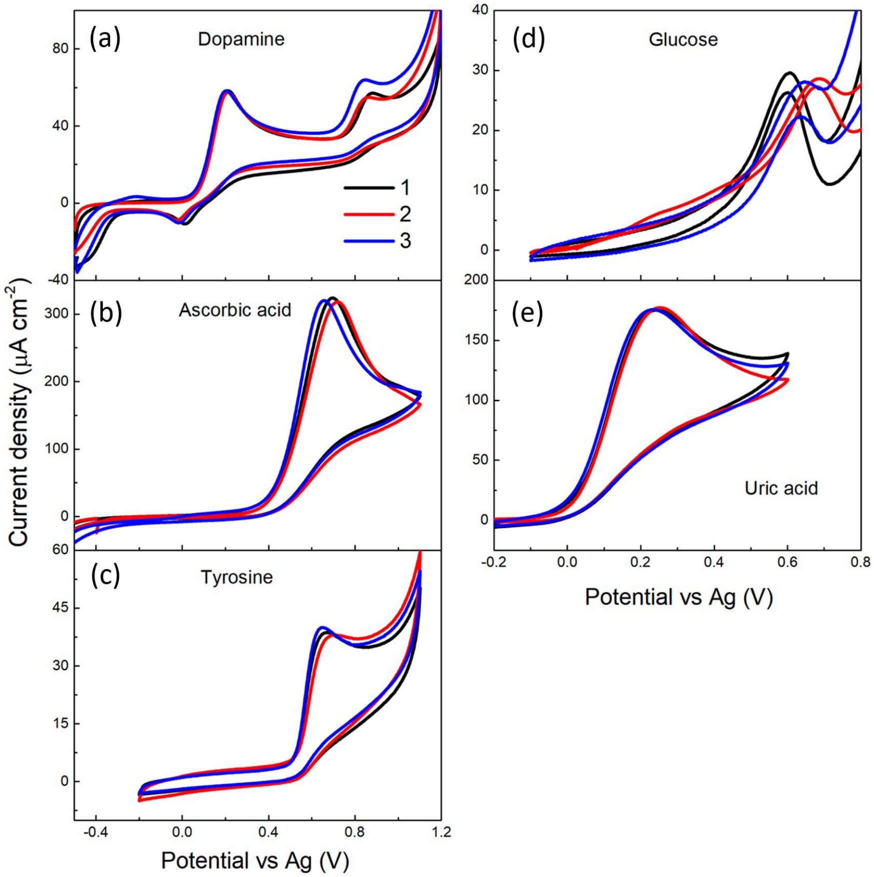

Figure 5.11: Cyclic voltammograms recorded on three different inkjet-printed BDD sensing chips (sample-to-sample variation) in a solution of (a) 100 μM dopamine in 10 mM phosphate buffered saline of pH = 7.4, (b) 1 mM ascorbic acid in 0.1 M H_2SO_4, (c) 100 μM tyrosine in 10 mM phosphate buffered saline of pH = 7.4, (d) 1 mM glucose in 0.1 M NaOH, and (e) 1 mM uric acid in 0.1 M NaOH.

films grown using conventional seeding procedures based on electrostatic seeding by dip coating, for example [34].

Besides having the ability to electrochemically detect organic compounds of various structural motifs, developed inkjet-printed BDD three-electrode chips can be used repeatedly over time, as convincingly demonstrated in Fig. 5.12 for dopamine, ascorbic acid, and tyrosine. The same set of measurements as described above was repeated with the same chip after having been shelfed for 2 months at room temperature. The peak potentials of all tested analytes remained practically unaffected, and a shift of a maximum of 30 mV was observed (for ascorbic acid, see Fig. 5.12(b)), which indicates a very good stability and a high reliability of the inkjet-printed silver RE. Similarly, the signals of the same intensity were recorded for ascorbic acid after 2 months (a change of less than 4%), while for dopamine and tyrosine only a drop of 10.4% and 13.9% in the peak

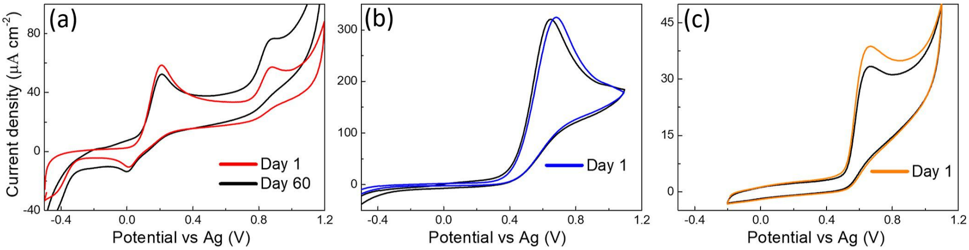

Figure 5.12: CVs were obtained on the same chip at (color line) day 1 and (black line) day 60 in a solution of (a) 100 μM dopamine in 10 mM phosphate buffered saline of pH = 7.4, (b) 1 mM ascorbic acid in 0.1 M H2SO4, and (c) 100 μM tyrosine in 10 mM phosphate buffered saline of pH = 7.4.

current density, respectively, was recognized. It needs to be emphasized that these very promising results were obtained without any pre-treatment or activation, and one can expect that incorporation of such a step may enhance the signal repeatability. This certainly demonstrates a significant advantage of the newly developed BDD three-electrode chips in comparison with commercially available ones, typically promoted as disposable and for one-time use only.

Moreover, the novel inkjet printing-based manufacturing approach described herein is not only limited to silicon-based substrates but also can be easily expanded to a wider range of supporting materials (e.g., ceramic) with only fine-tuning the ink composition and wetting properties of the selected substrate. Besides, this is the first report on a BDD layer growth by CVD from the nanodiamond-containing nucleation layer formed on a substrate via the inkjet printing approach. The used CVD protocol favored boron incorporation into the diamond lattice and ensured high boron doping, as confirmed by the Raman spectra (see Fig. 5.4(b) and thus high electrical conductivity of the deposited BDD WE and CE, but it also resulted in a relatively increased sp^2 carbon content. Nevertheless, the CVD protocol may be modified by adjusting the deposition parameters to achieve BDD thin films of different (potentially tailored) morphologies, compositions, and microstructures, depending on the requirements of intended applications.

5.4. CONCLUSION

In this work, a simplified, lithography-free, bottom-up fabrication route for the BDD three-electrode sensing chips is reported utilizing direct inkjet printing of nanodiamond-containing ink on silicon-based substrates. The patterning was successfully accomplished without the use of reactive chemicals and costly cleanroom facilities. Following the BDD growth and completion of the chip with the inkjet-printed silver RE, CV experiments in a supporting electrolyte and solutions of redox markers and structurally different organic compounds demonstrated highly satisfactory electrochemical performance, comparable to that of a BDD electrode prepared by a conventional seeding technique. No drawbacks that could potentially limit the applications of the novel inkjet-printed BDD chips were identified.

Markedly, a fully digital inkjet printing technique enables exceptional freedom of precise electrode print designs of various geometries and dimensions ranging from the micro- (μm) to macro- (cm) scale. Furthermore, selective area seeding via utilization of inkjet printing can be expanded to a variety of supporting materials upon tailoring the diamond ink composition and wetting features of the substrate surfaces, including three-dimensional substrates, not being compatible with conventional lithographic techniques.

All in all, the newly developed chip-based manufacturing method allows the rapid prototyping of different small-scale electrode designs and BDD microstructures, which can lead to enhanced sensor performance and to expansion of the miniaturized BDD electrodes for on-site electrochemical measurements and development of point-of-care devices.

BIBLIOGRAPHY

[1] J. V. Macpherson, “A practical guide to using boron doped diamond in electrochemical research”, Phys. Chem. Chem. Phys. **17**, 2935–2949 (2015).

[2] R. S. Balmer, J. R. Brandon, S. L. Clewes, H. K. Dhillon, J. M. Dodson, I. Friel, P. N. Inglis, T. D. Madgwick, M. L. Markham, T. P. Mollart, et al., “Chemical vapour deposition synthetic diamond: materials, technology and applications”, Journal of Physics: Condensed Matter **21**, 364221 (2009).

[3] Y. Zheng, C. Li, J. Liu, J. Wei, X. Zhang, H. Ye, and X. Ouyang, “Chemical vapor deposited diamond with versatile grades: from gemstone to quantum electronics”, Frontiers of Materials Science **16**, 220590 (2022).

[4] Y.-J. Lu, C.-N. Lin, and C.-X. Shan, “Optoelectronic diamond: growth, properties, and photodetection applications”, Advanced Optical Materials **6**, 1800359 (2018).

[5] N. J. Yang, S. Y. Yu, J. V. Macpherson, Y. Einaga, H. Y. Zhao, G. H. Zhao, G. M. Swain, and X. Jiang, “Conductive diamond: synthesis, properties, and electrochemical applications”, Chemical Society Reviews **48**, 157–204 (2019).

[6] S. Baluchova, A. Danhel, H. Dejmkova, V. Ostatna, M. Fojta, and K. Schwarzova-Peckova, “Recent progress in the applications of boron doped diamond electrodes in electroanalysis of organic compounds and biomolecules - a review”, Analytica Chimica Acta **1077**, 30–66 (2019).

[7] C. P. Sousa, F. W. P. Ribeiro, T. M. B. F. Oliveira, G. R. Salazar-Banda, P. de Lima-Neto, S. Morais, and A. N. Correia, “Electroanalysis of pharmaceuticals on boron-doped diamond electrodes: a review”, ChemElectroChem **6**, 2350–2378 (2019).

[8] P. Joshi, P. Riley, K. Y. Goud, R. K. Mishra, and R. Narayan, “Recent advances of boron-doped diamond electrochemical sensors toward environmental applications”, Current Opinion in Electrochemistry **32**, 100920 (2022).

[9] O. Sarakhman and Ľ. Švorc, “A review on recent advances in the applications of boron-doped diamond electrochemical sensors in food analysis”, Critical Reviews in Analytical Chemistry **52**, 791–813 (2022).

[10] M. Domonkos, P. Demo, and A. Kromka, “Nanosphere lithography for structuring polycrystalline diamond films”, Crystals **10**, 356 (2020).

[11] M. L. Hicks, A. C. Pakpour-Tabrizi, and R. B. Jackman, “Polishing, preparation and patterning of diamond for device applications”, Diamond and Related Materials **97**, 107424 (2019).

[12] A. Sugitani, M. Katayama, T. Watanabe, Y. Matsumoto, and Y. Einaga, “Fabrication of boron doped diamond chip electrodes for single drop analysis”, RSC Advances **3**, 25636–25639 (2013).

[13] B. Ali, I. Litvinyuk, and M. Rybachuk, “Femtosecond laser micromachining of diamond: current research status, applications and challenges”, Carbon **179**, 209–226 (2021).

[14] O. Shimoni, J. Cervenka, T. J. Karle, K. Fox, B. C. Gibson, S. Tomljenovic-Hanic, A. D. Greentree, and S. Prawer, “Development of a templated approach to fabricate diamond patterns on various substrates”, ACS Applied Materials & Interfaces **6**, 8894–8902 (2014).

[15] A. F. Sartori, B. H. L. Overes, P. Fanzio, M. Tsigkourakos, L. Sasso, and J. G. Buijnsters, “Template-assisted bottom-up growth of nanocrystalline diamond micropillar arrays”, Diamond and Related Materials **95**, 20–27 (2019).

[16] H. Zhuang, B. Song, T. Staedler, and X. Jiang, “Microcontact printing of monodiamond nanoparticles: an effective route to patterned diamond structure fabrication”, Langmuir **27**, 11981–11989 (2011).

[17] T. Vandenryt, L. Grieten, S. D. Janssens, B. van Grinsven, K. Haenen, B. Ruttens, J. D’Haen, P. Wagner, R. Thoelen, and W. De Ceuninck, “Rapid fabrication of micron-sized CVD-diamond structures by microfluidic contact printing”, Physica Status Solidi A **211**, 1448–1454 (2014).

[18] A. C. Taylor, R. Edgington, and R. B. Jackman, “Patterning of nanodiamond tracks and nanocrystalline diamond films using a micropipette for additive direct-write processing”, ACS Applied Materials & Interfaces **7**, 6490–6495 (2015).

[19] Z. Y. Xu, L. Z. Wang, X. Huan, H. Lee, J. Yang, Z. W. Zhou, M. J. Chen, S. Q. Hu, Y. Liu, S. P. Feng, et al., “On-demand, direct printing of nanodiamonds at the quantum level”, Advanced Science **9**, 2103598 (2022).

[20] N. A. Fox, M. J. Youh, J. W. Steeds, and W. N. Wang, “Patterned diamond particle films”, Journal of Applied Physics **87**, 8187–8191 (2000).

[21] Y. C. Chen, Y. H. Tzeng, A. Davray, A. J. Cheng, R. Ramadoss, and M. Park, “Fabrication of diamond micro-structures by ink-jet printed diamond seeding and microwave plasma assisted chemical vapor deposition”, Diamond and Related Materials **17**, 722–727 (2008).

[22] Y. C. Chen, Y. Tzeng, A. J. Cheng, R. Dean, M. Park, and B. M. Wilamowski, “Inkjet printing of nanodiamond suspensions in ethylene glycol for CVD growth of patterned diamond structures and practical applications”, Diamond and Related Materials **18**, 146–150 (2009).

[23] A. F. Sartori, P. Belardinelli, R. J. Dolleman, P. G. Steeneken, M. K. Ghatkesar, and J. G. Buijnsters, “Inkjet-printed high-q nanocrystalline diamond resonators”, Small **15**, 1803774 (2019).

[24] A. Laposa, J. Kroutil, M. Davydova, A. Taylor, J. Voves, L. Klimsa, J. Kopecek, and M. Husak, "Inkjet seeded CVD-grown hydrogenated diamond gas sensor under UV-LED illumination", IEEE Sensors Journal **20**, 1158–1165 (2020).

[25] A. Moya, G. Gabriel, R. Villa, and F. J. del Campo, "Inkjet-printed electrochemical sensors", Current Opinion in Electrochemistry **3**, 29–39 (2017).

[26] A. D. Ambaye, K. K. Kefeni, S. B. Mishra, E. N. Nxumalo, and B. Ntsendwana, "Recent developments in nanotechnology-based printing electrode systems for electrochemical sensors", Talanta **225**, 121951 (2021).

[27] T. Kant, K. Shrivas, K. Dewangan, A. Kumar, N. K. Jaiswal, M. K. Deb, and S. Pervez, "Design and development of conductive nanomaterials for electrochemical sensors: a modern approach", Materials Today Chemistry **24**, 100769 (2022).

[28] T. Kondo, H. Sakamoto, T. Kato, M. Horitani, I. Shitanda, M. Itagaki, and M. Yuasa, "Screen-printed diamond electrode: a disposable sensitive electrochemical electrode", Electrochemistry Communications **13**, 1546–1549 (2011).

[29] T. Kondo, I. Udagawa, T. Aikawa, H. Sakamoto, I. Shitanda, Y. Hoshi, M. Itagaki, and M. Yuasa, "Enhanced sensitivity for electrochemical detection using screen-printed diamond electrodes via the random microelectrode array effect", Analytical Chemistry **88**, 1753–1759 (2016).

[30] T. Kondo, M. Horitani, H. Sakamoto, I. Shitanda, Y. Hoshi, M. Itagaki, and M. Yuasa, "Screen-printed modified diamond electrode for glucose detection", Chemical Letters **42**, 352–354 (2013).

[31] T. Matsunaga, T. Kondo, T. Osasa, A. Kotsugai, I. Shitanda, Y. Hoshi, M. Itagaki, T. Aikawa, T. Tojo, and M. Yuasa, "Sensitive electrochemical detection of ciprofloxacin at screen-printed diamond electrodes", Carbon **159**, 247–254 (2020).

[32] T. Matsunaga, T. Kondo, I. Shitanda, Y. Hoshi, M. Itagaki, T. Tojo, and M. Yuasa, "Sensitive electrochemical detection of l-cysteine at a screen-printed diamond electrode", Carbon **173**, 395–402 (2021).

[33] M. Shlomo, *The chemistry of inkjet inks* (World Scientific, 2009), p. 356.

[34] S. Mandal, "Nucleation of diamond films on heterogeneous substrates: a review", RSC Advances **11**, 10159–10182 (2021).

[35] V. Mortet, I. Gregora, A. Taylor, N. Lambert, P. Ashcheulov, Z. Gedeonova, and P. Hubik, "New perspectives for heavily boron-doped diamond Raman spectrum analysis", Carbon **168**, 319–327 (2020).

[36] V. Mortet, A. Taylor, Z. Vlčková Živcová, D. Machon, O. Frank, P. Hubík, D. Tremouilles, and L. Kavan, "Analysis of heavily boron-doped diamond Raman spectrum", Diamond and Related Materials **88**, 163–166 (2018).

[37] Determination of boron concentration in diamond from Raman spectroscopy, Online Raman analysis tool available at https://ramantool.pythonanywhere.com/ (accessed 21-02-2025).

[38] V. Mortet, Z. Živcová, A. Taylor, M. Davydová, O. Frank, P. Hubík, J. Lorincik, and M. Aleshin, "Determination of atomic boron concentration in heavily boron-doped diamond by Raman spectroscopy", Diamond and Related Materials **93**, 54–58 (2019).

[39]L. A. Hutton, J. G. Iacobini, E. Bitziou, R. B. Channon, M. E. Newton, and J. V. Macpherson, “Examination of the factors affecting the electrochemical performance of oxygen-terminated polycrystalline boron-doped diamond electrodes”, Analytical Chemistry **85**, 7230–7240 (2013).

[40]M. Brycht, S. Baluchová, A. Taylor, V. Mortet, S. Sedláková, L. Klimša, J. Kopeček, and K. Schwarzová-Pecková, “Comparison of electrochemical performance of various boron-doped diamond electrodes: dopamine sensing in biomimicking media used for cell cultivation”, Bioelectrochemistry **137**, 107646 (2021).

[41]S. Baluchová, M. Brycht, A. Taylor, V. Mortet, J. Krůšek, I. Dittert, S. Sedláková, L. Klimša, J. Kopeček, and K. Schwarzová-Pecková, “Enhancing electroanalytical performance of porous boron-doped diamond electrodes by increasing thickness for dopamine detection”, Anal. Chim. Acta **1182**, 338949 (2021).

[42]S. Baluchová, A. Taylor, V. Mortet, S. Sedláková, L. Klimša, J. Kopeček, O. Hák, and K. Schwarzová-Pecková, “Porous boron doped diamond for dopamine sensing: effect of boron doping level on morphology and electrochemical performance”, Electrochim. Acta **327**, 135025 (2019).

[43]Z. Liu, S. Baluchová, A. F. Sartori, Z. Li, Y. Gonzalez-Garcia, M. Schreck, and J. G. Buijnsters, “Heavily boron-doped diamond grown on scalable heteroepitaxial quasi-substrates: a promising single crystal material for electrochemical sensing applications”, Carbon **201**, 1229–1240 (2023).

[44]K. Schwarzová-Pecková, J. Vosáhlová, J. Barek, I. Šloufová, E. Pavlova, V. Petrák, and J. Zavázalová, “Influence of boron content on the morphological, spectral, and electroanalytical characteristics of anodically oxidized boron-doped diamond electrodes”, Electrochim. Acta **243**, 170–182 (2017).

[45]M. C. Granger, M. Witek, J. Xu, J. Wang, M. Hupert, A. Hanks, M. D. Koppang, J. E. Butler, G. Lucazeau, M. Mermoux, J. W. Strojek, and G. M. Swain, “Standard electrochemical behavior of high-quality, boron-doped polycrystalline diamond thin-film electrodes”, Anal. Chem. **72**, 3793–3804 (2000).

[46]J. A. Bennett, J. Wang, Y. Show, and G. M. Swain, “Effect of sp2-bonded nondiamond carbon impurity on the response of boron-doped polycrystalline diamond thin-film electrodes”, J. Electrochem. Soc. **151**, E306 (2004).

[47]G. R. Salazar-Banda, L. S. Andrade, P. A. P. Nascente, P. S. Pizani, R. C. Rocha-Filho, and L. A. Avaca, “On the changing electrochemical behaviour of boron-doped diamond surfaces with time after cathodic pre-treatments”, Electrochim. Acta **51**, 4612–4619 (2006).

[48]B. Oliveira and A. M. Oliveira-Brett, “Voltammetric and electrochemical impedance spectroscopy characterization of a cathodic and anodic pre-treated boron doped diamond electrode”, Electrochim. Acta **55**, 4599–4605 (2010).

[49]M. Zelenský, J. Fischer, S. Baluchová, L. Klimša, J. Kopeček, M. Vondráček, L. Fekete, J. Eidenschink, F. M. Matysik, S. Mandal, et al., “Chem-mechanical polishing influenced morphology, spectral and electrochemical characteristics of boron doped diamond”, Carbon **203**, 363–376 (2023).

[50] J. Breczko, M. E. Plonska-Brzezinska, and L. Echegoyen, “Electrochemical oxidation and determination of dopamine in the presence of uric and ascorbic acids using a carbon nano-onion and poly(diallyldimethylammonium chloride) composite”, Electrochim. Acta **72**, 61–67 (2012).

[51] D. A. Tryk, H. Tachibana, H. Inoue, and A. Fujishima, “Boron-doped diamond electrodes: the role of surface termination in the oxidation of dopamine and ascorbic acid”, Diamond and Related Materials **16**, 881–887 (2007).

[52] Z. Liu, A. F. Sartori, and J. G. Buijnsters, “Role of sp^2 carbon in non-enzymatic electrochemical sensing of glucose using boron-doped diamond electrodes”, Electrochem. Commun. **130**, 107096 (2021).

6

6

CONCLUSION AND OUTLOOK

This concluding chapter summarizes the key results from individual chapters and gives a perspective on future works.

THE overarching goal of this thesis is to enhance the understanding and application of BDD electrodes in electrochemical sensing. With a focus on both material properties and innovative electrode fabrication techniques, this work aimed to contribute new insights into the use of BDD in sensor technologies.

6.1. CONCLUSION

First, this work investigated the heterogeneity in electrochemical activity across polycrystalline BDD at the microscale, examining how factors like crystallographic orientation, sp^2 carbon content, and boron doping influence localized electrochemical performance. This approach addressed the need for a deeper understanding of BDD's material characteristics and their effects on sensing reliability. Additionally, the study compared single-crystal and polycrystalline BDD, focusing on how variations in sp^2 carbon content and boron doping impact the sensing ability, anti-fouling properties, and stability in detecting complex molecules, such as glucose and dopamine, to meet specific electrochemical sensing needs. Finally, this research developed a scalable inkjet printing method to fabricate BDD-based three-electrode sensor chips, offering a cost-effective alternative to conventional manufacturing techniques and supporting the broader applicability of BDD in real-world sensing applications. Together, these objectives form a cohesive framework for enhancing BDD-based such sensing technologies.

The second chapter focused on the localized variations in electrochemical activity within polycrystalline BDD electrodes, emphasizing how structural and compositional heterogeneity affects sensing performance. Advanced mapping techniques—such as SEM, EBSD, and SECM—revealed significant heterogeneity in electrochemical activity that closely correlated with grain orientation, sp^2 carbon content, and boron doping level. The grains, which were predominantly (110)-oriented with portions of (100) and (111) facets, demonstrated varying boron uptake efficiencies, with the (111) facets incorporating the highest levels of boron dopants. This variation in boron content led to considerable differences in local electrochemical activity. Heavily doped (111) grains exhibited strong electrochemical responses, while (100)-oriented grains, despite similar boron levels, showed lower electrochemical activity. Additionally, although grain boundaries contained higher levels of boron and sp^2 carbon impurities, these regions did not display increased electrochemical activity. SECM data supported this, showing that activity hotspots did not align with grain boundaries but were associated with highly boron-doped (111) facets. By examining the influence of microstructural features on electrochemical activity, this chapter sheds light on the crucial role of optimizing the crystal orientation in polycrystalline BDD. These insights underscore the potential for tailoring BDD electrodes to achieve consistent and high performance, particularly suited to demanding electrochemical sensor applications.

The third chapter examined the effect of sp^2 carbon content on the electrochemical response of BDD electrodes, specifically in the context of non-enzymatic glucose detection. Through controlled experiments, it was established that varying the level of sp^2 carbon content significantly influences the sensitivity of BDD electrodes. Freestanding polycrystalline BDD electrodes with different amounts of sp^2 carbon were evaluated. The results showed that their nucleation surface (FS-BDD-nucl), which had the highest

sp^2 carbon content, exhibited the strongest response to glucose, achieving a sensitivity of 7.25 μA mM^{-1} cm^{-2}, in contrast to the polished surface (FS-BDD-pol) and growth surface (FS-BDD-gr) with sensitivities of 1.37 and 0.78 μA mM^{-1} cm^{-2}, respectively. This demonstrated that glucose oxidation on BDD was enhanced in the presence of sp^2 carbon, which acted as a catalytic site. Removing sp^2 carbon by anodic oxidation led to a marked decrease in sensitivity for glucose detection. This observation underscores the importance of optimizing sp^2 carbon content to balance sensitivity. The findings in this chapter provide a framework for designing BDD electrodes tailored for precise and reliable glucose detection, a valuable consideration for future (bio)chemical sensing and monitoring technologies.

The fourth chapter focused on the comparative analysis of single-crystal BDD (SC-BDD) and polycrystalline BDD (poly-BDD) in detecting dopamine, a biologically relevant molecule, to evaluate their respective strengths in terms of electrochemical activity, stability and fouling resistance. The study demonstrated that SC-BDD electrodes, particularly the heteroepitaxial (100)-oriented samples, exhibited superior electrochemical stability and anti-fouling characteristics. The SC-BDD samples maintained less than a 14% decrease in anodic peak height after five consecutive CV scans with dopamine, while the poly-BDD electrodes showed a 42% reduction under identical conditions. This notable difference indicates the enhanced resistance of SC-BDD to fouling, making it better suited for long-term electrochemical sensing applications. Furthermore, the sensitivity and detection limits of dopamine on SC-BDD and poly-BDD were compared using DPV, revealing that SC-BDD outperformed the poly-BDD electrode in terms of analytical parameters. SC-BDD achieved a wider linear range (0.25–100.0 μmol/L) and a higher sensitivity of 12.25 ± 0.01 μA/μM·cm^2. In contrast, poly-BDD exhibited a narrower linear range (0.50–75.0 μmol/L) and lower sensitivity (5.47 ± 0.07 μA/μM·cm^2). The findings underscore that the SC-BDD's minimal grain boundaries, high boron doping, and uniform crystallographic orientation collectively contribute to its superior performance. Unlike poly-BDD, which has heterogeneous grain boundaries with sp^2 carbon, SC-BDD shows consistent electrochemical responses with lower noise and background currents, thus enhancing its suitability for sensitive applications such as *in vitro* and *in vivo* dopamine detection. This chapter establishes SC-BDD as a highly promising material for electrochemical sensors, providing high precision and low maintenance requirements for complex organic molecule detection.

In the fifth chapter, a novel approach to BDD sensor chip fabrication was explored using inkjet printing technology utilizing nanodiamond containing ink and silicon-based substrates. This method offers precise control over electrode geometry and composition, allowing for the patterning of three-electrode BDD chips without costly cleanroom facilities or reactive chemicals. The developed inkjet-printed BDD chips demonstrated excellent reproducibility and performance, as validated through comparative electrochemical testing against commercially available screen-printed BDD chips. The inkjet-printed BDD chips exhibited high stability, with minimal variation in peak current density for target analytes like dopamine, ascorbic acid, and tyrosine over two months of storage. Specifically, the average current density change was less than 4% for ascorbic acid, glucose, and uric acid and below 10% for dopamine and tyrosine, underscoring their durability. This reproducibility makes inkjet-printed BDD sensors ideal for long-term applications, offering an advantage over commercially available disposable sensors. Additionally, the inkjet-printed BDD sensors delivered higher peak current densities than the commercial alternatives, particularly in acidic and alkaline solutions. Current densities were elevated by approximately 20–49%, depending on the analyte, indicating a broader effective surface area and enhanced electrochemical activity on the inkjet-printed BDD chips. The higher performance was attributed to a well-optimized diamond ink composition, fine-tuned substrate treatment, and controlled CVD growth conditions, which collectively resulted in a highly conductive BDD layer with improved sensitivity across a range of analytes, including glucose and dopamine. The inkjet printing can be applied to various substrates beyond silicon, such as ceramics, by adjusting ink composition and substrate wetting properties. This adaptability, combined with the digital control over electrode design, allows for rapid prototyping of electrode geometries from micro- to macro-scale and opens new pathways for on-site electrochemical measurements and point-of-care devices. The feasibility of miniaturized, reproducible BDD sensors fabricated via this technique thus holds great promise for expanding BDD sensor applications in healthcare.

Overall, this thesis offers a comprehensive investigation into the potential of BDD as a high-performance material for electrochemical sensors, spanning fundamental microstructural properties to fabrication approaches. By thoroughly examining material optimization, components control, and innovative manufacturing techniques, this work establishes a solid foundation for the development of adaptable, application-specific BDD sensors. Each research element has contributed valuable insights, enabling a more refined understanding of how BDD's unique properties can be optimized to address complex sensing demands. The findings presented here underscore BDD's chemical stability, broad electrochemical window, and adjustable sensitivity, positioning it as an ideal material for precise, durable, and highly responsive sensor applications.

6.2. OUTLOOK AND RECOMMENDATIONS

While this research provides significant advancements in the development of BDD electrochemical sensors, several limitations emerged, pointing to valuable directions for future exploration. A primary challenge lies in the inherent heterogeneity of polycrystalline BDD, which complicates efforts to achieve consistent electrochemical performance across sensor surfaces. Variations in grain orientation, boron distribution, and sp^2 carbon content, while partially controlled in this study, still contribute to variability in sensor response, particularly under complex sensing conditions. Another limitation encountered was the challenge in precisely controlling sp^2 carbon content, as higher boron doping levels tend to increase the sp^2 carbon content at grain boundaries, which in turn affects sensitivity and detection limits. This dual impact of boron and sp^2 carbon highlights the need for an optimal balance that maintains boron's conductive properties without compromising sensor performance due to excessive sp^2 carbon. Developing advanced synthesis techniques or post-processing treatments that mitigate grain boundary effects could facilitate a more uniform electrochemical response across polycrystalline BDD surfaces, enhancing reproducibility and reliability in sensor applications. Addressing this issue in future work could involve investigating new CVD growth methods to refine material properties. A third limitation pertains to the technical demands and scalability challenges associated with single-crystal BDD. While it has shown superior electrochemical stability and resistance to fouling, its production is currently resource-intensive and more complex than that of polycrystalline BDD, limiting its feasibility for large-scale applications. Future research could focus on developing scalable single-crystal BDD synthesis methods that lower production costs and technical barriers, thus enabling the broader use of single-crystal BDD in electrochemical sensing applications requiring long-term stability and precision, such as in continuous monitoring systems.

Looking ahead, this thesis addresses key limitations while contributing to the ongoing development of BDD sensor technology. This work represents a valuable step forward in electrochemical sensing, offering insights and practical solutions that enhance the potential of BDD as a material for advanced sensing applications. In particular, the newly developed printing-based manufacturing method allows the rapid prototyping of different small-scale BDD electrode designs and microstructures, which can improve sensor performance and expand the use of miniaturized BDD electrodes in the chemical, agriculture, and food industries as well as in environmental and biomedical applications. Enhanced sensor features, such as the use of BDD micro-electrode arrays, to build multi-analyte detection systems might be particularly useful for diagnostic monitoring. The high production costs that have historically hindered the commercial development of diamond electrodes have started to show promising reductions. In China, where synthetic diamonds now account for 95% of the global production, the massive scale of diamond production has significantly lowered the costs over the past several years. Currently, the primary applications of these diamonds remain in industrial machinery, cutting tools, jewelry, and electronics. However, as production capacity continues to expand and costs further decrease, a solid foundation is being laid for the broader application of BDD electrodes. This trend presents a robust platform for future innovations and applications of BDD electrodes.

Acknowledgements

Time truly flies—it’s hard to believe that not long ago, I was excitedly retrieving a freshly grown thin-film diamond from the CVD reactor, celebrating the successful replication of glucose detection using BDD electrodes. And now, as I wrap up my PhD thesis, I find myself not only having started a new chapter in my career but also embracing the joy and responsibility of fatherhood.

Looking back, my PhD journey has been nothing short of a roller coaster. There were sudden shifts in research direction, long delays waiting for experimental setups, lockdowns during the COVID-19 pandemic, and of course, the painstaking process of writing and publishing. Despite all of that, this journey became one of the most formative and unforgettable chapters of my life—thanks to the unwavering support and inspiration from so many incredible people. Without them, I would not only have struggled to complete this thesis, but I wouldn’t be the person I am today.

First and foremost, I want to express my deepest gratitude to my promoters.

Ivan Buijnsters, words truly fall short in capturing my appreciation. You have been the kind of mentor every PhD student dreams of: committed, detail-oriented, and remarkably patient. Every time I faced obstacles or moments of uncertainty, you were always there—proactively offering guidance, and giving me direction when I needed it most. I’ve always admired your discipline and work ethic—especially those late-night email replies that somehow always arrived exactly when I needed a push. Your approach to research is precise and grounded, yet always supportive and encouraging. Under your mentorship, I not only completed this PhD but also grew into a confident and independent researcher. For all this, I am sincerely and endlessly thankful.

Urs, you are a true visionary and a charismatic leader. Under your guidance, the MNE group has become a nurturing and vibrant research community. From the very first moment we met, you brought warmth, encouragement, and positivity into every interaction. Talking with you always left me motivated and inspired—you have a rare gift for making people feel seen and supported.

Murali, you were the first person I met during my PhD interview, and since then, every conversation—whether about research or life—has offered valuable insight. Thank you for your wisdom and kindness.

Angelo, from the very beginning, I’ve looked up to you as a role model. Your drive, passion, and determination are infectious. You never stop pushing forward, and that spirit has been deeply motivating for me.

Marcel, thank you for your steadfast support, especially during the final phase of writing this thesis. Your help and encouragement meant a lot to me when I needed it most.

Andres, I truly appreciated your sharp and thoughtful questions during group meetings, as well as your generous help with inkjet printing technology.

I would also like to extend my heartfelt thanks to all the committee members for generously dedicating their valuable time and effort to reviewing my thesis. Your feedback and evaluation mean a great deal to me.

To my dear paranymphs, **Sifeng** and **Hava**—**Sifeng**, When you first joined the PME office for your PhD and greeted everyone on your very first day, I immediately knew that I would no longer be the one who enjoyed chatting the most—because you clearly enjoyed it even more than I did. You are always optimistic, positive, and full of energy. Thank you for organizing so many parties and poker nights, which truly brought a great deal of joy and laughter to all of us. It is a great honor to have you as my paranymph. I was also delighted to hear that you have just submitted your Form B and are about to graduate. I sincerely wish you all the best and a bright future ahead.

Hava, meeting you during my PhD journey has been a true privilege. In your work, you always demonstrated remarkable precision, dedication, and an unwavering sense of responsibility. Your perseverance and resilience in the face of challenges deeply impressed me, and your steady determination was a constant source of inspiration. Beyond your professionalism, our conversations were always enriched by your curiosity, cultural insight, and thoughtful perspectives. Thank you as well for introducing me to the joy of real Turkish coffee—a small but unforgettable moment that I will always associate with your warmth and generosity.

Ahmed, our countless conversations, ranging from deep scientific discussions to the everyday randomness of life, remain among my fondest memories. Your unique blend of humor and intellect never failed to brighten even the busiest days. Now that you have completed your postdoctoral journey and are about to begin an exciting new chapter, I would like to extend my warmest congratulations. I sincerely wish you every success in what lies ahead.

Simona, you were my most important collaborator throughout this journey, and your involvement played a pivotal role in the successful publication of my final three papers. Your guidance—particularly in figure preparation and manuscript editing—was truly invaluable. Your sharp scientific insight and relentless attention to detail not only elevated the quality of our work but also profoundly shaped the way I now approach research. From securing NWO funding to becoming an assistant professor at Charles University, your academic path continues to inspire me. I feel incredibly fortunate to have worked alongside you, and I sincerely wish you a future filled with continued scientific success and fulfillment.

André, thank you for mentoring me during the early stages of my PhD. Your clarity of thought and rigorous attitude left a strong and lasting impression on how I tackle problems.

Our MNE group has always been a place filled with energy, intelligence, and kindness. **Pieter**, you are truly the group's walking encyclopedia—whenever I had a question, you always seemed to have the answer ready. **Qais**, your dedication and unwavering focus are deeply admirable. **Ebrahim**, my cheerful companion—every conversation with you was a delightful mix of randomness and laughter. **Giulio**, I believe it is more than time that we finally share that long-promised drink. **Francesco**, your expertise in microneedles is truly exceptional; thank you for the stimulating discussions and for so generously sharing your insights.

To many other amazing members of the MNE family—**Tomas**, **Daniel**, **Kai**, and **Gurhan**—thank you for being such wonderful colleagues.

At PME, I've also had the pleasure of meeting so many brilliant and warm-hearted people: **Pierre**, **Serena**, **Satadal**, **Martin**, **Hadi**, **Andrea**, **Ali**, **Matthijs**, **Irek**, and **Ruben**—it has been an absolute joy working with all of you.

Finally, I would like to give a heartfelt shout-out to my fellow Chinese colleagues at PME. **Yong**, **Jian**, **Minxing**, **Xianfeng**, **Ze**, **Jian**, **Hanqing**, **Zichao**, **Kai**, **Yang Yang**, **Xinxin**, **Binibin**, **Mingkai**, **Zhilin**, **Lidan**, **Xuerong**, **Hui**, **Ruibo** and **Yujiang**—thank you all for the companionship, the conversations, and the shared experiences. Having you around brought a sense of home that meant more than words can say.

也感谢代尔夫特中文学校。一个起初源于机缘巧合、却让我坚持志愿服务了五年多的地方。在这里，我并不是以“博士生”或“研究者”的身份存在，而只是一个参与其中、付出时间与精力、与人真实连接的普通人。这份角色的转换，对我而言意义非凡。感谢王红彦校长以及诸多老师在生活与工作中的支持与关照，让身处异国他乡的日子多了一份踏实与温度。正是这种人与人之间真诚而具体的连接，让“海外”不再只是地理概念，而逐渐成为可以安放情感与归属感的地方。中文学校也让我在博士研究之外，看见了另一种世界运行的方式：教育、家庭、文化传承、代际之间的努力与坚持。

在博士旅程即将画上句号之际，我怀着满腔的感恩，想把最深的谢意献给我的家人——你们是我生命中最坚实的依靠与最温暖的港湾。

首先，我要衷心感谢我的父母。是你们无私的支持与宽容，给予我走出国门、追寻学术梦想的勇气。从只身前往荷兰求学，到如今完成博士学业，这一路的坚持与收获，都离不开你们始终如一的理解、信任与默默守护。回望来路，从乡镇小学一步步走到今天，你们从未缺席我人生中任何一个重要的选择，用行动支持我读书、用信任让我安心前行。成为父亲之后，我才更加真切地体会到你们当年给予我的爱与包容，那是一种不求回报、始终站在身后的力量。你们对整个大家庭的付出与照顾，为我筑起了最稳固的后方，让我得以心无旁骛地投入学业。感谢总是唠唠叨叨、却用一生为我遮风挡雨的爸爸，感谢始终包容、坚定支持我选择的妈妈。你们的爱，是我最珍贵、也最笃定的底气。爸妈，辛苦了。

我也要特别感谢我的爷爷奶奶、姥姥姥爷。你们的爱，是我童年最温暖、也最深沉的底色。爷爷始终对知识与学业怀有敬畏与热忱，用一位知识分子的言行，为整个大家庭奠定了重视学习、尊重思考的精神基调。你们对我读书道路的支持与鼓励，在无形中塑造了我对学术与人生的态度。姥姥和姥爷以豁达、乐观的方式面对生活中的起伏与不易，让我学会以积极的心态看待世界，也给予我敢想、敢闯、敢拼的性格底气。你们的朴实、坚韧、善良与从容，始终是我为人处世的重要参照。直到今天，这些精神仍然陪伴着我，构成了我人生与人格中最稳定、最珍贵的底色。

感谢我的妻子，愿意陪我一起踏上异国他乡的求学之路。那是一条并不浪漫、甚至常常充满不确定性的路，而你却始终选择站在我身旁。在这段漫长的旅程中，你陪我经历了实验一次次失败后的沮丧，也陪我走过论文压力与自我怀疑交织的低谷；你见过我最疲惫、最焦虑、最不自信的样子，却从未动摇过对我的信任。比起任何一个阶段性的成果，我更珍惜的是我们携手走过的每一段日子。正是那些看似平凡却真实的经历，让奋斗不再冰冷，让理想有了温度，也让人生变得更加厚重而有意义。感谢你始终愿意相信我，哪怕前路并不清晰，依然选择与我一同向前。你在工作中承担起家庭的重要支撑，在生活里默默分担压力；你经历怀孕与生产的艰

辛，把身体与时间毫无保留地交付给这个家庭；我们一起在深夜哄睡孩子、在疲惫中学习如何成为父母，也在琐碎与焦虑中体会养育女儿的酸甜苦辣。直到最近，我们甚至已经开始为孩子未来的小学择校而操心——这些细碎而真实的片段，构成了我们共同走过的人生。十多年的相处，没有惊天动地的故事，更多的是日复一日的陪伴、理解与坚持。正是这种平淡，却让我深知其珍贵。谢谢你与我并肩走过成长、迷茫与变化，让我始终明白：无论身在何处、面对何种挑战，我都不是独自一人。

还有我亲爱的女儿安柏（Amber），你是我生命中最美好的礼物。当我书写论文最后章节的时候，恰好见证着你一天天的成长，这份并行的时光让我内心充满幸福与踏实。你的到来让我明白，人生不仅有学术与理想的追求，还有爱与陪伴所赋予的深意。你让我的世界变得更加辽阔，也更加柔软。正是在与你相伴的过程中，我更加深刻地体会到父母当年给予我的爱与付出。你也成为我面对生活与工作的源源动力，让我在前行的道路上多了一份温柔而坚定的力量。

博士求学之路虽已告一段落，但这段旅程中所积累的记忆、经验与情谊，将始终珍藏于心。感谢所有在这条道路上陪伴过我的人，是你们的支持、鼓励与善意，塑造了今日的我，也让我得以成为更好的自己。

Although my PhD journey is now complete, the memories, lessons, and friendships I gained along the way will forever remain in my heart. To everyone who has accompanied me on this path: your support, encouragement, and kindness have helped shape the best version of who I am today.

Zhichao Liu
January 2026

CURRICULUM VITÆ

Zhichao LIU

30-09-1992 Born in Shandong, China.

EDUCATION

2010–2014 Undergraduate in Polymer Materials and Engineering
Ocean University of China, China
Thesis: All-solid-state quantum dot-sensitized solar cell from plastic crystal electrolyte
Promotor: Prof. dr. Qunwei Tang

2016–2018 Master in Research Chemistry
Leiden University, The Netherlands
Thesis: Selectivity trends between oxygen evolution and chlorine evolution on iridium-based double perovskites in acidic media
Promotor: Prof. dr. Marc T.M. Koper

2019–2023 PhD in Micro and Nano Engineering
Delft University of Technology, The Netherlands
Thesis: Boron-doped diamond for electrochemical sensing: Material insights and application advances
Promotor: Prof. dr. Urs Staufer
Copromotor: Dr. Ivan Buijnsters

LIST OF PUBLICATIONS

PhD-Related Publications

1. **Zhichao Liu** , Simona Baluchová, Ziyu Li, Yaiza Gonzalez-Garcia, Clive E. Hall, Josephus G. Buijnsters, *Unravelling microstructure-electroactivity relationships in free-standing polycrystalline boron-doped diamond: A mapping study*, Acta Materialia, Volume 266, 119671 (2024).

2. **Zhichao Liu**, Simona Baluchová, Bob Brocken, Essraa Ahmed, Paulius Pobedinskas, Ken Haenen, Josephus G. Buijnsters, *Inkjet printing-manufactured boron-doped diamond chip electrodes for electrochemical sensing purposes*, ACS Applied Materials & Interfaces, 15, 39915-39925 (2023).

3. **Zhichao Liu**, Simona Baluchová, André F. Sartori, Ziyu Li, Yaiza Gonzalez-Garcia, Matthias Schreck, Josephus G. Buijnsters, *Heavily boron-doped diamond grown on scalable heteroepitaxial quasi-substrates: A promising single crystal material for electrochemical sensing applications*, Carbon, 201, 1229-1240 (2023).

4. **Zhichao Liu**, André F. Sartori, Josephus G. Buijnsters, *Role of sp^2 carbon in non-enzymatic electrochemical sensing of glucose using boron-doped diamond electrodes*, Electrochemistry Communications, 130, 107096 (2021).

5. Chenghao Zhang, **Zhichao Liu**, Chun Li, Jian Cao, Josephus G. Buijnsters, *Templated synthesis of diamond nanopillar arrays using porous anodic aluminium oxide (AAO) membranes*, Nanomaterials, 13(5), 888 (2023).

Other Works

6. Johannes G. Vos, **Zhichao Liu**, Florian D. Speck, Nickson Perini, Wentian Fu, Serhiy Cherevko, Marc T. M. Koper, *Selectivity trends between oxygen evolution and chlorine evolution on iridium-based double perovskites in acidic media*, ACS Catalysis, 9(9), 8561-8574 (2019).

7. Yu Zhang, *Organotin photoresists for extreme ultraviolet lithography*, PhD thesis, Van 't Hoff Institute for Molecular Sciences (HIMS), Faculty of Science, University of Amsterdam, Chapter 9: Low-valent tin carboxylates as photoresists (co-authored by **Zhichao Liu**), 2019. Persistent Identifier: hdl.handle.net/11245.1/2dfb06c7-1aa1-4135-9860-174a0e40a522.

8. Qinghua Li, Xiaoxu Chen, Qunwei Tang, Hongyuan Cai, Yuancheng Qin, Benlin He, Mingjun Li, Suyue Jin, **Zhichao Liu**, *Enhanced photovoltaic performances of quasi-solid-state dye-sensitized solar cells using a novel conducting gel electrolyte*, Journal of Power Sources, 248, 923-930 (2014).

9. Shuangshuang Yuan, Qunwei Tang, Benlin He, Haiyan Chen, Qinghua Li, Chunqing Ma, Suyue Jin, **Zhichao Liu**, H_3PO_4 *imbibed polyacrylamide-graft-chitosan frameworks for high-temperature proton exchange membranes*, Journal of Power Sources, 249, 277-284 (2014).

10. Qinghua Li, Qunwei Tang, Haiyan Chen, Haitao Xu, Yuancheng Qin, Benlin He, **Zhichao Liu**, Suyue Jin, Lei Chu, *Quasi-solid-state dye-sensitized solar cells from hydrophobic poly (hydroxyethyl methacrylate/glycerin)/polyaniline gel electrolyte*, Materials Chemistry and Physics, 144(3), 287-292 (2014).

TU Delft Delft University of Technology

ISBN 978-94-6384-913-5